

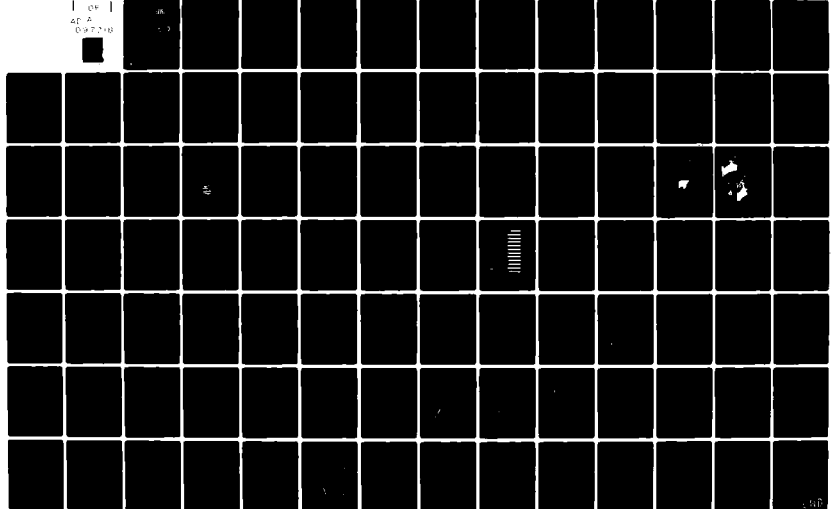
AD-A097 718 SYSTEMS AND APPLIED SCIENCES CORP RIVERDALE MD F/G 4/2  
DEVELOPMENT OF AUTOMATED OBJECTIVE METEOROLOGICAL TECHNIQUES (U)  
NOV 80 A M GERLACH F19628-79-C-0033

UNCLASSIFIED

AFGL-TR-81-0017

NL

1 09  
AFGL  
097748



AD A097718

AFGL-TR-81-0017

12

LEVEL II

DEVELOPMENT OF AUTOMATED OBJECTIVE  
METEOROLOGICAL TECHNIQUES

Alan M. Gerlach (ed.)

Systems and Applied Sciences Corporation  
6811 Kenilworth Avenue  
Riverdale, Maryland 20840

DTIC  
SELECTED  
APR 14 1981  
S E D

30 November 1980

Final Report for Period 1 December 1978 - 30 November 1980

Approved for public release; distribution unlimited

AMIC FILE COPY

AIR FORCE GEOPHYSICS LABORATORY  
AIR FORCE SYSTEMS COMMAND  
UNITED STATES AIR FORCE  
HANSCOM AFB, MASSACHUSETTS 01731

81 4 14 : 33

**Qualified requestors may obtain additional copies from the Defense Technical Information Center. All others should apply to the National Technical Information Service.**

| 19. REPORT DOCUMENTATION PAGE   |   | READ INSTRUCTIONS<br>BEFORE COMPLETING FORM   |
|---|---|---|
| 1. REPORT NUMBER<br><b>18</b><br>AFGL-TR-81-0017  | 2. GOVT ACCESSION NO.<br><b>AD-A097 718</b> | 3. RECIPIENT'S CATALOG NUMBER   |
| 4. TITLE (and Subtitle)<br><b>6</b><br>DEVELOPMENT OF AUTOMATED OBJECTIVE<br>METEOROLOGICAL TECHNIQUES  | 9   | 5. TYPE OF REPORT & PERIOD COVERED<br>Final Report<br>1 Dec 78 - 30 Nov 80                                |
| 7. AUTHOR(s)<br><b>10</b><br>Alan M. Gerlach (ed.)  | 15  | 6. PERFORMING ORG. REPORT NUMBER<br>F19628-79-C-0033  |
| 9. PERFORMING ORGANIZATION NAME AND ADDRESS<br>Systems and Applied Sciences Corporation<br>6811 Kenilworth Avenue<br>Riverdale, Maryland 20840  | 16  | 10. PROGRAM ELEMENT, PROJECT, TASK AREA & WORK UNIT NUMBERS<br>61102F, 62101F<br>667000AA<br><b>17 00</b> |
| 11. CONTROLLING OFFICE NAME AND ADDRESS<br>Air Force Geophysics Laboratory<br>Hanscom AFB, MA 01731<br>Manager/Charles Burger/LY  | 12) 91<br>11                                | 12. REPORT DATE<br>30 November 1980   |
| 14. MONITORING AGENCY NAME & ADDRESS (if different from Controlling Office)   |   | 13. NUMBER OF PAGES<br>94   |
|   |   | 15. SECURITY CLASS. (of this report)<br>UNCLASSIFIED  |
|   |   | 15a. DECLASSIFICATION/DOWNGRADING SCHEDULE  |
| 16. DISTRIBUTION STATEMENT (of this Report)<br><br>Approved for public release; distribution unlimited  |   |   |
| 17. DISTRIBUTION STATEMENT (of the abstract entered in Block 20, if different from Report)  |   |   |
| 18. SUPPLEMENTARY NOTES   |   |   |
| 19. KEY WORDS (Continue on reverse side if necessary and identify by block number)<br>PRIMITIVE EQUATION MODEL<br>SENSOR TESTS<br>OBJECTIVE SVR PREDICTION<br>AUTOMATED SATELLITE IMAGERY PROCESSING<br>BRIGHTNESS ANALYSIS<br>MESOSCALE FORECASTING<br>THUNDERSTORM TURBULENCE DETECTION<br>RADAR WIND RETRIEVAL<br>REAL-TIME STORM CELL TRACKING<br>AUTOMATED WIND OBSERVATIONS   |   |   |
| 20. ABSTRACT (Continue on reverse side if necessary and identify by block number)<br>This report summarizes weather research conducted by SASC in several areas: determining the effect on forecast accuracy of varying spatial resolution in a limited-area numerical weather prediction model; providing specialized programming support for sensor and technique testing; developing McIDAS-derived software for AWDS; developing objective techniques for estimating cloud base heights, predicting slant visual range, and predicting low-level winds; developing objective techniques for processing satellite imagery (cloud type identification, snow/cloud discriminator, brightness variation analysis); developing |   |   |

Block 20 (con't.)

applications software for McIDAS; maintaining, enhancing, and operating McIDAS; developing weather radar techniques (wind retrieval technique, storm cell detection and tracking, detection of turbulence in thunderstorms using radar methods).

|                    |                                     |
|--------------------|-------------------------------------|
| Accession For      |                                     |
| NTIS GRA&I         | <input checked="" type="checkbox"/> |
| DTIC TAB           | <input type="checkbox"/>            |
| Unannounced        | <input type="checkbox"/>            |
| Justification      |                                     |
| By _____           |                                     |
| Distribution/      |                                     |
| Availability Codes |                                     |
| Dist               | Avail and/or<br>Special             |
| A                  |                                     |

2 UNCLASSIFIED

## FOREWORD

This is the Final Report under Contract F19628-79-C-0033 with the Meteorology Division, Air Force Geophysics Laboratory. The contract extended from December 1, 1978 to November 30, 1980.

The report consists of narrative descriptions of work accomplished during those two years and two technical papers reporting research achievements. Work which was described or reported on previously (in Scientific Reports Nos. 1, 2, and 3) is referenced in the appropriate places but is not repeated except in brief summary form.

The contract called for effort in five discrete areas, reported upon in the monthly R&D Status Reports for the last two years under these headings:

- Numerical Weather Prediction
- Automated Weather System
- Satellite Meteorology
- McIDAS Operation and Enhancement
- Weather Radar Techniques.

This Final Report is organized similarly.

Personnel associated with these areas at any time during the contract are:

|                                  |   |                              |
|----------------------------------|---|------------------------------|
| Numerical Weather Prediction     | - | Donald C. Norquist, M.S.     |
|                                  |   | Peter J. Mansfield, Ph.D.    |
|                                  |   | Isidore M. Halberstam, Ph.D. |
|                                  |   | Gail M. Bertolini, A.B.      |
|                                  |   | Dorothy C. Moran, A.B.       |
|                                  |   | Scott D. Hamilton            |
| Automated Weather System         | - | Joan M. Ward, A.B.           |
|                                  |   | Russell C. Dengel, B.S.      |
|                                  |   | Maureen F. Hampton, B.A.     |
| Satellite Meteorology            | - | Gail A. Dengel, M.S.         |
|                                  |   | Robert P. d'Entremont, B.S.  |
|                                  |   | Michael E. Niedzielski, B.S. |
|                                  |   | Lucy K. Aharonian, A.M.      |
|                                  |   | Laurie E. Engels             |
| McIDAS Operation and Enhancement | - | John M. Powers, B.A.         |
|                                  |   | Barry A. Mareiro             |
|                                  |   | Judith E. Larkin             |

Weather Radar Techniques - Alan R. Bohne, Ph.D.  
John D. Tuttle, M.S.  
Wayne S. Collamore, B.S.  
Chen-Hung Chang, M.S.  
Glenn R. Smythe, M.S.

Principal Investigator was Alan M. Gerlach, Ph.D.

Subcontracts with Harris Corporation Computer Systems Division and Perkin-Elmer Customer Service Division provided on-site maintenance services for the McIDAS and Weather Radar Data Processing System respectively.

Reports were prepared by the scientists, engineers, and mathematicians identified in the Table of Contents with their technical reports.

## TABLE OF CONTENTS

|  |    |
|--|----|
| REPORT DOCUMENTATION PAGE  | 1  |
| FOREWORD   | 3  |
| TECHNICAL REPORTS  |    |
| A. THE EFFECT ON FORECAST ACCURACY OF VARYING SPATIAL<br>RESOLUTION IN A LIMITED-AREA NUMERICAL WEATHER PRE-<br>DICTION MODEL - Donald C. Norquist | 7  |
| I. Purpose of Study and Model Equations  | 7  |
| II. Implementation of Variable Resolution in<br>the Model  | 9  |
| III. Preparation of Initial and Boundary Values  | 11 |
| (A). Vertical Interpolation from Pressure<br>Levels to $\sigma$ Levels   | 12 |
| (B). Interpolation on $\sigma$ Surfaces  | 15 |
| (C). Wind Initialization   | 17 |
| (D). Boundary Values   | 19 |
| IV. Conclusion   | 20 |
| B. AUTOMATED WEATHER SYSTEM  | 21 |
| I. AFGL Weather Test Facility Support -<br>Joan M. Ward, Maureen F. Hampton  | 21 |
| (A). Doric   | 21 |
| (B). MAWS  | 23 |
| (C). Other   | 24 |
| II. Development of Observational Techniques -<br>Russell C. Dengel   | 24 |
| (A). AWDS Scenario Software  | 24 |
| (B). Cloud Base Height Estimation  | 25 |
| III. Development of Short-Range Prediction<br>Techniques   | 27 |
| (A). Objective Prediction of Slant Visual<br>Range - Russell C. Dengel   | 27 |
| (B). Objective Prediction of Wind -<br>Maureen F. Hampton  | 30 |

|   |    |
|---|----|
| C. SATELLITE METEOROLOGY: OBJECTIVE PROCESSING OF SATELLITE IMAGERY               | 33 |
| I. Identification of Cloud Types - Robert P. d'Entremont                          | 33 |
| II. Snow/Cloud Discriminator - Robert P. d'Entremont                              | 33 |
| III. Brightness Variation Analysis - Michael E. Niedzielski                       | 40 |
| IV. Navigation Fine-Tuning - Gail A. Dengel                                       | 42 |
| D. McIDAS OPERATION AND ENHANCEMENT   | 43 |
| I. Hardware Acquisitions - Barry A. Mareiro                                       | 43 |
| II. McIDAS Support to Research Projects - John M. Powers                          | 44 |
| III. System Operability - John M. Powers  | 46 |
| IV. Applications Software - Gail A. Dengel  | 46 |
| E. WEATHER RADAR TECHNIQUES   | 52 |
| I. Wind Retrieval - Glenn R. Smythe   | 52 |
| II. Real-Time Storm Cell Detection and Tracking - Chen-Hung Chang                 | 53 |
| III. Detection of Turbulence in Thunderstorms Using Radar Methods - Alan R. Bohne | 55 |
| (A). Introduction   | 55 |
| (B). Theoretical Investigations   | 57 |
| (C). Conclusions  | 94 |

## A. THE EFFECT ON FORECAST ACCURACY OF VARYING SPATIAL RESOLUTION IN A LIMITED-AREA NUMERICAL WEATHER PREDICTION MODEL

### I. Purpose of Study and Model Equations

One of the many challenges facing scientists engaged in numerical weather prediction modeling is that of minimizing prediction error while maximizing computational speed and efficiency. In finite difference models such as the six-layer Limited-Area, Fine-Mesh (LFM) model initially formulated by Shuman and Hovermale (1968)<sup>1</sup>, the large data lattice on which the atmospheric primitive equations are solved numerically requires a large computer storage capacity. In addition, multitudinous calculations are made at each time step of the model simulation so that relatively large processing times are involved. Although a finer grid resolution would yield better approximations to the derivatives in the primitive equations, it would also necessitate a proportionately greater outlay of computational storage and processing time. Furthermore, the necessary spatial interpolation of the initial data and boundary values onto the finer grid could significantly alter the input data and degrade the resulting forecast.

This Section describes an effort to investigate the effect of varying the spatial resolution on forecast accuracy by using a proven operational forecast model. The National Meteorological Center (NMC) six-layer LFM model as documented by Gerrity (1977)<sup>2</sup> was coded for the Air Force Geophysics Laboratory (AFGL) computer. The model was formulated for computations on a 33 x 33 point horizontal grid at each of six prognostic levels in the vertical, then was modified to perform the same computations on grids containing twice and four times the number of grid points at each level. Analyzed data at approximately the horizontal density of the 33 x 33 grid were interpolated to provide finer resolution initial and bound-

<sup>1</sup>Shuman, F.G., and J.B. Hovermale, 1968: An operational six-layer primitive equation model, J. Applied Meteor., 7, 525-547.

<sup>2</sup>Gerrity, J.F., Jr., 1977: The LFM Model - 1976: A documentation. National Meteorological Center, NOAA Technical Memorandum NWS, NMC 60.

ary values for the modified model. The goal of this study was to determine the optimal spatial resolution for a given input data density, in order to achieve maximum accuracy at minimum computational time and expense.

A full discussion of the method used in the model to solve the primitive equations was included in an earlier report by the author (Gerlach, ed., 1980)<sup>3</sup>. The primitive equations in Cartesian form for a conformal projection of the earth are repeated below; the symbols are explained in the earlier report:

$$\frac{\partial}{\partial t} \left( \frac{u}{m} \right) = \frac{v}{m} \left\{ f + m^2 \left[ \frac{\partial}{\partial x} \left( \frac{v}{m} \right) - \frac{\partial}{\partial y} \left( \frac{u}{m} \right) \right] \right\} - \frac{\partial \phi}{\partial x} - c_p \theta \frac{\partial \pi}{\partial x} - \dot{\sigma} \frac{\partial}{\partial \sigma} \left( \frac{u}{m} \right) - \frac{\partial}{\partial x} \left[ \frac{u^2 + v^2}{2} \right] - F_x \quad (1)$$

$$\frac{\partial}{\partial t} \left( \frac{v}{m} \right) = - \frac{u}{m} \left\{ f + m^2 \left[ \frac{\partial}{\partial x} \left( \frac{v}{m} \right) - \frac{\partial}{\partial y} \left( \frac{u}{m} \right) \right] \right\} - \frac{\partial \phi}{\partial y} - c_p \theta \frac{\partial \pi}{\partial y} - \dot{\sigma} \frac{\partial}{\partial \sigma} \left( \frac{v}{m} \right) - \frac{\partial}{\partial y} \left[ \frac{u^2 + v^2}{2} \right] - F_y \quad (2)$$

$$\frac{\partial}{\partial t} \left( \frac{\partial p}{\partial \sigma} \right) = -m^2 \left[ \frac{\partial}{\partial x} \left( \frac{u}{m} \frac{\partial p}{\partial \sigma} \right) + \frac{\partial}{\partial y} \left( \frac{v}{m} \frac{\partial p}{\partial \sigma} \right) \right] - \frac{\partial}{\partial \sigma} \left( \dot{\sigma} \frac{\partial p}{\partial \sigma} \right) \quad (3)$$

$$\frac{\partial \theta}{\partial t} = -m \left[ u \frac{\partial \theta}{\partial x} + v \frac{\partial \theta}{\partial y} \right] - \dot{\sigma} \frac{\partial \theta}{\partial \sigma} + H \quad (4)$$

$$\frac{\partial w}{\partial t} = -m^2 \left[ \frac{\partial}{\partial x} \int_{\sigma_U}^{\sigma_L} \frac{\alpha w u}{m} d\sigma + \frac{\partial}{\partial y} \int_{\sigma_U}^{\sigma_L} \frac{\alpha w v}{m} d\sigma \right] - \left[ \alpha w \dot{\sigma} \right]_{\sigma_U}^{\sigma_L} + C \quad (5)$$

$$\frac{\partial \phi}{\partial \pi} = -c_p \theta \quad (6)$$

$$\pi = \left( \frac{p}{p_0} \right)^{\frac{R}{c_p}} \quad (7)$$

$$\frac{\partial p}{\partial \sigma} \frac{\partial^2 \dot{\sigma}}{\partial \sigma^2} = -m^2 \left[ \frac{\partial}{\partial x} \left( \frac{1}{m} \frac{\partial p}{\partial \sigma} \frac{\partial u}{\partial \sigma} \right) + \frac{\partial}{\partial y} \left( \frac{1}{m} \frac{\partial p}{\partial \sigma} \frac{\partial v}{\partial \sigma} \right) \right]. \quad (8)$$

The coarsest resolution grid (33 x 33 points on each of six prognostic levels and one computational level) was set up to cover that seg-

<sup>3</sup>Gerlach, A.M., ed., 1980: Computer-based weather research. AFGL-TR-80-0069. Scientific Report No. 2, Contract F19628-79-C-0033, pp. 5 - 19.

ment of the NMC octagonal grid which completely includes the contiguous United States (see Figure A-1). The finer resolutions of the model involved grid points within this same region but at twice and four times the density at equally-spaced intervals. Finite differences were calculated using the method described by Shuman and Hovermale (1968). The input data were prepared so as to accommodate both second and fourth order spatial finite differences, but only the second order scheme was actually coded in the model. The model used a center-difference in time (leapfrog) method except at the first time step where forward difference was used.

## II. Implementation of Variable Resolution in the Model

The computer code for the  $33 \times 33 \times 7$  grid point model described in this report was formulated following a procedure identical to that described in the Gerrity documentation. The only exception is the absence of the time-smoothing technique used in the NMC model. This was not included because it was thought that this effect might mask the effect of changing the model resolution. After successful testing in this form, the model code was modified to permit the model computations to be carried out on  $65 \times 65 \times 7$  and  $129 \times 129 \times 7$  grid lattices. Since the originally formulated coarse resolution version of the model required essentially all of the core memory available on the AFGL CDC 6600 computer, a simple increase of storage array sizes to accommodate the higher resolutions was not possible. Instead, the code was redesigned to carry out the computations for the larger grids in  $35 \times 35 \times 7$  grid point sectors. Four such sectors were required for the medium resolution, and 16 were needed for the fine resolution. In this way, the core memory requirement remains constant with change of model resolution, and only the computation time increases accordingly.

In the code, Equations (1) - (5) are solved numerically in sequence for each sector, after which the sector's results are sent to mass storage before the computations for the next sector begin. The sectors are processed in a distinct sequential order, beginning with the southwesternmost, proceeding northward to the northwesternmost, then to the sector just east of the initial sector and northward again, and continuing with this process until the northeasternmost sector is completed.

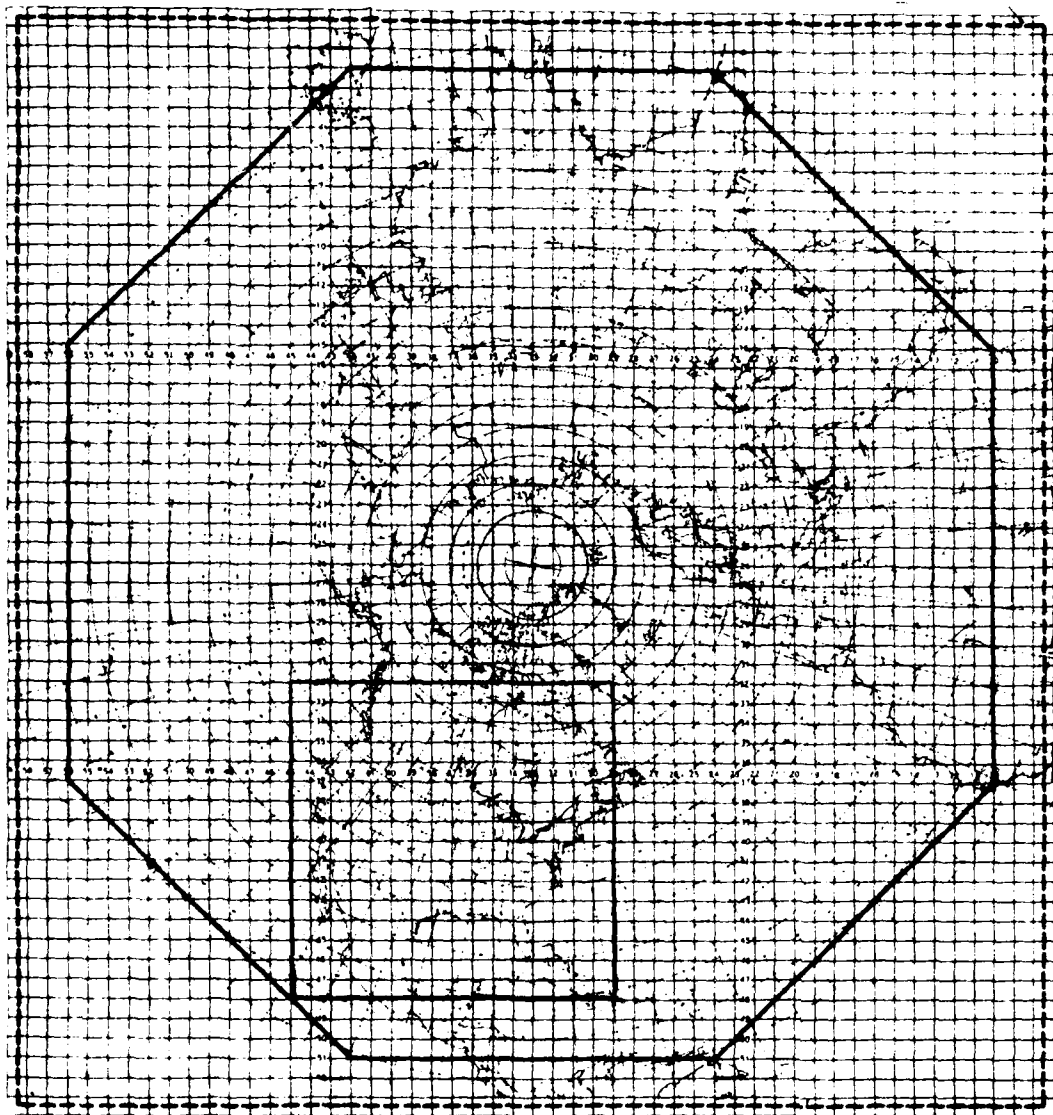


Figure A-1. The NMC octagonal grid. Square outlined region is the limited area considered in this study. Coarsest resolution considered is twice that of this grid. (Adapted from Shuman and Hovermale, 1968.)

After all newly predicted internal values for the sectors are stored in mass storage, external boundary values for that time step are included with the computed values and the entire sectors' values are stored. Then, sector by sector, the algorithms for precipitation processes are implemented in which all values of velocity, potential temperature, and precipitable water in the sectors are subject to possible adjustment. Finally, the check for super adiabatic lapse rate is carried out and the "dry adiabatic convection adjustment" is implemented for each column in which such instability is found. It was necessary to limit the number of attempts to remove instability completely from a particular column; the limit was placed at 300 tries, in this study. Upon completion of the super adiabatic check, the newly predicted and adjusted values of  $\frac{u}{m}$ ,  $\frac{v}{m}$ ,  $\theta$ ,  $\frac{\partial p}{\partial \theta}$ , and  $W$  are again sent to storage and the precipitation adjustment procedure is begun for the next sector.

In order to perform the finite-difference operations on the rows or columns which form the border between two adjoining sectors, three rows or columns common to both sectors are involved in the computations for both sectors. This overlap is necessary to provide a boundary row in order to compute internal values for each sector. What is used as a boundary row for computations in one sector is the last row for which computations were made in the adjoining sector. The extra storage space required for these rows was provided by having originally coded the model for a 35 x 35 grid which when doubled or quadrupled allows space for up to 70 x 70 or 140 x 140 respectively, enough to accommodate even a fourth order differencing scheme if it were to be incorporated into the model in the future.

### III. Preparation of Initial and Boundary Values

The model formulation followed exactly the methodology used in the NMC model. This was not true for the preparation of the input data for the model, however. The differences are due largely to the nature and spatial distribution of the atmospheric data chosen as input for the model. The data for initial values and boundary values are taken from the FGGE Level III-A data set<sup>4</sup>. The observed data had been objectively analyzed to produce these data values located at  $2.5^\circ \times 2.5^\circ$  latitude-

<sup>4</sup>Obtained from World Data Center-A, National Climatic Center, Asheville, NC 28801.

longitude intervals and at standard mandatory pressure levels. Values for zonal and meridional wind components, temperature, geopotential height up to 50 mb, and relative humidity up to 300 mb are available at each grid point. In addition, surface values of temperature and geopotential height are included in the data set, along with mean sea level pressure and tropopause temperature and pressure. Surface albedo, drag coefficient, terrain elevation, and sea surface temperature values are also provided and are used in the parameterizations included in the model. Since data values from the end time of the forecast are used to compute boundary values, both initial and final data values are processed through all steps leading up to preparation of the boundary values.

#### (A). Vertical Interpolation from Pressure Levels to $\sigma$ Levels

Once the desired data are extracted from the larger data set, the first step in preparing the data for model input is the vertical interpolation of data values from mandatory pressure levels to  $\sigma$  levels required by the model. The code which performs this interpolation processes each vertical column separately. The latitude and longitude of the column are used along with the velocity components to obtain the velocity components along grid lines.

At this point in the code the pressure at each of the  $\sigma$  levels is calculated in order to obtain  $\frac{\partial p}{\partial \sigma}$  for each of the three domains (troposphere, stratosphere, and computational layer) according to the definition of  $\sigma$  in each domain (see Gerlach, ed., 1980). Although mean sea level pressure is provided for each column, it is not used to obtain surface pressure where the terrain lies above sea level. Attempts to extrapolate a value for  $p_{sfc}$  in such cases using  $p_{msl}$  in the hydrostatic equation often yielded a surface potential temperature greater than that for the  $\sigma$  level immediately above it. As a result, surface pressure is determined using the hydrostatic assumption in the form

$$p_{sfc} = p_m \exp [(\phi_m - \phi_{sfc}) / RT] \quad (9)$$

where  $\bar{T}$  is the arithmetic average of the surface temperature and the temperature at the first mandatory pressure level ( $p_m$ ) above the surface. The surface pressure ( $p_1$ ) and the given tropopause pressure ( $p_5$ ) are then used to generate pressure values  $p_2$ ,  $p_3$ , and  $p_4$  for the intermediate  $\sigma$

levels as defined in the previous report (Gerlach, ed., 1980). The corresponding values of the Exner function at each of these levels is then obtained using Equation (7).

To calculate the value of geopotential at the tropopause ( $\Phi_5$ ) the geopotential is assumed to be a quadratic function of  $\pi$  in the stratosphere:

$$\Phi(\pi) = \Phi_5 - A(\pi - \pi_5) - \frac{B}{2}(\pi - \pi_5)^2. \quad (10)$$

Differentiating (10) with respect to  $\pi$ , it can be seen that  $A = c_p \theta_5$  and  $B = c_p [\theta_5 - \theta(\pi)]/(\pi_5 - \pi)$ . Eq. (10) is solved for  $\Phi_5$  using data from the next mandatory level above the tropopause, or in the case of  $p_5 < 100\text{mb}$ , data at 100 mb are used to obtain  $\Phi_5$ .

The value of geopotential at the top of the stratospheric domain ( $\Phi_7$ ) is obtained using the same assumption. Here the quadratic assumption takes the form

$$\Phi_7 = \bar{\Phi} - A(\pi_7 - \bar{\pi}) - \frac{B}{2}(\pi_7 - \bar{\pi})^2 \quad (11)$$

where  $\bar{\pi}$ ,  $\bar{\Phi}$  refer to the values of the respective variables at the mid-level (in  $\pi$ ) of a layer bounded by mandatory levels at or above the tropopause.

Using "U" and "L" to denote the known values at the top and bottom of this layer respectively, we have  $\bar{\pi} = \frac{1}{2}(\pi_L + \pi_U)$ ,  $A = -(\Phi_L - \Phi_U)/(\pi_L - \pi_U)$ , and  $B = c_p (\theta_L - \theta_U)/(\pi_L - \pi_U)$ . The expression for  $\bar{\Phi}$  can be derived as follows: substitute  $\bar{\Phi}$ ,  $\bar{\pi}$  for  $\Phi, \pi$  in Equation (10), and replace the "5" subscript in the result with "L". Then noting from the definition of  $\bar{\pi}$  that  $\bar{\pi} - \pi_L = \frac{1}{2}(\pi_U - \pi_L)$ , substitute this into the result. Form another equation by substituting  $\Phi_U, \pi_U$  for  $\Phi, \pi$  and  $\Phi_L, \pi_L$  for  $\Phi_5, \pi_5$  in Equation (10), and combine this result with the equation just obtained by eliminating the first order term between the two equations. The resulting expression for  $\bar{\Phi}$  is

$$\bar{\Phi} = \frac{1}{2}(\Phi_L + \Phi_U) + \frac{B}{8}(\pi_U - \pi_L)^2. \quad (12)$$

In the current study the "U" subscript denotes values of the subscripted variables at 100 mb and "L" denotes values at 150 mb when the tropopause pressure is greater than 150 mb. Values at 100 mb are used for the variables with "U" subscripts and tropopause values for "L" subscripted variables when  $p_5 < 150$  mb.

The symbol  $\Phi_{TOP}$  represents the geopotential at the top of the model atmosphere, a value which is chosen arbitrarily. Thus,  $\Phi_7 = \Phi_{TOP} - c_p \theta_c \pi_7$ , where  $\theta_c$  is the constant potential temperature in the computa-

tional layer. To derive an expression for  $\pi_7$  in terms of known quantities, this is rewritten in the form

$$\Phi_7 = \Phi_{TOP} - c_p \theta_c \bar{\pi} - c_p \theta_c (\pi_7 - \bar{\pi}) . \quad (13)$$

Subtracting (13) from (11) yields

$$(\pi_7 - \bar{\pi})^2 - [2(c_p \theta_c - A)/B](\pi_7 - \bar{\pi}) + 2C/B = 0 \quad (14)$$

where  $C \equiv \Phi_{TOP} - \bar{\Phi} - c_p \theta_c \bar{\pi}$ . Solving for  $\pi_7$  using the quadratic formula and choosing the negative sign gives

$$\pi_7 = \bar{\pi} + \frac{2C}{c_p \theta_c - A + \sqrt{(c_p \theta_c - A)^2 - 2BC}} . \quad (15)$$

The first step taken in solving (15) for  $\pi_7$  is to calculate an arbitrary value for  $\theta_c$  that would be satisfactory for the soundings of all grid points at the time of interest. The desired value of  $\theta_c$  is chosen using the sounding data from the southwesternmost grid point in order to obtain the largest value of  $\pi_7 \leq .4249630111$  (50 mb). The quantity  $\theta_c = (\Phi_{TOP} - \bar{\Phi})/c_p \bar{\pi}$  has its lowest values in the tropics, and the lower values will help insure real-valued solutions in (15) since B is always positive. Then by holding  $\theta_c$  constant at this value for all subsequent soundings,  $\pi_7$  will be prevented from becoming too small for other tropical soundings or too large ( $\pi_7$  is restricted to be less than .5180152937, or 100 mb) for high latitude soundings.

The following method is used to solve (15): starting with the southwesternmost sounding, choose a value for  $\Phi_{TOP}$  equal to  $4.41 \times 10^5 \text{ m}^2/\text{sec}^2$  (45 km), calculate  $\theta_c$  for that sounding, round the result up to the next higher value that is evenly divisible by ten and calculate  $\pi_7$ . If the discriminant or  $\pi_7$  become negative, increase  $\Phi_{TOP}$  by  $9,800 \text{ m}^2/\text{sec}^2$  (1 km) and recalculate  $\pi_7$ . If  $\pi_7 \leq .4249630111$  (50 mb), save this value of  $\theta_c$  for all soundings. If not, increase  $\theta_c$  by  $10^{\circ}\text{K}$  and recalculate  $\pi_7$ . For subsequent soundings, calculate  $\pi_7$  using the value of  $\theta_c$  obtained for the first sounding. If the discriminant or  $\pi_7$  become negative, increase  $\Phi_{TOP}$  by  $980 \text{ m}^2/\text{sec}^2$  (0.1 km) and try again. Once a real positive value of  $\pi_7$  is calculated, it is checked to see that  $\pi_7 < .5180152937$  (100 mb). If not, lower  $\Phi_{TOP}$  by  $980 \text{ m}^2/\text{sec}^2$  and try again. Eventually a satisfactory value of  $\pi_7$  will be obtained, and this value is used to obtain  $\Phi_7$ , using Equation (11), as well as to obtain  $\pi_6 = \frac{1}{2}(\pi_5 + \pi_7)$ .

Geopotential at all other diagnostic levels ( $k = 2, 3, 4$ , and 6) is calculated assuming a quadratic relationship in the natural logarithm of

pressure, as described by Gerrity (1977; see Equations A-2 through A-9). One modification was made to the scheme for calculating  $\phi_{k=2}$ : when  $p_{sfc}$  is less than the next mandatory pressure level lying below  $p_{k=2}$ , the surface data are used in place of the mandatory level data. This change combined with the use of temperature averaging in the equation for  $p_{sfc}$  eliminates the problem of  $\theta_{k=2} < \theta_{k=1}$  (calculated at a later step) in mountainous regions. It was observed that the calculation for  $\phi_{k=6}$  occasionally produced a value for  $\theta_6$  that was less than  $\theta_5$ . Therefore, a comparison of  $\theta_6$  with  $\theta_5$  was included in the code. If  $\theta_6 < \theta_5$ ,  $\phi_{TOP}$  and  $\phi_7$  are both increased by  $980 \text{ m}^2/\text{sec}^2$  (to increase  $\theta_6$  while keeping  $\theta_7$  constant) and another check is made. When this instability is resolved, the potential temperatures are calculated for the entire column using the hydrostatic equation, except  $\theta_1$  when the surface pressure is less than 850 mb. In this case,  $\theta_1$  is obtained using a linear interpolation of temperature in the natural logarithm of pressure between the surface and the mandatory level above it. The stability of the column is checked, and the dry adiabatic convection adjustment described by Gerrity is used in case any instabilities occur. Finally, the values of geopotential are recalculated from the stable values of potential temperature.

The final step in the vertical interpolation procedure is the generation of values for  $u, v$  at prognostic sigma levels using a linear interpolation in  $\pi$ . This is done by putting the mandatory pressure level values of  $u, v$  in order of decreasing  $\pi$ , finding the two mandatory levels which bound each  $\sigma$  level by comparing its  $\pi$  value with the mandatory level values, and performing a linear interpolation between the two to obtain  $u$  and  $v$  from their corresponding values at the mandatory levels. The  $u$  and  $v$  values at 70 mb and 50 mb are used to interpolate values for all  $\sigma$  levels with pressures less than 100 mb. Values for the specific humidity  $q$  at  $\sigma$  levels are obtained using a linear interpolation in pressure between mandatory levels.

#### (B). Interpolation on $\sigma$ Surfaces

The values of  $u, v, \phi, \frac{\partial p}{\partial \sigma}$ , and  $q$  for the appropriate  $\sigma$  locations at all grid points are passed on to a code which performs a series of interpolations at each  $\sigma$  location for each variable. In determining the best

method of interpolating values onto the finer resolution grids, bilinear, biquadratic, and trigonometric interpolation schemes were considered. An earlier investigation of three methods (trigonometric, bicubic spline, and four-point averaging) of interpolation to complete a staggered grid (Norquist, 1979)<sup>5</sup> showed the trigonometric method to be somewhat better than the other two in preserving the spectral components of the original data field. When the trigonometric interpolation was compared with the bilinear and biquadratic methods in interpolating onto points representing the next finer resolution grid, no similar significant advantage was observed. Therefore, since the bilinear and biquadratic interpolation algorithms had already been coded for the finer resolution interpolations, they were used in the current study.

First, a four-point bilinear interpolation is performed in which the data values at each  $2.5^{\circ} \times 2.5^{\circ}$  latitude grid point are used to obtain values on a  $35 \times 35$  grid corresponding to the grid network of the model. This set of points includes both the  $33 \times 33$  grid of the coarsest resolution plus an extra row of grid points surrounding it which are used for subsequent interpolations and initialization. After this interpolation, two successive biquadratic interpolations are carried out to obtain the values at grid points representing twice and four times the resolution of the  $35 \times 35$  grid. A 16-point least-squares biquadratic interpolation is used in which a slight modification is required when a grid point of higher resolution falls on a grid line of lower resolution. The value of such a point is obtained by averaging the two least-squares estimates on the two sides of the line. After all interpolations are completed, domain values of  $\frac{\partial p}{\partial \sigma}$  and the values of  $\phi$  at diagnostic levels are used to evaluate potential temperature  $\theta$  at the six prognostic levels, using Equation (6). The values generated for the computational layer are averaged and this average value is assigned to all grid points in this layer. Also, precipitable water  $W$  is calculated from  $q$  and  $\frac{\partial p}{\partial \sigma}$  and reduced-image velocity components are formed by dividing the velocity component values by the appropriate grid point value of the map factor  $m$ .

<sup>5</sup> Norquist, D.C., 1979: An investigation of three methods of completing a staggered data field on a square grid. AFGL-TR-79-0197. Scientific Report No. 1, Contract No. F19628-79-C-0033.

(C). Wind Initialization

The input data processing continues with the initialization of the wind field at each prognostic level and for each resolution. This is done by assuming that the given reduced-image wind field on the grid can be represented by a vector function  $\vec{v} = (\frac{u}{m})\vec{i} + (\frac{v}{m})\vec{j}$  where  $\vec{i}$  and  $\vec{j}$  are unit vectors parallel to grid lines and positive eastward and northward respectively. It is further assumed that  $\vec{v}$  can be considered the sum of a non-divergent component  $\vec{v}_\psi$  and an irrotational component  $\vec{v}_\chi$  defined by

$$\vec{v}_\psi = \vec{k} \times \vec{\nabla} \psi \quad \vec{v}_\chi = \vec{\nabla} \chi \quad (16)$$

where  $\vec{k}$  is the unit vector in the vertical pointing upward,  $\vec{\nabla} = \vec{i} \frac{\partial}{\partial x} + \vec{j} \frac{\partial}{\partial y}$  the horizontal del operator,  $\psi$  is the scalar stream function, and  $\chi$  the scalar velocity potential function. Then it can be shown that the vorticity  $\zeta$  is

$$\zeta \equiv \vec{k} \cdot \vec{\nabla} \times \vec{v} = \nabla^2 \psi \quad (17)$$

where  $\nabla^2 = \vec{i} \frac{\partial^2}{\partial x^2} + \vec{j} \frac{\partial^2}{\partial y^2}$  is the horizontal Laplacian operator, while the

divergence  $D$  is given by

$$D \equiv \vec{\nabla} \cdot \vec{v} = \nabla^2 \chi \quad (18)$$

In order to formulate a wind field less likely to contain observation, analysis, or interpolation errors that might excite spurious motions in the forecast, a non-divergent and an irrotational wind value were calculated at each of the interior grid points for each resolution for both the initial and final data sets.

The non-divergent component values were obtained by first calculating the vorticity  $\zeta = \frac{\partial v}{\partial y} - \frac{\partial u}{\partial x}$  numerically for each grid square center using the Shuman-Hovermale (1968) finite difference scheme. The next step is to solve (17) numerically to obtain values of  $\psi$  at the interior grid square centers. Values of  $\psi$  for the centers of the exterior row of grid squares are needed to do this, and these values are estimated as follows.

First, assume that on the exterior grid square centers the component of the wind normal to the grid as a whole is due only to the non-divergent

wind. If  $\vec{V}$  is expressed in natural coordinates as

$$\vec{v} = -\left(\frac{\partial \psi}{\partial n} + \frac{\partial \chi}{\partial s}\right)\vec{s} + \left(\frac{\partial \psi}{\partial s} + \frac{\partial \chi}{\partial n}\right)\vec{n} \quad (19)$$

where  $\vec{s}$  and  $\vec{n}$  are unit vectors tangential and normal to the boundary of the grid as a whole, then this assumption means that  $\frac{\partial \chi}{\partial n} \equiv 0$  and  $\vec{v} \cdot \vec{n} = \frac{\partial \psi}{\partial s}$ . Letting the subscript "i" indicate the counter for the exterior grid squares, we have in finite difference form

$$\psi_{i+1} = \psi_i + \frac{\Delta \psi}{\Delta s}(\Delta s) = \psi_i + (\vec{v} \cdot \vec{n})(\Delta s). \quad (20)$$

The normal component of the given wind at the sides of the exterior grid squares is then obtained by averaging the normal component values located at the grid points on both the interior and exterior edges of each exterior grid square side. Since the divergence theorem dictates that the sum of the normal components of the wind over the boundary of the region equals the total divergence in the region, this sum must vanish for non-divergent flow. This sum is obtained using each of the normal component values on the exterior grid square sides as calculated above, then it is divided by the number of such normal components to find the value each normal component is to be adjusted by (all adjusted equally) to make their sum vanish. Then Equation (20) is used with these adjusted values to obtain estimates of  $\psi$  in the exterior grid square centers, beginning with  $\psi_{i=1} = 0$  in the lower left corner of the grid. These boundary values of  $\psi$  are used with the interior values of  $\zeta$  to solve the Poisson equation (17) numerically. The resulting values of  $\psi$  in the interior grid square centers are then used with the boundary values of  $\psi$  estimated above to obtain  $(\frac{u}{m})\psi = -\frac{\partial \psi}{\partial y}$  and  $(\frac{v}{m})\psi = \frac{\partial \psi}{\partial x}$  at the interior grid points using finite differences.

The calculation of the irrotational component of the wind at interior grid points is done in an analogous way. The divergence  $D = \frac{\partial}{\partial x}(\frac{u}{m}) + \frac{\partial}{\partial y}(\frac{v}{m})$  is calculated for each grid square center. In obtaining values of  $\chi$  for the exterior grid square centers, we note that the motion is irrotational in the interior only if the circulation around the region, given by  $\oint \vec{v} \cdot \vec{s} ds$ , vanishes. Since  $\oint \frac{\partial \chi}{\partial s} ds \equiv 0$ , this condition is met if the line integral of the tangential component of the non-divergent wind vanishes.

In the procedure used in this study, this component is removed everywhere on the boundary in the following way. The tangential component of the non-divergent wind on the grid points just inside the exterior grid points calculated above is averaged with the tangential component of the given wind on each exterior grid point (in which it is assumed that the given wind is largely non-divergent) to obtain an estimate of  $\vec{v}_X \cdot \vec{s}$  at the side of each exterior grid square. This is subtracted from the full wind value at this same location obtained as in the non-divergent wind discussion, to obtain  $\vec{v}_X \cdot \vec{s}$  at each point. Then

$$\chi_{i+1} = \chi_i + \frac{\Delta x}{\Delta s} (\Delta s) = \chi_i + (\vec{v}_X \cdot \vec{s}) (\Delta s) \quad (21)$$

is used to obtain values of  $\chi$  at each exterior grid square centers beginning with  $\chi_{i=1} = 0$ . The Poisson equation (18) is then solved for the interior values of  $\chi$  from which  $(\frac{u}{m})_\psi = \frac{\partial \chi}{\partial x}$  and  $(\frac{v}{m})_\psi = \frac{\partial \chi}{\partial y}$  are obtained at the interior grid points. The initialized wind at all interior grid points is then given by

$$\vec{v}_{in} = \left[ (\frac{u}{m})_\psi + (\frac{u}{m})_\chi \right] \vec{i} + \left[ (\frac{v}{m})_\psi + (\frac{v}{m})_\chi \right] \vec{j} \quad (22)$$

#### (D). Boundary Values

Data from both the initial and final time of the forecast are processed through the preceding steps. Then boundary values for each prognostic variable at each location on the exterior of the grid lattice are calculated using a linear interpolation in time. These boundary values are calculated for each time step of the forecast. Time steps of six, three, and 1.5 minutes are used for the single, double, and quadruple resolution cases. In addition, the time step increment (rate of change of quantity at a grid point multiplied by appropriate time step length in seconds) is calculated for grid points located one and two rows in from the boundary for each prognostic variable in order to provide sponge-type boundary conditions. The sponge boundary scheme involves the combination of one-third computed value and two-thirds increment value at grid points located one row from the boundary, and two-thirds computed value and one-third tendency value at two rows in from the boundary.

#### IV. Conclusion

This report describes a variable resolution limited-area numerical weather prediction model developed to test the effect on forecast accuracy of changing spatial resolution. Unfortunately, the contract period elapsed before the model could be successfully run using atmospheric data. Therefore no conclusions can be drawn concerning the relationship between model resolution and forecast accuracy. It is recommended that the model formulated in this effort be utilized to examine the nature of this relationship in finite-difference models.

## B. AUTOMATED WEATHER SYSTEM

Under the contract SASC was responsible for developing and implementing computerized data processing methods and techniques to evaluate new or improved weather sensors and observational techniques and short-term prediction methods for weather parameters critical in aviation.

### I. AFGL Weather Test Facility Support

SASC activity in this area was largely based on data produced by two acquisition systems installed at the AFGL Weather Test Facility (WTF) at Otis AFB, Cape Cod. These systems are the 200-Channel Doric Data Logger and the Modular Automated Weather System (MAWS). For them, SASC developed four large CDC 6600 computer programs: REQUOTE, PWP, MAWS, and VERIFY. In addition, many associated programs were written to obtain specific statistical analyses and discrete data displays.

#### (A). DORIC

The Doric Data Logger writes onto magnetic tape voltages recorded by over 100 weather sensors located on towers and a ground site, constructed in a runway simulation configuration.<sup>1</sup> Instruments included are wind sensors of several types, temperature and dew point instruments, precipitation gauges, radiometers, and a variety of visibility meters. The Doric system gathers readings five times per minute, 10 times in the case of wind sensors, and records the information onto tapes which are shipped daily to AFGL at Hanscom AFB. In the contract period nearly 500 tapes were received and processed.

The raw voltage tapes are processed by a computer program called REQUOTE. This program converts voltages to one-minute mean meteorological unit data which in turn are used for display or further analysis.

Data received from REQUOTE were fed to the Present Weather Program (PWP) in order to produce automatic "present weather" observations (wea-

<sup>1</sup>The AFGL Weather Test Facility is further described in Gerlach, ed. (1980), pp. 21-23.

ther conditions and obstructions to vision) comparable to those reported by a human weather observer. By using a decision-tree approach the PWP was successful in discriminating weather conditions such as moderate or heavy drizzle, rain, snow, freezing drizzle or freezing rain. Obstructions to vision included blowing dust or sand, blowing snow, smoke, haze, fog, ground fog, or ice fog.

Hourly results of automated observations were compared by computer plot with FAA human observations for data collected over the period March 1978 - April 1979. These plots were used by AFGL in a study on automation of visual weather observations. The results showed about 84 percent agreement. Lack of agreement for the remaining hours was attributed, in part, to lack of responsiveness of the rain gauge to small amounts of precipitation and in part to the spatial separation of the observer and the test facility.

The FAA obstruction to vision reports for the same period, when plotted in comparison with the results obtained from the PWP, showed similar results. The difference between the two methods was shown by the AFGL study to fall mostly in the five to eight mile visibility range. FAA regulations require an obstruction to vision report only if visibility is less than seven miles. In the ranges close to this limit variations could occur. In general, however, analysis of the results of the PWP using the data collected appeared to verify the approach taken.

In addition to the Present Weather Program model, data were fed from REQUOTE to many statistical routines to determine correlations, scatter, and goodness-of-fit. Data from REQUOTE were also used to evaluate new or improved weather sensors. Wind sets such as the Rosemount, J-Tec, and Gill were compared with the Climatronics.<sup>2</sup> Several models of small-volume forward-scatter meters (Fumosens) were evaluated by varying calibration equations and plotting the conversions, in extinction coefficients, in comparison with transmissometer data.

Another important use of the data base was in the slant visual range prediction model discussed below (pp. 27, 30). To determine probability estimates for below-limits SVR conditions, SASC wrote routines to incorporate Markov and Equivalent Markov techniques into REQUOTE. Also, a plot program was written to display the predicted probability of below-

<sup>2</sup>See Gerlach, ed. (1980), pp. 20-29, for a detailed description of the wind set tests.

limit visibility using the Markov and Equivalent Markov techniques.

A Doric wind shear routine, DORWIND, was developed by SASC to evaluate the spatial homogeneity of wind measurements collected at towers A, Q, and X at WTF. Sensors located at various tower levels report values used to compare wind shears and statistics such as mean, standard deviation, standard error, root mean square error, bias, correlation, and line of best fit. DORWIND is run on a regular basis with each Doric tape.

(B). MAWS (Modular Automated Weather System)

A second data acquisition system, MAWS, was installed at the WTF in late Summer, 1979. Using the same instruments as the Doric, with the addition of three rotating beam ceilometers for determining cloud base height, the MAWS records one-minute means in meteorological unit: onto magnetic tape. It also has the capability of interspersing raw voltages with the weather data means to provide test information. In addition, three remote sites on Cape Cod, instrumented to give additional information particularly on sea fog, are tied into the MAWS retrieval system. The sensor information contained in the data records is relayed over telephone long lines to Hanscom AFB and packed onto tapes at AFGL. Because of packing one-minute mean data, rather than 12-second voltage data as in Doric, MAWS tapes hold 15 to 20 days of data per tape.

Computer program MAWSE was developed by SASC to accomplish the unpacking, processing, and display of data acquired from the sensors at Otis. An editing routine was devised to recover data records sometimes marked by faulty identifications and other errors transient in the system, and was implemented in MAWSE.

Using MAWS data, program VERIFY was developed by SASC to perform a thorough verification analysis of short-range probability and categorical forecasts. Probability forecasts are substantiated using rank probability scores, Brier scores, a "T" statistic, a measure for skill, and a Friedman's Analysis of Variance test. Categorical forecasts are verified using a Chi-Square statistic, percent correct, threat score, and bias. VERIFY also updates a master file containing raw statistics from all episodes of low ceiling.

Two routines, WINDCOM and VSBYCOM, were written by SASC to compare

statistically wind and visibility observations reported by MAWS (at Scott AFB) and a human observer at Scott during the period Jan. 1977 - Jan. 1979. MAWS values were averaged over a ten-minute period and compared with a human observation taken once during the same ten-minute interval. WINDCOM and VSRY OM compute means, standard deviations, variances, bias, correlation, root mean square error, percent root mean square error, standard error, covariance, and line of best fit. Statistics were updated as successive tapes were processed.

(C). Other

Other software written by SASC included a data retrieval program to process tapes from the Monitor Labs Data Acquisition System used for testing laboratory instruments. This program provides interpretation of any number of data channels up to 200, and any number of scans of the channels capable of fitting on a single tape. Also devised was a data reduction program for the Particle Measuring System Inc. spectrometer, which measures fog droplet size.

## II. Development of Observational Techniques

(A). AWDS Scenario Software

To meet requirements for accurate and timely reporting of airfield weather conditions, the Air Weather Service (AWS) plans to modernize its Base level weather support in the 1980's. The Automated Weather Distribution System (AWDS) will encompass the modernization of Air Force weather station functions. AWDS will serve as a data products handler, producing computer-generated alphanumeric and videographic displays of meteorological information. Critical weather parameters which affect airfield operations include visibility, wind speed and direction, turbulence, and precipitation. AWDS will provide the technology with which these parameters will be collected, analyzed, and displayed.

SASC meteorologists developed software applicable to the AWDS scenario through adaptation and exploitation of software developed for the Man-computer Interactive Data Access System (McIDAS). Development concentrated on routines to display standard and derived meteorological parameters. These new routines access current McIDAS library modules to pro-

duce both plotted and analyzed weather data.

Specific operational software includes a program which plots upper air wind observations on constant height levels. This program, WINHGT, displays either wind vectors, wind flags, or numerical values of wind speed and direction. A total of 16 levels, from 1,000 to 50,000 feet, may be plotted on base maps ranging from full USA to individual states. Derived atmospheric stability parameters and estimates of precipitable water are also available. This program, STABLE, provides the option of displaying either plotted or analyzed information. Quantities available for display include K-index, totals index, lifted index, convective temperature, and precipitable water. Information may be displayed on Mercator projections or overlaid on satellite imagery. Output can be directed to either a CRT or line printer.

#### (B). Cloud Base Height Estimation

Data storage and manipulation routines were developed to perform the initial evaluation of a series of algorithms used to translate rotating beam ceilometer (RBC) measurements into estimates of cloud base height (from 0 to 6,000 ft) and total sky condition (clear, scattered, broken, or overcast). A total of 15 different algorithms was tested.

Preliminary results suggested modifications to the cloud base height/sky condition program CLOUD. Originally, CLOUD produced output which included sky condition estimates for up to five different layers **between** the surface and 8,700 ft. RBC measurement error (inherent in the instrument) necessitated lowering the height of the maximum cloud layer from 8,700 to 6,000 ft. With this drop in maximum cloud height the maximum number of cloud layers was also reduced (from five to three) to produce a more realistic depiction of the sky condition.

In all a total of 14 episodes (62 individual data sets) was processed during the period from June through September, 1980.

Figure B-1 is a flow chart of the storage and manipulation software. Each step represents a program used either to reduce or store processed information. The individual programs are as follows:

TRANS - Input to this program comes directly from CLOUD. The information is coded and packed to speed processing and reduce stor-

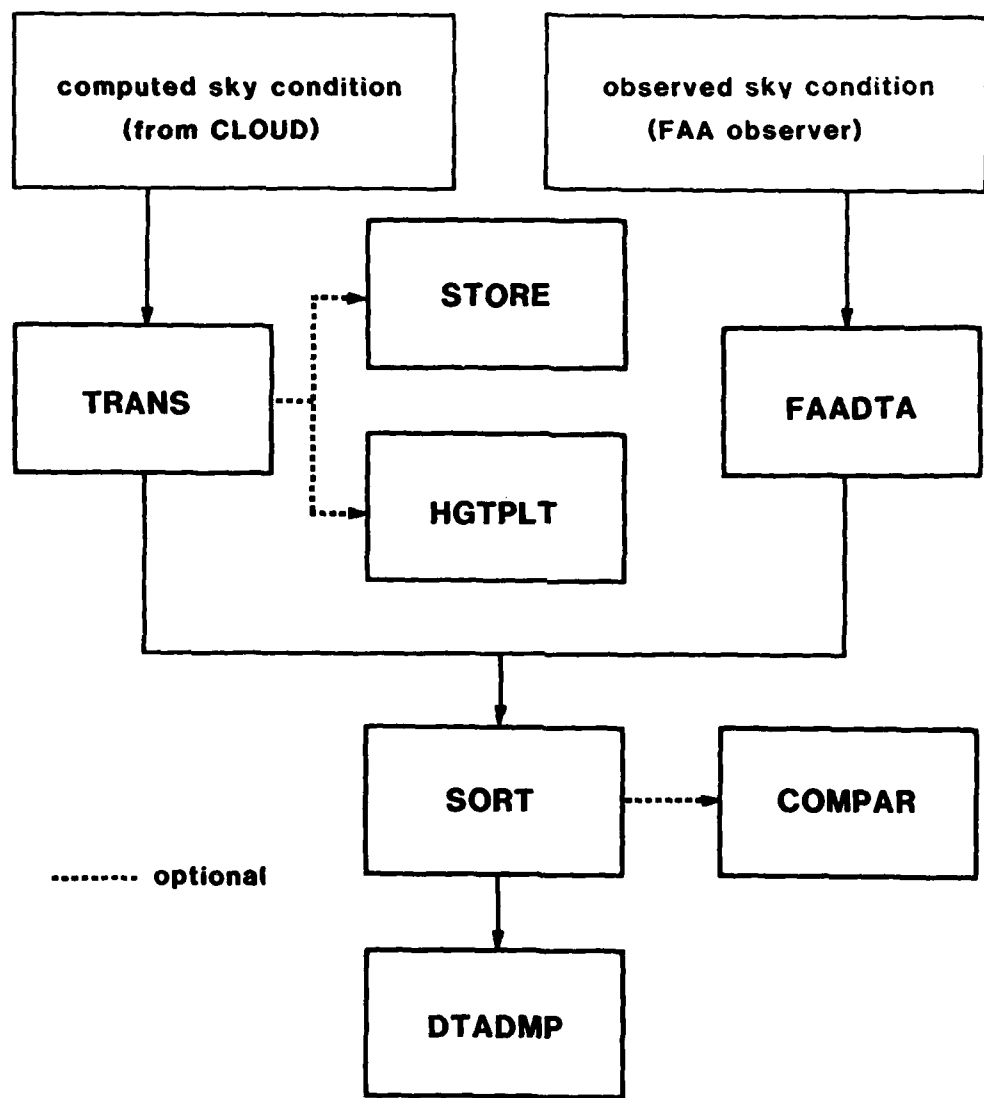


Figure B-1. Data storage and manipulation software.

age. Output is stored in separate episodes containing as many as ten different methods (calculations) for evaluation.

STORE - Used to store the packed data from TRANS on magnetic tape. Information is filed in separate episodes.

HGTPLT - Produces time vs. height ink plots of any one method (1 - 15) for a particular episode. Plots represent altitude of individual cloud decks, the condition of each layer, whether the layer is continuous with time, the height of measured ceiling, and the presence of a layer above the measured ceiling. Figure B-2 is a sample of HGTPLT output.

FAADTA - Produces CDC 6600 data files from sky condition reports taken by FAA observers. The information is coded and key punched in a form compatible with the information received from the automatic routine and provides ground truth for the evaluation.

SORT - Produces a single data file by combining both the observed data set and calculated estimates.

COMPAR - Produces computer ink plots of observed/calculated ceiling heights on time vs. height axes for any one method during a particular episode. Figure B-3 is a sample of COMPAR output.

DTADMP - Calculates statistical information used to evaluate the cloud height and sky conditions algorithms. For every method tested, DTADMP tabulates observed vs. calculated number of layers, total sky cover, and ceiling reports, and calculates the following statistics:

Percent Correct  
Percent Agreement  
Probability of Detection (POD)  
Threat Score (TS)  
False Alarm Ratio (FAR).

Method statistics are presented for all past, present, and total (past + present) episodes.

### III. Development of Short-Range Prediction Techniques

#### (A). Objective Prediction of Slant Visual Range

SASC meteorologists aided AFGI scientists in developing an objective

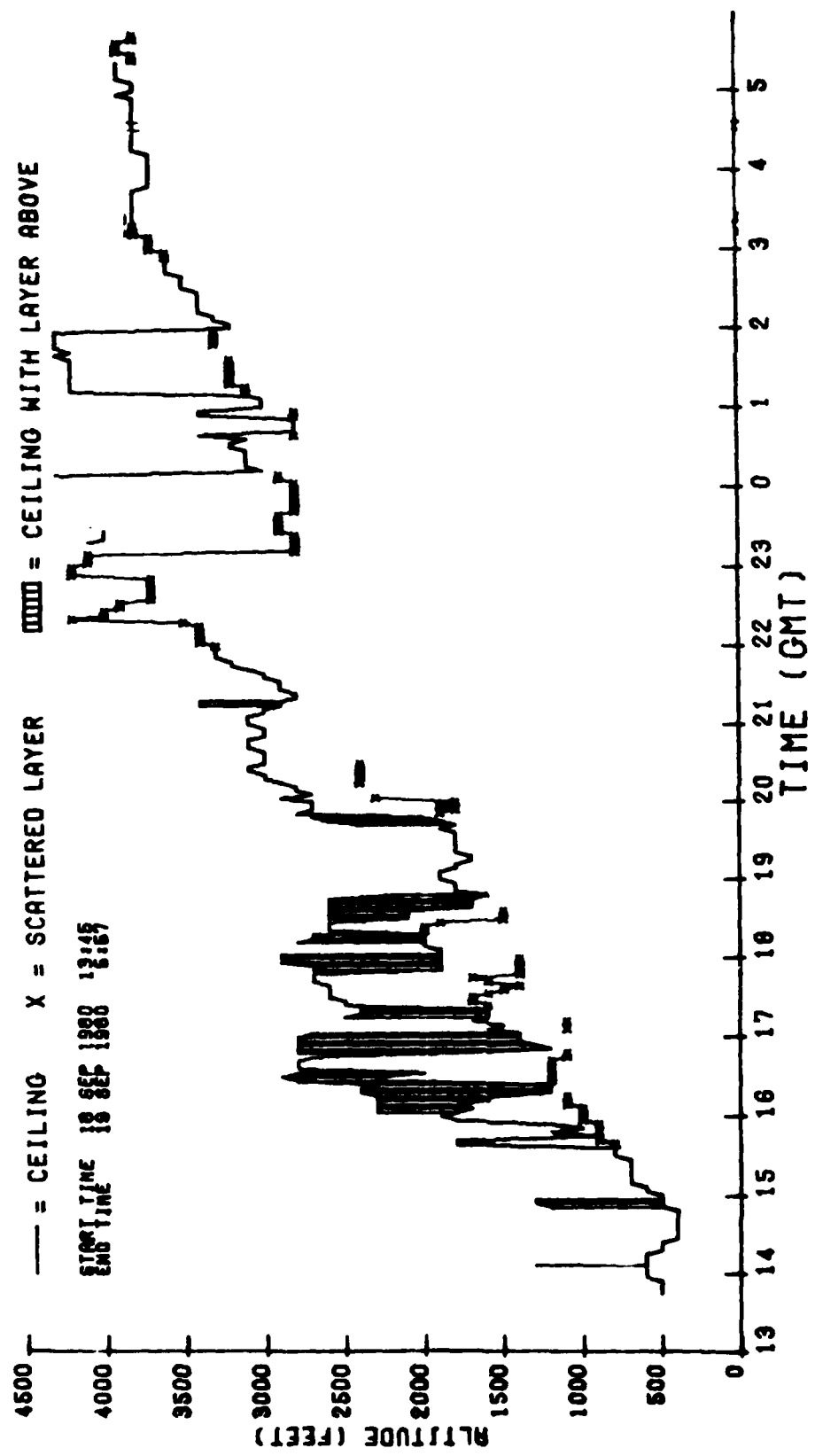


Figure B-2. HGTPLT sample output.

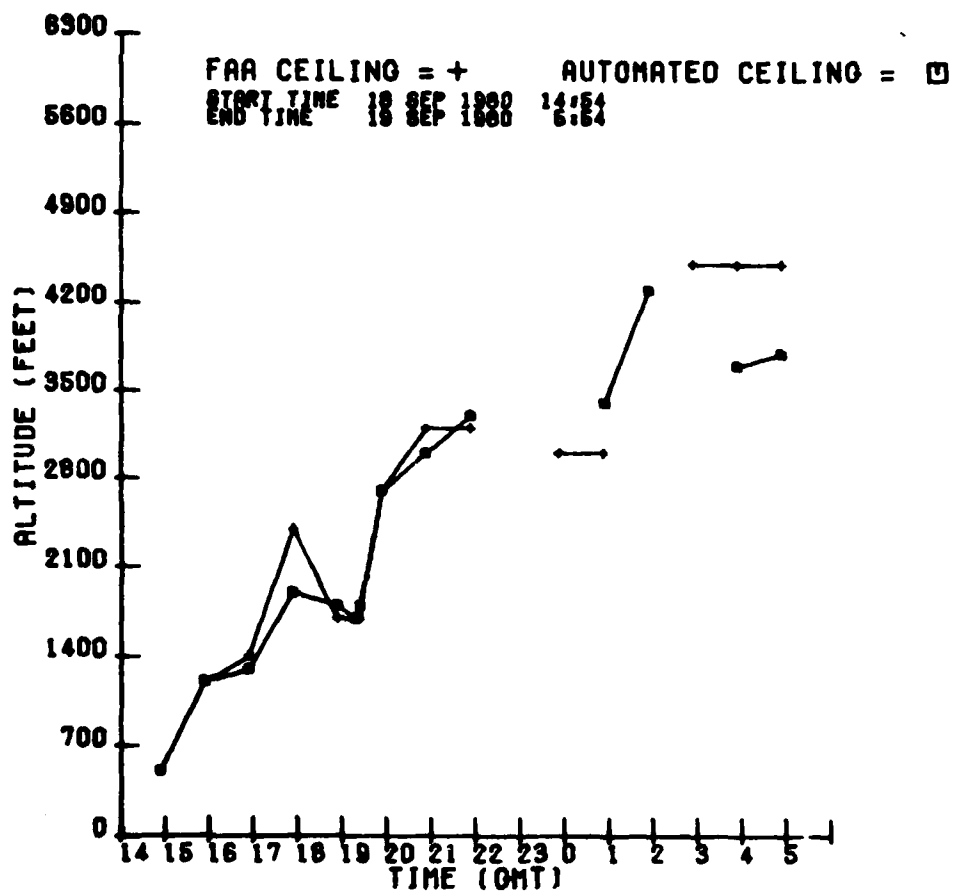


Figure B-3. COMPAR sample output.

technique for specifying visibility conditions below FAA Category I and II aircraft landing guidelines from forward scatter meter (FSM) measurements. Atmospheric extinction coefficients measured by an array of FSM's on three instrumented towers at AFGL's Weather Test Facility were used to specify the Slant Visual Range (SVR) in the landing approach zone.

The accuracy and reliability of three prediction techniques used to estimate SVR at forecast intervals of 2, 5, 10, 30, and 60 minutes were tested and evaluated. Techniques consisted of an adaptation of a Markov chain known as the "Ornstein-Uhlenbeck" process, Regression Estimation of Event Probabilities (REEP), and an Equivalent Markov method based on the classical Markov transition matrix. Prediction equations were formulated using twenty cases of reduced visibility (6,300 minutes of data). An independent data set of twenty-five episodes (9,900 minutes of data) was used to compare the techniques.

Results of this study indicated that in cases of reduced visibility caused by advection fog, a prediction scheme which utilizes SVR measurements yields far more accurate forecasts of below-limit conditions than the standard Runway Visual Range (RVR) measurements being used. Probability of detecting reduced visibility conditions for both Category I and II landing operations is 91 percent or greater.

Of the three prediction techniques evaluated, the Equivalent Markov scheme demonstrated a higher degree of reliability and accuracy than did the Markov or REEP techniques.

A paper entitled "Objective Prediction of Slant Visual Range During Advection Fog Situations," which documents the results of this study (co-authored by SASC and AFGL meteorologists), was presented at the American Meteorological Society's Eighth Conference on Weather Forecasting and Analysis, Denver, June 10 - 13, 1980. The paper appears in the preprints of the conference.<sup>3</sup>

#### (B). Objective Prediction of Wind

Study of mesoscale wind variability, leading to the development of automated wind analysis and prediction methods, required establishment of

<sup>3</sup>Geisler, E.B., and R. C. Dengel, 1980: Objective prediction of slant visual range during advective fog situations. Preprint, Eighth Conference on Weather Forecasting and Analysis, AMS, Boston; pp. 420-423.

a suitable data base. Data tapes generated by the AFGL Mesonet were selected for this purpose. The Mesonet collected meteorological data (wind, temperature, dew point, visibility, and rainfall) from September 1972 through May 1976 at 26 specially designed weather stations in northeastern Massachusetts.

A three-phase project was established to edit the data, generate a climatology, and perform statistical analyses aimed at developing an objective wind prediction technique.

Programs designed by SASC to edit, condense, and group these data into a more complete data set are MESOFV, HOURAVE, HSTOGRM, and EDIT.

MESOFV converts voltage values, taken at ten-second intervals from each of the 26 Mesonet stations, into one-minute meteorological means. These one-minute values of wind direction and speed, temperature, dew point, and extinction coefficient (exco) are written onto a permanent file. This file eliminates further processing of the Mesonet magnetic tape, thus decreasing computer processing time.

One-minute means are then computed into hourly and daily averages using the program HOURAVE. Hard copies of these averages, along with maximums, minimums, and standard deviations, are printed for each Mesonet file generated by MESOFV.

HSTOGRM was designed as a supplement to HOURAVE, to make easier the identification of spurious data. This program generates a histogram of each variable at each station for the period covered by one Mesonet tape. In addition, a list of variables and times in which an erroneous value seems to occur is printed at the end of each program.

MESOFV is run only once with HOURAVE and HSTOGRM for initial data processing purposes. All other editing is done using one-minute means from the permanent file generated by MESOFV, hereafter referred to as netfile.

Hard copies produced by HOURAVE and HSTOGRM are analyzed and spurious data identified. A set of data cards is punched containing times and stations at which a variable has been flagged as bad. These cards are used as input for EDIT, which searches netfile for flagged variables and replaces them with a value of 999. Whenever this value is encountered by later programs, it is ignored. EDIT also insures that there are no time gaps on the file, by filling in missing minutes and giving the corresponding variables a value of 999. When editing is complete, netfile is re-

placed by an edited version of the one-minute means. HOURAVE and HSTO-GRM then produce updated versions of their respective outputs to be re-analyzed for further editing.

This editing process is repeated (usually three or four times) until a fully edited netfile exists. The edited netfile is later packed by program MAGFILE onto a new magnetic tape (Mesoxx). Ten netfiles are placed on one Mesoxx tape. Eventually these one-minute mean packed tapes will replace the Mesonet tapes.

Each of these programs was designed to make intensive data reduction as selective as possible. Because of the amount of processing time and data involved, job turnaround time was often slow. To contract completion, 40 Mesonet tapes were fully edited and four new magnetic tapes created (Meso01 - Meso04). With this newly created data base, preparations for analysis of mesoscale wind variability were begun.

SASC prepared a series of programs to generate a climatological atlas of monthly, seasonal, and annual weather at various times of the day. One of these programs is MAINFRE, which categorizes wind direction and speed, temperature, dew point, and exco values, and stores them on permanent random access files. These files are used to generate tables containing relative frequency distributions, maximum and minimum values, and means of given periods of time. SASC also wrote programs to print these tables on hard copy.

The tables contained in the atlas are:

- Wind direction vs. wind speed
- Wind direction vs. exco
- Wind direction vs. temperature
- Wind speed vs. temperature
- Wind speed vs. exco
- Maximum temperatures
- Minimum temperatures
- Mean temperatures
- Maximum wind speed and direction
- Exco

Each frequency distribution is dependent on station, month, and time factors. This climatological summary is run and updated with each Mesoxx tape. When the atlas is completed, results will be interpreted for effects of topography, diurnal change, and synoptic scale weather patterns.

## C. SATELLITE METEOROLOGY: OBJECTIVE PROCESSING OF SATELLITE IMAGERY

### I. Identification of Cloud Types

SASC scientists investigated an objective satellite imagery classification technique which identifies the cloud type of a visible or infrared image sample  $25 \times 25$  n mi in size. Defense Meteorological Satellite Program (DMSP) 2/3 n mi visible and infrared data from an area in the vicinity of the Mediterranean Sea were used for this study. These data on tape were supplied to AFGL by the Air Force Global Weather Central (AFGWC). The classifier, a modification of an earlier technique applied to visible data only, extracts information about the texture and patterns of clouds in an imagery sample by examining the coefficients of its discrete Fourier transform. It is capable of classifying a  $37 \times 37$ -pixel ( $25 \times .25$  n mi) image in less than one second on AFGL's CDC 6600 computer. The classifier was tested on a total of 143 image samples, and was allowed to choose the cloud type of an image sample from one of nine types: stratocumulus, stratus, cumulus, clear, altocumulus, altostratus/nimbostratus, cirrus, cirrostratus, and cumulonimbus. On average, 7 to 8 image samples were correctly identified out of every 10 it was allowed to classify. A scientific report, "Performance of the Discrete Fourier Transform Satellite Imagery Classification Technique," submitted for publication in June 1980,<sup>1</sup> offers a complete description of this study.

### II. Snow/Cloud Discriminator

In June 1979 the DMSP launched an experimental snow/cloud discriminator sensor (SSC) in a polar orbit. The sensor is a linear array of detectors sensitive to reflected sunlight in the 1.51 - 1.63 micron spectral region. Visible (0.4 - 1.1 micron), infrared (10 - 12 micron), and snow/cloud data for December 1979 were sent on tape to AFGL by AFGWC. Coverage was limited to near local noontime orbits over eastern North and Central America, and extreme northern South America. Because of power supply prob-

<sup>1</sup>d'Entremont, R.P., 1980: Performance of the discrete Fourier transform satellite imagery classification. AFGL-TR-80-0175. Scientific Report No. 3, Contract F19628-79-C-0033.

tems, no data were available after December 1979.

Snow/cloud imagery contains useful information with which cloud/no cloud and snow/no snow decisions can be more confidently made, inasmuch as the snow/cloud spectral region exhibits several unique physical characteristics. In this region of the near IR, water droplets are good reflectors of sunlight, ice particles are not so good, and oceans, lakes, and other bodies of water, along with snow-covered ground, are poor reflectors. When land is not covered by snow or ice, it appears brighter in the snow/cloud bandwidth than it does in the visible. Coastlines and shores thus contrast well with surrounding waters, which appear black.

In the visible and in the 10 - 12 micron IR, snow, low stratiform, and low cumuliform clouds tend to appear brighter than clear land or ocean. Thus fog and low stratus can be confused with snow-covered ground. However, snow-covered land is dark in the snow/cloud, while low stratiform and cumuliform clouds composed of water droplets are bright. The sharp distinction between snow (dark) and liquid clouds (bright) earns the SSC the name "snow/cloud discriminator."

Snow/cloud data also can help satellite imagery analysts more confidently determine whether clouds are composed of ice particles or water droplets. Clouds that are bright in the visible and warm in the IR appear bright in the snow/cloud (water droplets), while clouds that are bright in the visible but cold in the IR appear gray in the snow/cloud (ice particles).

Figure C-1 shows the geographical locations of the images in Figures C-2 and C-3. These figures contain SSC imagery which illustrates some of the features discussed in the preceding paragraphs. Figure C-2 contains visible, IR, and snow/cloud imagery over a region of northwestern South America. In the lower part of each image a large group of cumulonimbus clouds can be seen. These clouds, between 250 and 300 n mi wide, appear bright in the visible and cold in the IR. Snow/cloud imagery in the corresponding bright/cold areas of the visible/IR pictures is gray, indicating that the cloud tops consist of ice particles. Surrounding lower-level water clouds (extreme lower right) are much brighter.

Figure C-3 is imagery over Cape Cod, the coast of Maine, and Nova Scotia. The bright clouds (warm in the IR) in the lower right of each visible image are stratocumulus. The fact that these clouds appear bright in the snow/cloud indicates that they consist of water droplets. Note

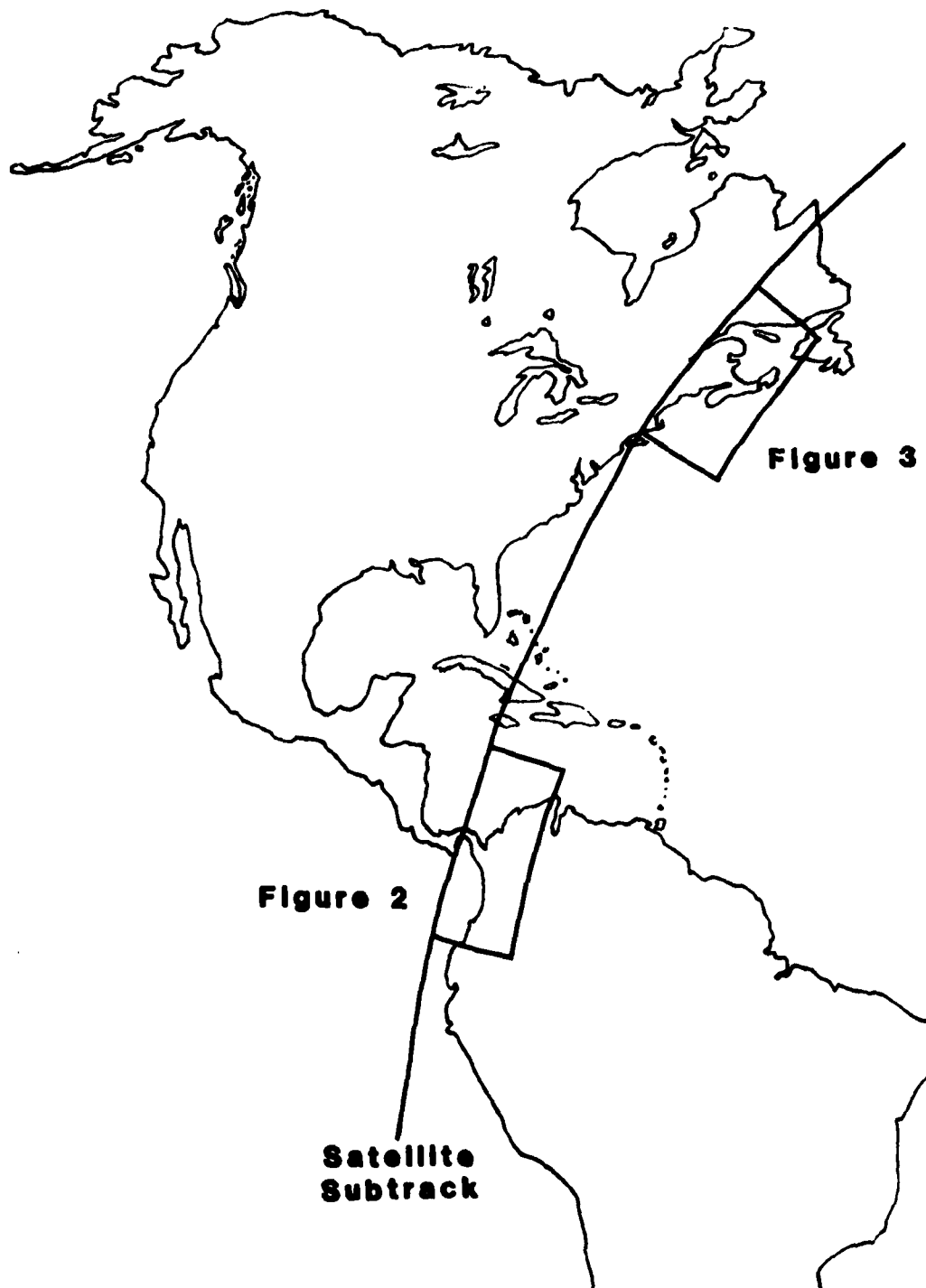


**Figure C-1.** Geographical locations of satellite imagery in Figures C-2 and C-3.



3 n mi Visible



3 n mi Infrared



6 n mi Visible



6 n mi Snow/Cloud



6 n mi Infrared

Figure 1. Visible and infrared imagery of snow/ice fields over eastern Central America.



**3 n mi Visible**



**3 n mi Infrared**



**6 n mi Visible**



**6 n mi Snow/Cloud**



**6 n mi Infrared**

Figure 1-3. Visible, IR, and SSIC images over New England and Nova Scotia.

that the Maine and Nova Scotia coastlines stand out against the ocean in the snow/cloud better than they do in the visible. Unfortunately, snow cover in eastern North America was very sparse in December 1979 when these data were collected. Thus there were not many good snow-covered ground imagery samples to use as illustrations.

Each image in Figures C-2 and C-3 is labeled with its sensor and resolution at satellite subpoint. The cross-track resolution of a visible or infrared pixel is 1.66 n mi at satellite subpoint, and decreases to 2.95 n mi at scan edge. Along-track resolution is close to 3.0 n mi. The visible and IR images to either side of the 6 n mi snow/cloud image were generated by averaging the 3 n mi visible and IR data in order to make them look like (match up with) the snow/cloud imagery. (This was done by AFGWC, but a similar set of averaged visible and IR images was also generated by SASC at AFGL.) The cross-track resolution of the coarser snow/cloud data is 4.1 n mi at satellite subpoint, decreasing to 8.3 n mi at scan edge. Along-track resolution of SSC decreases from 6.6 n mi at subpoint to 9.1 n mi at scan edge.

When visible and IR images of 3 n mi resolution are averaged (smoothed) to correspond pixel for pixel to snow/cloud imagery, small-scale variabilities in cloud brightness and temperature are lost. As a consequence, a significant amount of small-scale cloud feature information is lost. Knowing the "footprint" sizes (resolutions of each pixel edge) and geographical locations of each 3 n mi visible and IR pixel and each 6 n mi snow/cloud pixel enables the higher resolution visible/IR data to be mapped into the coarser snow/cloud imagery. Thus the several visible and IR 3 n mi pixels that lie within the same area as a 6 n mi snow/cloud pixel can be found. More information about the type of feature an SSC pixel represents can be obtained by observing the smaller-scale brightness variations of those 3 n mi pixels. Such analyses can help an automated classifier determine the cloud or surface type of an image sample.

Figure C-4 contains graphical displays of the relationships among averaged visible, averaged IR, and snow/cloud grayshades. These graphs were constructed by randomly choosing an interesting cloud feature on an image, subjectively classifying it, and then using a McIDAS command to extract the visible, IR, and SSC grayshade values of that feature. Re-

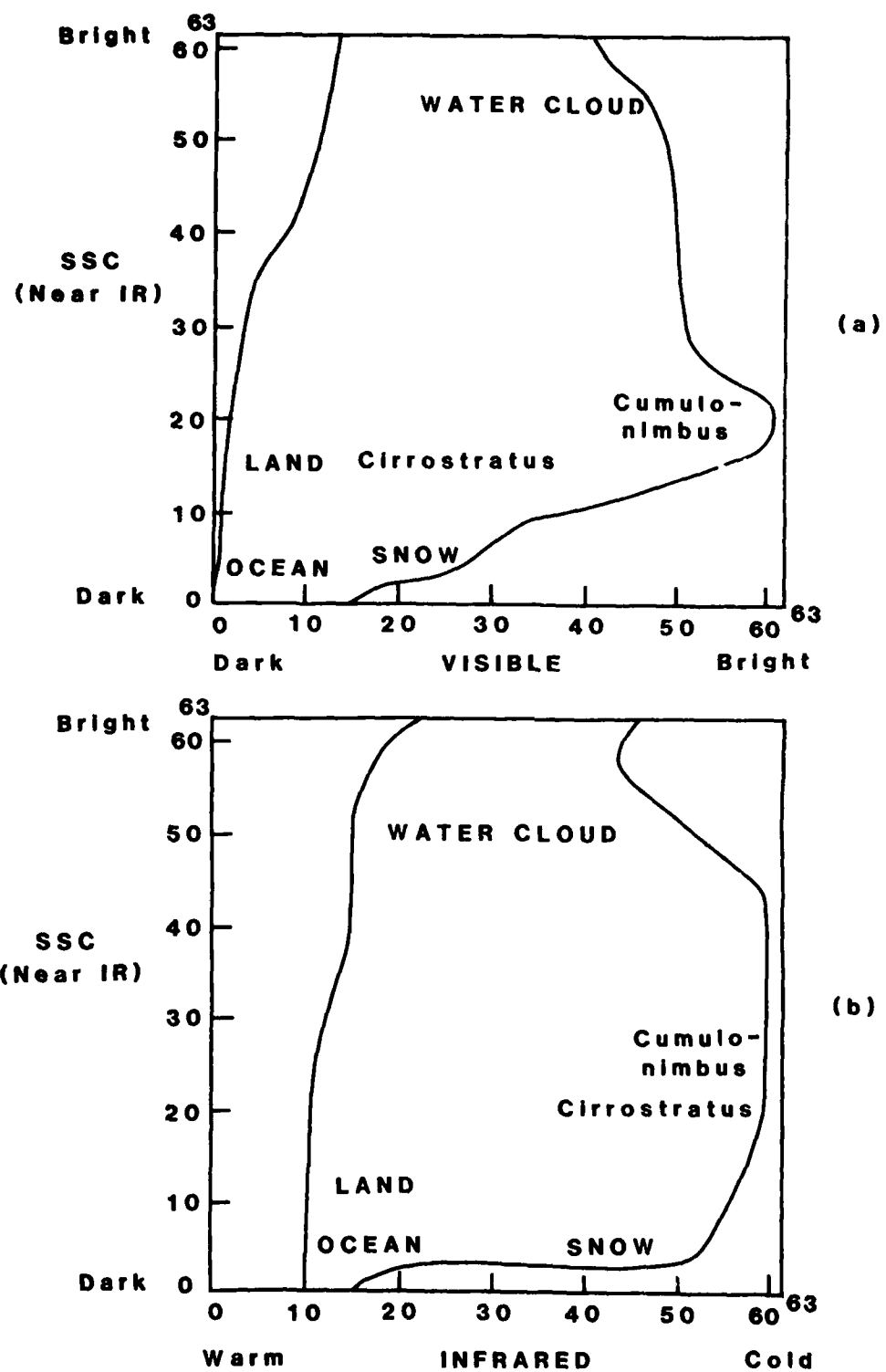


Figure C-4. Graphical displays of cloud- and ground-type thresholds.

sults were manually tabulated. These graphs point out grayshade thresholds among different meteorological situations.

In Figures C-4a and C-4b it is seen that the range between land and ocean backgrounds in the snow/cloud is greater than it is in either the visible or the IR. Note how well water clouds are separated from snow-covered ground in the SSC, and also how well water clouds are separated from ice clouds. The thresholds illustrated in these graphs could be used as input to a cloud type- and phase-determining algorithm.

Beyond the curves bounding the cloud types in the graphs of Figure C-4, no grayshades were found in the images that were examined. It is interesting to note in Figures C-4a and C-4b that the SSC is often saturated, primarily by thick, dense water droplet clouds. In the visible and IR, sensor saturation would most likely be caused by thick cirrostratus or well developed cumulonimbus.

In summary, certain characteristics of snow/cloud imagery logically determine how best to use it in an automated mode. Sharp snow/bare ground and ice cloud/water cloud contrasts dictate that an automated snow/cloud imagery processing algorithm should distinguish snow on the ground from bare ground or low clouds and identify cloud phase. Other potential applications of these data include determination of cloud type, fractional cloud cover, cloud top height, thickness, and temperature, and estimations of mesoscale visibility.

### III. Brightness Variation Analysis

In an effort to utilize geostationary satellite data for determining cloud cover amounts, SASC scientists developed and implemented software to analyze ODIS (Offline Data Ingest System) data.<sup>2</sup> ODIS data consist of one-mile resolution hourly images centered on the northeastern US as received from the GOES and SMS series of geostationary satellites. Data from the period March 1977 - April 1979 were processed. Seven sites - Syracuse, Buffalo, Wilkes-Barre, Philadelphia, Atlantic City, Lynchburg, and Wallops Island - were selected as study stations to provide a geographical mixture of the sampling region. Hourly weather observations

<sup>2</sup>See Gerlach, ed. (1980) for detailed description of the data reduction method and software; pp. 74 - 81.

from these stations were used as the ground truth in the study.

The first step in the analysis was a data reduction to provide more easily studied parameters. To this end program CENTER was developed. CENTER identifies and corrects garbled or missing scan lines of data and bad row count numbers. Provisions were also made to ignore occasional half-hourly data which have no corresponding ground truth data. Then using basic and fine-tuned navigation information provided by the McIDAS, CENTER isolates a 27 x 27 picture element array centered on a particular station. This array is further divided into nine 9 x 9 arrays and the brightness count for each picture element is converted to a reflectivity value normalized for solar zenith angle. The average reflectivity, maximum and minimum values, and the standard deviation and range of values for each 9 x 9 array and the entire 27 x 27 array are then calculated and saved. These data must then be checked to insure that the navigation parameters are applied to the proper image. Bad ODIS data headers, multiple headers, and incorrect recorder start-up times occurred and the necessary modifications were made to correct the input data for those tapes.

The collected data were then stratified into eleven categories of opaque cloud cover: clear, 10 percent opaque cloud cover, 20 percent, 30 percent, etc., using the ground truth data as the basis for stratification. Program ALBZGT performed a first order statistical analysis of these data. Erroneous samples were checked for poor navigation and corrected or rejected depending on individual circumstances. The eleven categories were further subdivided into two classes, water clouds and ice clouds, and then re-analyzed by ALBZGT. The results generated could be used to determine the characteristics which define each cloud cover class.

In a related effort program THRESH was developed by SASC to aid in constructing a cloud cover truth table. Using the same 27 x 27 array of reflectivity values isolated by CENTER, program THRESH calculates the number of picture elements in the array that are above a given threshold value. Also calculated is the percent of the total array that number represents. Several threshold values can be input to determine which one provides the best ground/cloud discriminator value. Once this best threshold value is determined, the percent of the 27 x 27 array containing clouds can be correlated to a percent cloud cover as determined by the ground truth data producing the cloud cover truth table.

Software was also developed by SASC scientists to analyze the infrared data which correspond to the visual data that were already processed. Program ANALYZE performs the same functions as CENTER except for use of thermal counts, not reflectivity values. However, since the IR data have a resolution of two miles in the east-west direction and four miles in the north-south direction, the additional steps of dividing each IR picture element into eight one-mile picture elements and then aligning these expanded data with the previously analyzed visual data must be performed. Unfortunately, the visual-IR alignment changes with each satellite, creating a problem which remains to be solved.

#### IV. Navigation Fine-Tuning

The earth location of points on satellite images is characteristically in error by several kilometers because of inherent inaccuracies in the navigation procedure employed by McIDAS. While errors of this magnitude are tolerable for many qualitative purposes, research applications frequently require greater precision. A fine-tuning method was developed by SASC to determine correction factors which are applied to navigated data to achieve the accuracy required.

Visible channel imagery recorded by the ODIS is read into McIDAS and displayed on a TV screen. The positions of one to four landmarks (earth features whose locations are known to an accuracy greater than or equal to the resolution of the satellite sensor) are measured. The differences between the locations of the landmarks as predicted by the original navigation and their actual measured positions are used to determine two offsets, one for scan line number and one for element number (roughly corresponding to north/south and east/west offsets). These values are used to compute correction factors for the navigation. This technique, when applied to each image time, is capable of reducing earth location errors to one kilometer or less.

## D. McIDAS OPERATION AND ENHANCEMENT

### I. Hardware Acquisitions

McIDAS hard copy capability was improved by acquisition of a Model 146 Memory Interface manufactured by Leonessa Engineering Company of Bedford, MA. This memory interface stores a satellite image 500 lines by 672 elements or a total of 316,000 pixel elements. The interface accepts data at a high transmission rate from the computer, stores them in memory, then re-transmits the data at a slower rate required by the Laserfax Model 850 to produce the final copy. The resulting 8½" x 7½" print is of markedly higher quality than that produced by the previously used hard copy system.<sup>1</sup> The Leonessa system also features a grayscale adjustment panel which permits various enhancements to be set into an image.

During 1980 a Model 147 Radar Interface, also from Leonessa Engineering Company, was purchased to add to the existing McIDAS components. A memory telephone with 19 pre-selectable numbers, each corresponding to a particular radar site, was incorporated with the Model 147 into the McIDAS Facsimile Interface. The resulting system allows the user to call up and display in real-time, radar data for sites located in the US. The 19 pre-selected radar sites may be changed according to the user's requirements.

An engineering study was initiated to determine what components are needed to enable McIDAS to receive GOES satellite data from the experimental VISSR Atmospheric Sounder (VAS) satellite launched in September 1980. The new satellite operates on what is called an AA mode of transmission while the existing McIDAS equipment can only handle the A mode. A plan was developed to purchase a VAS frame synchronizer and associated circuitry for use with the current data acquisition components in order to receive the new mode of transmission. Since the operational VAS satellite will ultimately replace the present satellite as the primary data down-link, appropriate system modification is mandatory.

<sup>1</sup> See Gerlach, ed. (1980), pp. 30 - 32, for description of earlier acquisitions.

Another modification was the recent installation of two 24-hour timers in the Sony Archive System. The timers are attached via a relay matrix to the A.C. power inputs of the two Sony 2800 Video Recorders. The recorders can be scheduled to operate at selected time periods by the insertion or withdrawal of timer pins. The timers also have day-select pins enabling them to be set up for operation several days in advance. This is especially useful at night or on weekends when an operator is not available yet satellite data acquisition is necessary.

The Sony Archive System playback capabilities were enhanced by the addition of a Search Track Monitor. The monitor shows the position of the tape during playback by displaying the time of day, scan count, Julian date, and year. This information is recorded on a separate track of the video tape during the real-time recording of the satellite transmission. When played back, the track information is sent to the monitor where it is decoded and displayed through the LED panel. The monitor is particularly helpful during data extraction when the user is looking for a specific portion of a tape which can contain up to five hours of recorded video.

Documentation of McIDAS hardware was begun in 1980. Since its installation in 1974 the system has undergone numerous modifications, including wiring and equipment changes which are not reflected in the existing documentation. The intent is to consolidate in book form documentation of all the electronics in the system, thus reducing the search time spent by a technician in isolating a malfunction. Documentation nearing completion at contract end included the data acquisition system, layout of the interconnecting cables of the video subsystem, and construction of schematics outlining various control words in the digital interface drawer.

## II. McIDAS Support to Research Projects

In 1980 McIDAS supported three AFGL research projects using aircraft: the Large Scale Cloud System (LSCS) study conducted by the Cloud Physics Branch; the Icing program conducted by the Climatology and Dynamics Branch; and the Tactical Weapons Support System program conducted by the Optical Physics Division.<sup>2</sup>

<sup>2</sup>See Gerlach, ed. (1980), pp. 33 - 41, for details of earlier support.

The LSCS program, a continuing AFGL effort, sampled large homogeneous cloud masses as they progressed from west to east across the US. The aircraft, a specially instrumented C-130, collected hydrometeor data such as particle size, number, concentration, type, spatial distribution, and liquid water content at various altitudes. McIDAS satellite imagery loops (both visible and infrared) which depict cloud growth and decay as well as cloud top temperatures, enabled the ground support team to ascertain the most desirable locations for aircraft cloud sampling. This information was relayed to the in-flight team, allowing effective utilization of available aircraft time. McIDAS provided conventional surface observation plots of wind vectors, precipitation amounts, current weather, cloud cover, and visibility, along with analyses of pressure fields, streamlines, and dew point temperatures. Upper air height analyses, radiosonde plots (Stuve), and cross-section analyses also helped determine appropriate sampling altitudes. Pre-flight and in-flight surface and upper air data were saved on magnetic tape. Cassettes containing satellite imagery from the Sony archive system were saved for later examination. The archived data are then used to document the synoptic situation.

The mode of operation was similar for the Icing program, a study directed at observing and measuring the accumulation of ice on an in-flight aircraft. Using the same aircraft as in the LSCS study, flights were conducted to sample over any one of 12 radiosonde stations within a 300-mile radius of Wright-Patterson AFB (W-PAFB), OH. Sequences of McIDAS imagery (visible and IR), 6-hour surface station listings, Stuve diagrams, upper air height analyses, and the new icing program plots helped determine if suitable icing conditions were present in the study area. Again, pre-flight and in-flight data were archived on tape and printouts for later inspection.

The Tactical Weapons Support System program is aimed at developing a Tactical Decision Aid (TDA), which will use weather and other geophysical information to determine and predict if certain environmental factors (e.g., IR target-to-background contrast, atmospheric transmission) are conducive to the deployment of specific precision-guided munitions in the tactical situation. Using an instrumented KC-135 aircraft operating out of W-PAFB, a test flight was conducted in September to obtain scene contrast data over a selected target area. McIDAS was able to provide visible and infrared satellite imagery loops, surface data listings for 30 stations

in and adjacent to the target area, upper air height analyses, and Stuve plot displays from the Huntington, WV, Dayton, OH and Pittsburgh radio-sonde stations. Data were collected for a week prior to the flight to establish weather trends. Appropriate pre-flight and in-flight data were archived on tapes and printouts.

Daily archiving of GOES/SMS satellite transmissions began in 1980 with acquisition of the Sony cassette recorders. By means of two 24-hour timers, one recorder was set to operate from 1200Z to 1700Z and the other recorder from 1700Z to 2200Z. Each cassette tape holds five hours of satellite transmissions. The tapes are archived for approximately a month and then recorded-over if there were no requests for particular data. Tapes containing interesting weather phenomena (hurricanes, squall lines, severe storms, volcano effects) are permanently archived. Additional data archiving is accomplished with the Off-line Data Ingest System (ODIS), a microprocessor-controlled tape drive configured as a peripheral device of the McIDAS facility. The ODIS collects one-mile visible, four-mile IR images centered over eastern Pennsylvania, at hourly intervals from 1400Z to 2100Z. Data are collected at half-hourly intervals if particularly interesting or severe weather is present in the study area. Data are then analyzed on the AFGL central computer to calculate brightness counts, cloud motion vectors, and IR temperatures.

### III. System Operability

During 1980 the McIDAS facility was operated 243 out of a possible 248 scheduled working days, for an availability of 98 percent (see Figure D-1). Of the five "down" days, only one was due to a component failure; the other four were caused by painting of the 24-ft. antenna dish, which prevented reception of satellite transmissions.

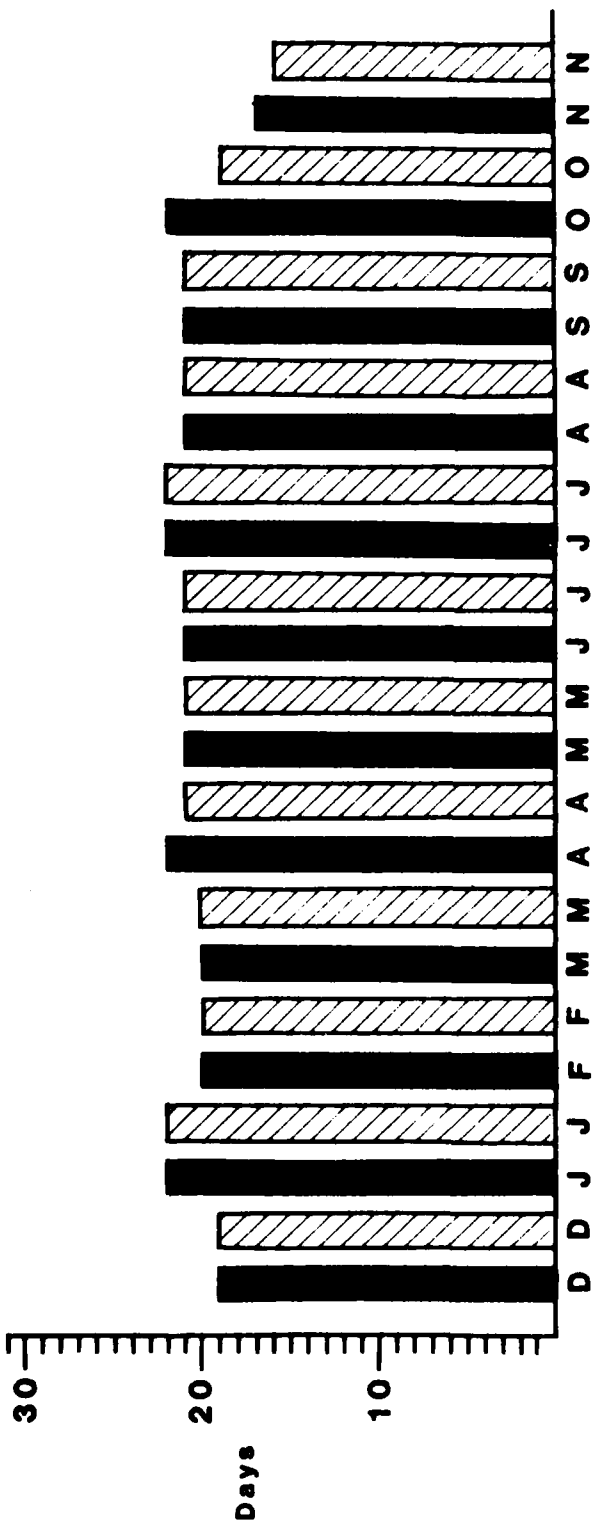
### IV. Applications Software

SASC McIDAS software efforts consisted of three types of activities: debugging existing software, expanding the capabilities of operational programs through addition of new options, and development of new programs.

The main body of system and applications software for the McIDAS was

■ number of days in a month, excluding holidays and  
weekends, when the facility was expected to be operational  
Total 248

■ number of days in a month that the facility was operational  
Total 243



Dec. 1, 1979 through Nov. 30, 1980

Figure D-1. MCIDAS operability during contract year.

written at the University of Wisconsin, whose Space Science and Engineering Center developed the McIDAS. However, many modules required modification to allow for configurational differences at AFGL. Others contained errors introduced by imperfect copying of the original programs, and a few of the most recent additions, received from the University of Wisconsin in an early stage of development, required correction of logic faults.

In order to adapt the original applications software to the specialized needs of AFGL and SASC scientists, new options were added by SASC to many existing programs. These additions increased the versatility of NOWCASTING programs (used to decode, store, analyze, and display conventional surface and upper air data received via a high speed FAA data line), expanded the graphics capabilities to include storage on television frames through a plot display file, and improved speed and accuracy of the navigation fine-tuning process.

New programs unique to the AFGL McIDAS and specifically designed to support current research projects were incorporated into the system. In order to expand the data base upon which imagery information extraction techniques are tested, data ingestion software for two geostationary satellite imagery archives (a 30-day rotating archive of full resolution hemispheric data from the video cassette archiving system, and a permanent ongoing collection of 9-track tapes covering the New England region recorded by the ODIS) was developed.

A new program by SASC was added to McIDAS to assist forecasters in estimating the probability, type, and intensity of aircraft icing at varying altitudes. The algorithm developed was based on a sequence of operational procedures used by Air Weather Service forecasters.<sup>3</sup> Upper air sounding data are used to estimate liquid water content, layer stability, and temperature for correlation with empirically derived icing probabilities.

A major addition to McIDAS software was the Mesoscale Forecasting Facility (MFF), developed by SASC as part of a program of preliminary testing and examination of the feasibility of using a man-interactive system in the preparation of short-range terminal forecasts. McIDAS was used to simulate many aspects of the interactive minicomputer-based display sys-

<sup>3</sup>AWS, 1980: Forecasters' guide on aircraft icing. Technical Report AWS/TR-80/001. Scott AFB, IL.

tem envisioned for the Automated Weather Distribution System (AWDS) planned for Air Weather Service's Base Weather Stations by the mid-1980's and the Satellite Data Handling System (SDHS) planned for the Air Force Global Weather Central.

The MFF is a "menu-driven" system designed to assist in preparing, executing, and verifying short-range forecasts. A series of questions and instruction pages is generated which assists the forecaster in examination of current weather data, formulation of 1-, 3-, and 6-hour probability forecasts, insertion of predictions into personalized data files, verification of forecasts, and later recall for evaluation of performance.<sup>4</sup>

A nine-month test (January-September 1980) was conducted by AFGL and SASC meteorologists to evaluate the utility of the interactive approach. Fifteen researchers with varying degrees of forecasting expertise participated in the program. Three teams performed the forecasting functions on a weekly rotating basis.

The exercise was structured in the form of a daily map discussion led by the Chief Forecaster of the Day, a role assumed by each team member one day during the week. The Chief's primary responsibility was preparation of a forecast problem for consideration by the team. Based on an assessment of that day's weather, the Chief selected a station which provided an interesting mesoscale forecasting situation, and three forecast components. Predictand options included wind speed, wind direction, gusts, visibility, cloud cover, ceiling height, temperature, dew point temperature, and weather. A map file of appropriate weather information was prepared for use in the group discussion. Data sources available through the MFF included conventional surface and upper air observations (Services A and C) and real-time GOES satellite imagery (visible and infrared channels). A wide range of objective analysis and display routines was provided along with image looping and data overlay capabilities for combining conventional and satellite data. Following the map discussion, each forecaster entered predicted values of the assigned parameters for forecast lengths of 1, 3, and 6 hours. Verification and scoring of individual forecasts were performed the following day.

At the end of the test period, a constructive review of the experiment was conducted to evaluate the advantages and disadvantages of an AWDS/

<sup>4</sup> See Gerlach, ed. (1980), pp. 49-73, for a detailed description of the MFF.

SDHS/MFP system for operational met-watch and short-range prediction. An assessment was also made of future directions the project should take toward the objectives of formulating and testing mesoscale nowcasting and forecasting techniques for the AWDS/SDHS era.

Among the advantages cited by MFP participants was the flexibility in analyzing and displaying conventional data made possible through an interactive system. Hourly surface charts, regional displays, upper air soundings, and derived fields such as divergence, vorticity, and temperature advection are examples of the tailored products shown to be useful that are not available on standard facsimile charts. Instant recall of observations ordered by time, station, region, or weather type was found to be an improvement over conventional modes of display. The addition of real-time satellite imagery alone, in time lapse sequences, and in combination with surface and RAOB reports, was a valuable expansion of the mesoscale data base. Other comments noted the advantages of the plot display file for instantaneous recall of displays and time sequencing of surface observations, and reduced or eliminated dependence on paper products.

Disadvantages included the deficiency in mesoscale information caused by coarse spacing of the operational reporting network and lack of radar data. Bad navigation on rare occasions rendered satellite imagery misleading. Several of the more experienced forecasters had problems adjusting to the new display format, expressing difficulty in obtaining an integrated understanding of the weather situation when limited to one chart at a time. It was suggested that the addition of one or more monitors would alleviate the problem by allowing coincident display of several analyses. Limitations in screen size, resolution, and color options were mentioned as undesirable features of the system, along with such mechanical difficulties as occasional flooding of the screen and delays while graphics were produced. It was suggested that a means of subjectively modifying objectively analyzed fields was needed to take advantage of independent information and the experience of the forecaster.

Examination of verification statistics for the test period revealed a general trend toward decreasing skill with increasing forecast length, as expected. A wide range of predictability among the various forecast parameters was indicated, with greatest success achieved in predicting dew point temperature, visibility, and temperature, and least skill in predicting ceiling height and wind direction. Firm conclusions were restricted

by the small sample size.

The MFF experience was a successful first step in evaluating the advantages and disadvantages of an interactive facility for producing short-range forecasts. The resulting recommendations provide a basis for continued research into the kinds of data, displays, and capabilities which will be supplied to AWDS-era forecasters.

## E. WEATHER RADAR TECHNIQUES

### I. Wind Retrieval

Ability to derive automatically the fields of motion within and about severe storms during single radar operations is highly desirable. Several approaches to this problem have been proposed, but as yet none has been tested operationally.

Smythe (1980)<sup>1</sup> presented a pattern recognition technique for retrieving nearly horizontal velocity vectors in clear air by cross-correlating data from two consecutive scans. Even though the Doppler radar is blind to motions perpendicular to its narrow beam, when this technique is used, cross-radial as well as along-radial components of velocity may be derived.

Software associated with the wind retrieval technique was modified for and coded on the Interdata 7/32 minicomputer system at the AFGL Weather Radar Facility. In the process of implementing this software, several problems were encountered by SASC radar meteorologists. These were in part due to system size and compiler differences.

Also, during implementation the software was modified to improve efficiency. Earlier, three jobs were run to obtain the finished product; at AFGL, the first two programs were merged by SASC and the process was reduced to two jobs. One program prepares digitized data for the second program's correlation analysis and transforms the digitized data to scalar data.

Two software versions of the technique had been previously developed. One correlates Doppler radial velocities, the other reflectivities or spectral widths. In both versions, radial velocities are used to determine radial displacements of small regions during the time elapsed between scans. Modification of the first program, which transforms the digitized data to scalar data, was initiated by SASC to provide the analysis program with either velocities and reflectivities or velocities and spectral widths. When finished, the modified program could be interfaced with the

<sup>1</sup>Smythe, G.R., 1980: The retrieval of mesoscale horizontal winds using a single Doppler radar. *Preprints, 19th Conference on Radar Meteorology*, AMS, Boston; pp. 250-255.

reflectivity and spectral width correlation program. Wind file is could then be produced from the ensuing analyses.

The pattern recognition technique was applied to data collected on May 2, 1978 in Norman, OK during the approach and passage of a gust front. Results from several analyses indicated the presence of the gust front. Doppler radial velocities were correlated for these analyses.

Development of a real-time version of the technique, requiring less core memory, was also initiated by SASC. This involves dividing the analysis program into two parts: the first program partitions the first scan into small regions, computes the variance and radial displacement of each region, and stores this information for each small region on separate disk files. This processing is completed before the second scan is collected.

The second program uses the stored information to find equally dimensioned regions of the second scan (collected at the same elevation angle as the first scan) and determines the covariances between data of these regions and data of radially and azimuthally displaced areas of the first scan. It also computes variances of the second scan regions and sorts and evaluates the many correlation coefficients computed. Finally, it produces a display of the vector wind field.

Additionally, at the end of the contract period two curves were being least-squares fitted to the correlation data. The curves are an exponentially decaying cosinusoid and a third order polynomial. It was expected that one curve or the other would properly smooth the correlation field and perhaps give a more precise estimate of the locations of the end points of the wind vectors.

## II. Real-Time Storm Cell Detection and Tracking

This SASC effort was to develop a real-time software technique for the detection and tracking of significant storm cells. The processing algorithm originally developed by Crane<sup>2</sup> extracts the essential information required to describe the organization, development, and motion of the storm system. This information includes the characteristics of the active cells

<sup>2</sup>Crane, R.K., 1979: Automatic cell detection and tracking, IEEE Trans. on Geoscience Electronics, GE-17, 250-262.

within the storm system, the clusters of cells, the fixed-threshold contours or echo regions that encompass the cells, and the complexes of echo regions that comprise the storm system.

The algorithm was modified in 1979 for use on the Interdata 7/32 on-site computer of AFGL. This modified (1979) program is able to operate over a wide range of reflectivity thresholds. In order, however, to reduce the number of cells processed in the computer, thereby improving operating speed for real-time operations, SASC raised the reflectivity threshold to 40 dBz. Despite this improvement, the current running time for reflectivity processing is 130 seconds per azimuth scan. This is not satisfactory for real-time operation, which requires 40 seconds per azimuth scan.

The SASC developmental work was therefore organized into three tasks:

- a. To check the accuracy of the original algorithm,
- b. To implement the modified (1979) program for real-time use, and
- c. To test yet-to-be-developed software for real-time operation.

Under the contract efforts were directed toward tasks a and b.

The first step in task a was to provide data from the pulse pair recorder interface (PPRI) as input to the original tracking algorithm, using a program that transforms digitized data to reflectivity values.<sup>3</sup> This digitized program is also capable of decoding the variance and velocity values. A double buffering technique developed by SASC was introduced into the digitized program to increase input/output speed. A magnetic disk is used as the output device because the data transfer speed of the tape drive is relatively slow. Therefore, two additional programs were developed: DSCTOTP, which transfers the data from disk to tape, and DIGRD, which prints the data from disk or tape.

Concurrently, the output format of the digitized program was modified to conform to the Common Doppler Radar Exchange Format adopted by the Doppler radar community. This involved adding seven ancillary data header blocks to the decoded radar data blocks.

For task b, the logic of the modified (1979) program was examined and

<sup>3</sup>Boak, T.I.S., L.J. Jagodnik, R.B. Marshall, D. Riceman, and M. Young, 1977: Tracking and significance estimator. Final Report, Raytheon Company.

redundant execution steps were removed. Timing analysis showed that the speed of the data acquisition subroutine and peak calculation subroutine needed to be increased for real-time implementation. Since coding these subroutines in assembler language would reduce the time required for indirect storage addressing and bit manipulation, SASC developed Common Assembly Language (CAL) macros for them. Such program modularization, that is, dividing large programs into subprograms which are developed and debugged individually, conforms to good programming practice.

### III. Detection of Turbulence in Thunderstorms using Radar Methods

#### (A). Introduction

The detection of turbulence in thunderstorms by remote methods has been a subject of investigation for many years. Early studies, relying on observations from penetrating aircraft, attempted to correlate turbulence encounters with radar storm features. The general conclusion was that the frequency of occurrence of moderate to severe turbulence increased markedly with increasing storm radar echo intensity (dBz), with 40 dBz a rough threshold value for development of such turbulence somewhere in the storm. Further observation indicated that severe turbulence was widely distributed in storms whenever the intensity indicated damaging hail (about 50 dBz), with turbulence encounters outside high intensity cores being as frequent as those within (Lee, 1967).<sup>1</sup> This was particularly evident within thunderstorm lines where severe turbulence was frequently encountered in low echo intensity regions between individual storms. The conclusion was that storm echo intensity was an indicator of the presence of turbulence, but it did not reliably measure its strength nor locate its position.

In light of these results and with continued development in Doppler radar techniques, emphasis was placed on finding kinematic signatures of hazardous zones within thunderstorms. Armstrong and Donaldson (1969)<sup>2</sup> developed the Plan Shear Indicator (PSI), which was able to detect regions

<sup>1</sup>Lee, J.T., 1967: Atmospheric turbulence and radar echoes, in Technical Memorandum IERTM - NSSL, 32, Norman, OK, pp. 1-9.

<sup>2</sup>Armstrong, G., and R. Donaldson, Jr., 1969: Plan Shear Indicator for real-time Doppler radar identification of hazardous storm winds, J. Appl. Meteor., 8, pp. 376-383.

of strong shear of the radial wind. Lee and Kraus (1975)<sup>3</sup>, by comparing PSI and penetrating aircraft observations, found good correlation between regions of strong shear of the radial wind and severe turbulent events. Radar data of Frisch and Strauch (1976) suggested that high turbulent intensity may not necessarily be correlated with zones of high shear of the radial wind, but when present, may be found in regions exhibiting large Doppler spectrum variance. Later Lee (1977)<sup>4</sup> also found good correlation between regions of severe turbulence and large spectrum variance. Thus, present attempts are being directed at using Doppler spectrum variance as a turbulence indicator.

The turbulent contribution to Doppler spectrum variance is a function of the turbulent intensity (or alternatively the eddy dissipation rate and the turbulent outer scale), range of the observation volume from the radar, and precipitation environment. The manner in which these effects combine is not well known, and thus, the interpretation of this indicator is not yet completely understood. The aim of this research is to clarify the relationship between Doppler spectrum variance and these parameters and to develop a more reliable radar turbulence detection technique.

This report focuses on results of theoretical investigations and data analyses performed by SASC during the period May, 1979 to June, 1980. Primary topics discussed are: 1) the response of a distribution of precipitation particles to various ranges of scales of turbulent motion; 2) the relationship between eddy dissipation rate and Doppler spectrum variance as a function of the turbulent scale regime and precipitation environment; and 3) the distribution of local turbulence regimes within thunderstorms as delineated by aircraft data. Finally, since one of the ultimate goals of this work is to revise a methodology for turbulence detection by incoherent radar, a possible method by which non-Doppler radar may estimate wind shear for the purpose of removing its contaminating effects from the Doppler spectrum variance will be briefly discussed. Results of these in-

<sup>3</sup>Lee, J.T., and M. Kraus, 1975: Plan Shear Indicator and aircraft measurements of thunderstorm turbulence: experimental results. Preprints, 16th Radar Meteorology Conference, AMS, Boston; pp. 337-340.

<sup>4</sup>Lee, J.T., 1977: Application of Doppler weather radar to turbulence measurements which affect aircraft. Final Report FAA-RD-77-145 to Systems Research and Development Service, FAA, Washington, D.C., 20 pp.

vestigations point to the need for further data analysis for verification and selection of practical solutions.

#### (B). Theoretical Investigations

The response of precipitation particles to turbulent air motions is of fundamental importance since the Doppler radar velocity is generally equated to the radial component (component along the radar viewing direction) of the environmental wind. However, the Doppler velocity is actually the power-weighted mean of the Doppler spectrum, which is formed from measurements of the radial velocities of the precipitation particles within the radar pulse volume, with the spectral power at each spectral velocity value proportional to the sum of the sixth powers of the diameters of the precipitation tracers moving with that radial velocity value. It is suspected that a sizeable portion of Doppler spectrum power may be supplied by tracers which, because of their large inertia (e.g., large raindrops), do not follow turbulent fluctuations faithfully. If so, then an incorrect estimate of the turbulent motion (e.g., Doppler spectrum mean and variance) is obtained. Thus, one is interested in determining the response of a distribution of particles to various scales of motion. This may be obtained by appropriately summing the individual responses of the particles comprising the distribution.

Consider a single particle. Its equation of motion may be written as

$$m_D \frac{d\vec{v}_D}{dT} = m_a \frac{d\vec{v}_a}{dT} + m_D g \left(1 - \frac{\rho_a}{\rho_D}\right) - 6\pi a \mu (\vec{v}_D - \vec{v}_a) \frac{C_d N_{Re}}{24} \quad (1)$$

where  $m_d$ ,  $\vec{v}_d$ ,  $\rho_d$ , and  $a$  are the mass, velocity, density, and radius of the particle. Air density is  $\rho_a$ ,  $m_a$  is the mass of displaced air, and  $\vec{v}_a$  is the air velocity in the vicinity of the particle. Kinematic viscosity is  $\mu$ , gravitational acceleration is  $\vec{g}$ , and  $C_d$  and  $N_{Re}$  ( $= 2 Re$ ) are the drag coefficient and alternate Reynolds number of the particle. The coefficient  $C_d N_{Re}/24$  is a catch-all term and is actually related to fluid acceleration and past particle motion (Pruppacher and Klett, 1978).<sup>5</sup> This equation simply relates the net force acting on the particle to the pressure, buoyancy-corrected gravity, and drag terms. Equation 1 may be written as

<sup>5</sup>Pruppacher, H.R., and J.D. Klett, 1971: Microphysics of Clouds and Precipitation, Boston, D. Reidel Publishing Co., 715 pp.

$$m_D \frac{d\vec{v}_D}{dT} = m_a \frac{d\vec{v}_a}{dT} + m_D \vec{g} \left(1 - \frac{\rho_a}{\rho_D}\right) - (\vec{v}_D - \vec{v}_a)/\tau \quad (2)$$

where  $\tau = \frac{8 \alpha \rho_D}{3 C_d |\vec{v}_D - \vec{v}_a| \rho_a}$  . (3)

Actual solution of Equation 2 requires application of numerical methods, since  $C_d$  is dependent on  $(\vec{v}_D - \vec{v}_a)$ . To obtain a general analytical solution for the particle response it is necessary to make some simplifying assumption concerning the drag force. For this purpose it is assumed that, on the average, the particle is settling at its terminal fallspeed ( $V_T$ ). The drag force in Equation 2 may be replaced by its average value. Then following Stackpole (1961)<sup>6</sup> the following relation is applicable:

$$\tau = \frac{V_T}{g} . \quad (4)$$

Neglecting particle growth and the variation of air density with height,  $\tau$  is a constant for each particle. Note that this assumption means that the drag coefficient is replaced by the value attained when the particle is settling at its normal terminal fallspeed in still air, and thus it is a slightly averaged particle response that may be estimated.

In applying Equation 2 to a turbulent field, one generally considers turbulence as composed of a random collection of eddies having a range of scales (e.g., wavelengths  $\lambda$ ). Mathematically, one may view this collection as a series of harmonic functions of varying frequency ( $\omega$ ) or wave-number ( $K = 2\pi/\lambda$ ), having random amplitude and combining to produce the observed turbulent structure. The response of a particle to a turbulent gust may therefore be considered the result of a superposition of the particle's responses to this collection of harmonic functions, or eddies.

The form of the particle response to a single such function may be seen by considering one dimension (horizontal) and introducing an air velocity  $v_a = V_0 \cos \omega T$  (5)

into Equation 2. The particle velocity is found to be

$$v_d = V_0 \left[ (1 + \omega^2 \tau^2 \rho_0^2)^{1/2} / (1 + \omega^2 \tau^2)^{1/2} \right] \cos (\omega T + \omega \tau (\rho_0 - 1)) + A e^{-\frac{T}{\tau}} \quad (6)$$

Stackpole, J.D., 1961: The effectiveness of raindrops as turbulence sensors. Proceedings, 9th Weather Radar Conference, AMS, Boston, pp. 212-217.

where  $\rho_o = \frac{\rho_a}{\rho_d}$  and  $\omega\tau < 1$  is assumed. This last condition is met for all environments except those combining large particle size and turbulent scale  $\leq 60$  m. (Even then, the energy content of the turbulent field at these scales is small in relation to larger scales and need not be considered further.) The first term shows that the particle velocity is reduced in amplitude and phase-shifted relative to the air velocity. The second term is a transient term. (These effects are generally small.) In reality, there is no way of actually incorporating the phase and transient information into actual motion of the particles which enter any given region of turbulence, since their present motion is also dependent upon their motion prior to entering this region, and this is unknown. Thus, only the amplitude response will be considered.

It is necessary to map this response function from dependence upon frequency to turbulent scale, since frequency is dependent upon the relative speed of the atmospheric structure and the sensing instrument (here the particles), and therefore is an artificial turbulent parameter. In a manner similar to Taylor's hypothesis, one may form a relationship between turbulent wavenumber, radian frequency, and particle terminal fallspeed as

$$\omega = \vec{V}_T \cdot \vec{K} = V_T K_z \quad (7)$$

resulting in the response function taking the form

$$V_d/V_a \doteq 1/(1 + K_z^2 V_T^4 / g^2)^{\frac{1}{2}} \quad (8)$$

where  $\rho_o \approx 10^{-3}$  has been assumed. This relationship was first obtained by Stackpole and states that as the particle size increases ( $V_T$  increases) the response to turbulent motions having any given apparent scale  $\lambda$  ( $= K_z / 2\pi$ ) decreases. Conversely, a particle of given size ( $V_T$  constant) exhibits decreasing response to decreasing scale. The term "apparent scale" has been used to signify that the particles are responding to the field which is the projection of the 3-D turbulent field upon the z-axis and that there may not be a one to one correspondence of features in the 3-D field to those observed in the 1-D field.

It is instructive to consider the effect this particle response has upon the actual mean total velocity variance contained by a particle distribution when in a turbulent field. This is given by

$$\text{VAR}_{pD} = \langle u^2 + v^2 + w^2 \rangle = \int_{K_{\min}}^{K_{\max}} E(K) W(K) dK \quad (9)$$

where the air energy density (9) is assumed given by the Kolmogorov relation

$$E(K) = C\epsilon^{2/3} K^{-5/3} \quad (10)$$

in which  $C$  is a known constant,  $\epsilon$  is the eddy dissipation rate, and  $K = |\vec{K}|$ . The particle distribution response is

$$W(K) = 2 \int \left\{ \left[ (qN(D) \tan(KV_T^2/q)) / KV_T^2 \right] \right\} dD \int N(D) dD \quad (11)$$

where the particle number density and fallspeed are given by

$$N(D) = N_0 e^{-\Lambda D} \quad (12)$$

and

$$V_T = aD^b \quad (13)$$

respectively. Figure E-1 shows this variance ( $\text{VAR}_{pD}$ ), normalized to the air turbulent variance  $\text{VAR}_a$  where

$$\text{VAR}_a = 2 \int E(K) dK. \quad (14)$$

The constant parameters in Equations 11 - 14 are  $a = 1690 \text{ cm}^4 \text{ sec}^{-1}$ ,  $b = .6$ ,  $D_{\min} = .005 \text{ cm}$ ,  $D_{\max} = .5 \text{ cm}$ , and  $K_{\max} = 2\pi \text{ cm}^{-1}$  (corresponding to a minimum turbulent scale of 1 cm). Parameters  $K_{\min}$  ( $= 2\pi/\lambda_0$ ) corresponding to a turbulent outer scale  $\lambda_0$  and the particle distribution slope  $\Lambda$  are the independent variables.

This figure shows that the mean turbulent variance of the particles is typically 95 percent (or greater) of the air value, for all precipitation environments (e.g., heavy rain  $\Lambda = 10 \text{ cm}^{-1}$  to light rain  $\Lambda = 60 \text{ cm}^{-1}$ ) and outer scales ( $\lambda_0$ ) greater than 500 m.

This figure demonstrates that even though individual particles (e.g., large drops) may not respond well to small scales of motion, the actual mean turbulent velocity variance of the particle distribution is generally a good measure of the atmospheric value. Unfortunately, the radar does not weight the particles identically, as this calculation assumes, but rather weights the particles according to the sixth power of drop diameter.

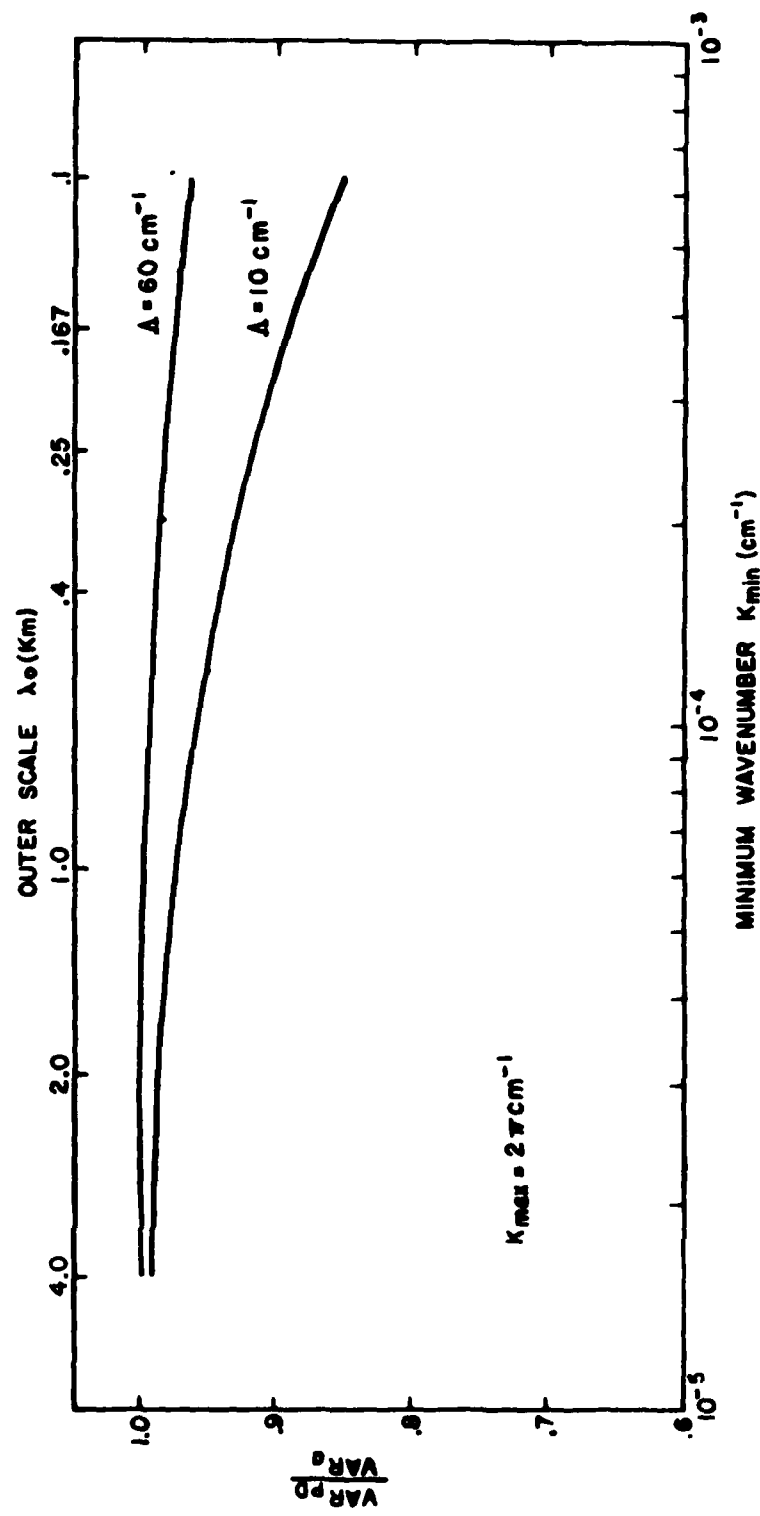


Figure E-1. Ratio of true total (3-D) precipitation motion variance  $\text{VAR}_{PD}$  to air motion variance ( $\text{VAR}_a$ ) for precipitation environments  $\Lambda = 10 - 60 \text{ cm}^{-1}$ .

The total 3-D radar measurable turbulent variance is given by

$$\text{VAR}_{pD} = \langle u^2 + v^2 + w^2 \rangle = \int_{K_{\min}}^{K_{\max}} E(K) W_1(K) dK \quad (15)$$

where

$$W_1(K) = 2 \int \left\{ \left[ (gN(D)D^6 \tan(KV_T^2/\alpha)) / KV_T^2 \right] \right\} dD / \int N(D) D^6 dD. \quad (16)$$

This quantity, normalized to the actual air turbulent variance, is shown in Figure E-2. It is observed that if the outer scale ( $\lambda_o$ ) extends to a kilometer or more, then the radar can measure 90 to 97 percent of the air motion variance in all precipitation environments. For shorter outer scales, however, particularly in heavy rain situations, the radar estimate may be in significant error. As an example, for  $\Lambda = 10 \text{ cm}^{-1}$  and an outer scale of 250 m, the total radar measurable variance is only about 72 percent of the air value. The striking difference between Figures E-1 and E-2 results from the strong power contribution to the Doppler spectrum from large particles which exhibit poor response characteristics, and demonstrates that the usual assumption of precipitation being perfect tracers of the air motion can lead to radar turbulent energy estimates having significant error. The results demonstrate that imperfect particle response and the finite scale of turbulence must be taken into account if reasonable estimates of turbulent parameters are to be obtained by radar methods. This will be accomplished by modifying the pertinent basic radar relations.

In all that follows the wind environment is considered fully turbulent to clearly obtain the relationship between the radar observed parameters and the turbulent field. The results are also applicable, however, in the presence of a constant background wind.

In general form the Doppler spectrum variance may be written as

$$\text{VAR} = \overline{V_p^2} - \overline{V_p}^2 \quad (17)$$

where  $V_p$  is particle radial velocity and the overbar indicates averaging over the Doppler power spectrum. This relation states that the spectrum variance equals the averaged square of particle radial velocity less the square of the averaged particle radial velocity. More specifically, this equation may be written as

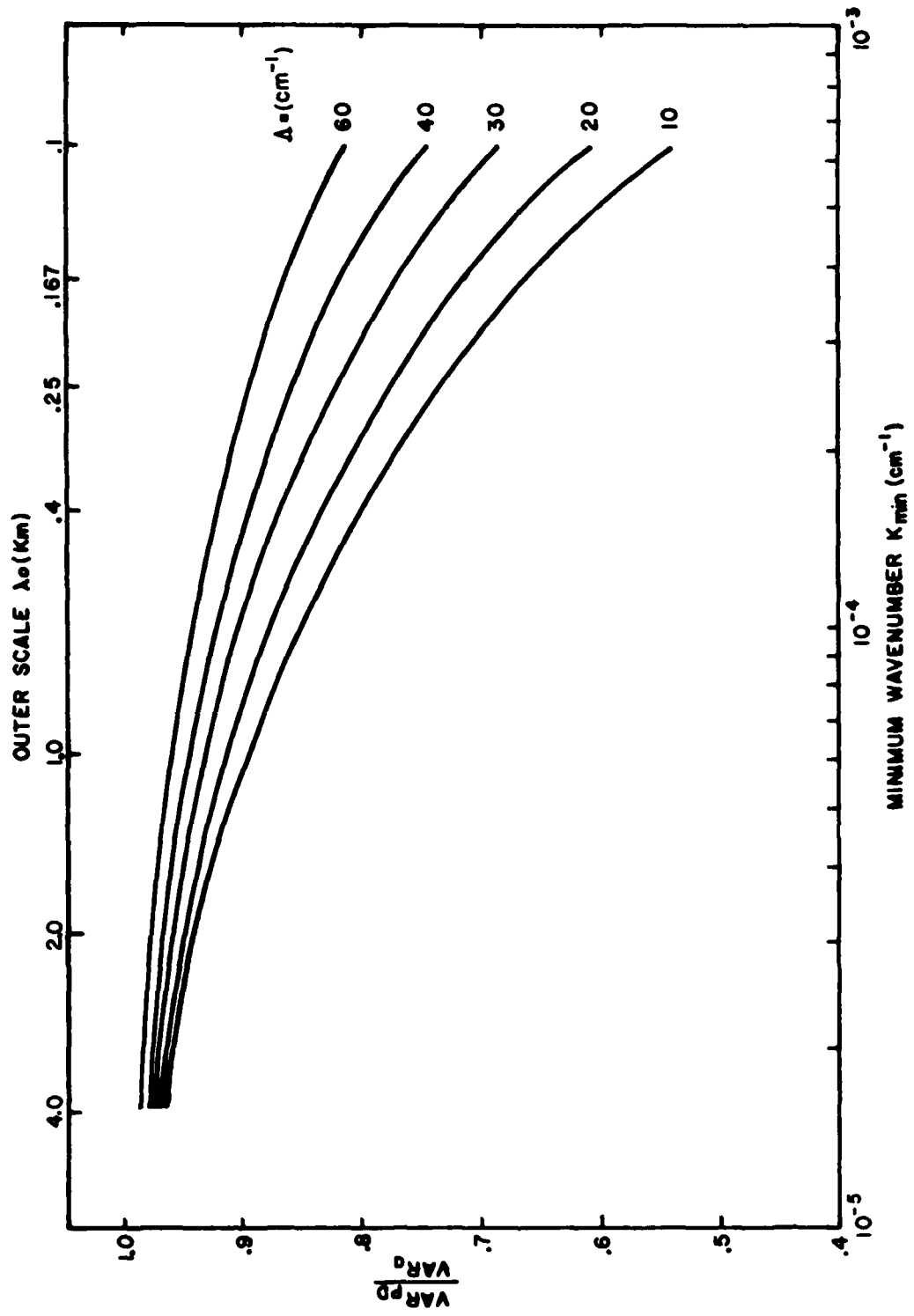


Figure E-2. Ratio of total (3-D) radar measurable turbulent motion variance ( $VAR_{pD}$ ) to air motion variance ( $VAR_a$ ) versus minimum wavevector magnitude (bottom) and outer scale (top). Precipitation environments are  $\Lambda = 10 - 60 \text{ cm}^{-1}$ .

$$\begin{aligned}
 \text{VAR} = & \frac{c_1 \iint v_p^2(\vec{R}) q(v_p, \vec{R}) I(\vec{r}, \vec{R}) dv_p d\vec{R}}{c_1 \iint q(v_p, \vec{R}) I(\vec{r}, \vec{R}) dv_p d\vec{R}} \\
 & - \left[ \frac{c_1 \iint v_p(\vec{R}) q(v_p, \vec{R}) I(\vec{r}, \vec{R}) dv_p d\vec{R}}{c_1 \iint q(v_p, \vec{R}) I(\vec{r}, \vec{R}) dv_p d\vec{R}} \right]^2
 \end{aligned} \quad (18)$$

showing more clearly the power-weighted averaging and pulse volume averaging over available particle radial velocities. Here  $c_1$  is the radar constant,  $q(v_p, \vec{R})$  is the reflectivity of the particles in the volume element  $d\vec{R}$ , (proportional to the sixth power of the partial diameter), located  $\vec{R}$  from the pulse volume center located at  $\vec{r}$  (relative to the radar), and having radial velocities ranging from  $v_p$  to  $v_p + dv_p$ . The term  $c_1 q(v_p, \vec{R}) d\vec{R} dv_p$  is the power back-scattered by these particles to the radar, and  $I(\vec{r}, \vec{R})$  is the two-way beam illumination pattern which is assumed normalized. The integral over  $\vec{R}$  is the integral over the pulse volume, and the  $v_p$  integral is over the total unambiguous velocity range of the radar.

Generally the returned power varies with position within the pulse volume; however, to incorporate the effect of imperfect response and make the above relation tractable, a simplifying assumption is required. It is assumed that during the time the radar samples a given region to form the sample data set (used to form the Doppler power spectrum), a characteristic distribution ( $N_0 e^{-AD}$ ) of particles is swept past each point within the pulse volume. In essence, this states that the reflectivity is constant throughout the pulse volume; i.e.,

$$q(v_p, \vec{R}) = q(v_p) \quad (19)$$

and allows Equation 18 to be re-written as

$$\text{VAR} = \int_{\vec{R}} v_{pD}^2(\vec{R}) I(\vec{r}, \vec{R}) d\vec{R} - \left[ \int_{\vec{R}} v_{pD}(\vec{R}) I(\vec{r}, \vec{R}) d\vec{R} \right]^2 \quad (20)$$

where

$$v_{pD}^2(\vec{R}) = \frac{\int_{V_p} v_p^2(\vec{R}) q(v_p) dV_p}{\int_{V_p} q(v_p) dV_p} \quad (21)$$

and

$$v_{pD}(\vec{R}) = \frac{\int_{V_p} v_p(\vec{R}) q(v_p) dV_p}{\int_{V_p} q(v_p) dV_p} \quad (22)$$

This is essentially the classical definition of Doppler spectrum variance. However, the significant difference here is that  $v_{pD}(\vec{R})$  is the power-weighted imperfect response of the particles, and thus incorporates the concept that during the sampling period, at a given point in space, the various size particles composing the particle distribution exhibit different velocities from each other and the single-valued air velocity at that point. With an ensemble (denoted by  $\langle \rangle$ ) of observations, and noting that ensemble averaging mathematically is a summation and can be brought within the integral, Equation 20 becomes

$$\langle \text{VAR} \rangle = \langle \bar{v}_{pD}^2 \rangle - \langle \bar{v}_{pD} \rangle^2 = \langle v_{pD}^2 \rangle - \text{VAR}_{\bar{v}_{pD}} \quad (23)$$

where now the overbar indicates averaging over the pulse volume and noting that  $\bar{v}_{pD} = 0$ . This states that the average Doppler spectrum variance equals the average one-dimensional power-weighted particle turbulent variance minus the average variance of the Doppler mean velocity. This is a modification of the relation of Rogers and Tripp (1964).<sup>7</sup> It is important to note here that this radar mean particle turbulent variance is not the air turbulent variance, but the power-weighted response of the particle distribution to the air turbulent motions. Similarly, the Doppler mean velocity term also includes the imperfect response function.

To incorporate the response functions it is useful to transform Equation 22 into wavevector space. Srivastava and Atlas (1974)<sup>8</sup> have shown

<sup>7</sup> Rogers, R.R., and B.R. Tripp, 1964: Some radar measurements of turbulence in snow, *J. Appl. Meteor.*, 3, 603-610.

<sup>8</sup> Srivastava, R.C., and D. Atlas, 1974: Effect of finite radar pulse volume on turbulence measurements, *J. Appl. Meteor.*, 13, 472-480.

that the average variance of the Doppler spectrum (Equation 17, for the case of perfect tracers) is given by

$$\langle \text{VAR} \rangle = \int \phi_{11}(\vec{k}) (1 - \phi_I(\vec{k})) d\vec{k} \quad (24)$$

where  $\vec{k}$  is the three-dimensional turbulent wavevector,  $\phi_I(\vec{k}) = (2\pi)^6 F_I(\vec{k}) F_I^*(\vec{k})$  where  $F_I(\vec{k})$  is the Fourier transform of  $I(\vec{r}, \vec{R}, t, \omega)$ .  $\phi_{11}(\vec{k})$  is the turbulent power density function of the radial (1) air velocity component. This relation (Equation 24), however, does not include the particle response functions. Referring back to Equations 19, 20, and 21, the new modified form of this relation becomes

$$\langle \text{VAR} \rangle = \int \phi_{11}(\vec{k}) (R_2(K_z) - R_1(K_z) \phi_I(\vec{k})) d\vec{k} \quad (25)$$

$$R_2(K_z) = \int \frac{e^{-\lambda D_D^6} dD}{(1 + K_z^2 (aD^b)^4 / g^2)} \quad / \quad \int e^{-\lambda D_D^6} dD \quad (26)$$

and

$$R_1(K_z) = \left[ \int \frac{e^{-\lambda D_D^6} dD}{(1 + K_z^2 (aD^b)^4 / g^2)^{1/2}} \quad / \quad \int e^{-\lambda D_D^6} dD \right]^2 \quad (27)$$

where now the power-weighted imperfect response function is explicitly shown. Hence  $R_2(K_z)$ ,  $R_1(K_z)$  are the point turbulent particle variance and squared mean point turbulent velocity weighting factors, respectively. This is the desired result.

The e are a few points to note in this relation. First, the results are dependent only on the slope ( $\lambda$ ) of the particle distribution function and not on the actual particle concentration number  $N_0$ . Secondly, if the pulse volume is decreased in size to a point, (in which case the beam filter function  $\phi_I(\vec{r}, \vec{R})$  behaves as a delta function, for which  $\phi_I(\vec{k})$  becomes unity over all  $\vec{k}$ ), there exists a minimum variance which must always be observed. Its value is given by

$$\langle \text{VAR} \rangle_{\min} = \int \phi_{11}(\vec{k}) (R_2(K_z) - R_1(K_z)) d\vec{k} \quad (28)$$

Numerical calculations show that this term is small and reflects that the two weighting functions are nearly identical in net effect. The existence of this minimum variance is expected, since each point in space is observed for a finite amount of time, during which a distribution of particles having differing radial velocities (because of varying response characteristics) sweeps by and contributes to the Doppler power spectrum.

The variation of these response functions with wavenumber component  $K_z$  is shown in Figures E-3a and E-3b for various particle distribution slopes. These figures show that the power-weighted precipitation response is good for turbulent motions having an apparent scale  $\lambda$  (measured along the z-direction) larger than about 250 m, with virtually no response to scales of motion smaller than about 10 m. As expected, better response is obtained in light rain ( $\lambda = 60 \text{ cm}^{-1}$ ) than in heavy rain ( $\lambda = 20 \text{ cm}^{-1}$ ) environments. It should also be remembered that the response, although excellent, is not perfect for scales greater than 1 km. Finally, note that the differences between Figures E-1 and E-2 result directly from the different response functions, Equations 8 and 26.

Equation 25 may be demonstrated graphically. For mathematical ease, the radar viewing direction is chosen as vertical, resulting in

$$\langle \text{VAR} \rangle = \int (\phi_{zz}(K_z) R_2(K_z) - \phi_{zzf}(K_z) R_1(K_z)) dK_z \quad (29)$$

where

$$\phi_{zz}(K_z) = \iint \phi_{zz}(\vec{K}) dK_x dK_y \quad (30)$$

$$\phi_{zzf}(K_z) = \iint \phi_{zz}(\vec{K}) \phi_I(\vec{K}) dK_x dK_y \quad (31)$$

and

$$\phi_{zz}(\vec{K}) = (1 - \frac{K_z^2}{K^2}) \frac{E(K)}{4\pi K} . \quad (32)$$

Here  $\phi_{zz}(K_z)$  is the true air point one-dimensional longitudinal power spectrum function along the z-direction. Similarly,  $\phi_{zzf}(K_z)$  represents the spectrum that would result from power spectrum analysis of Doppler radial velocities obtained from a set of successive range bins along the radial (close enough so that the pulse volume dimensions may be considered constant) at some range  $r$  from the radar.

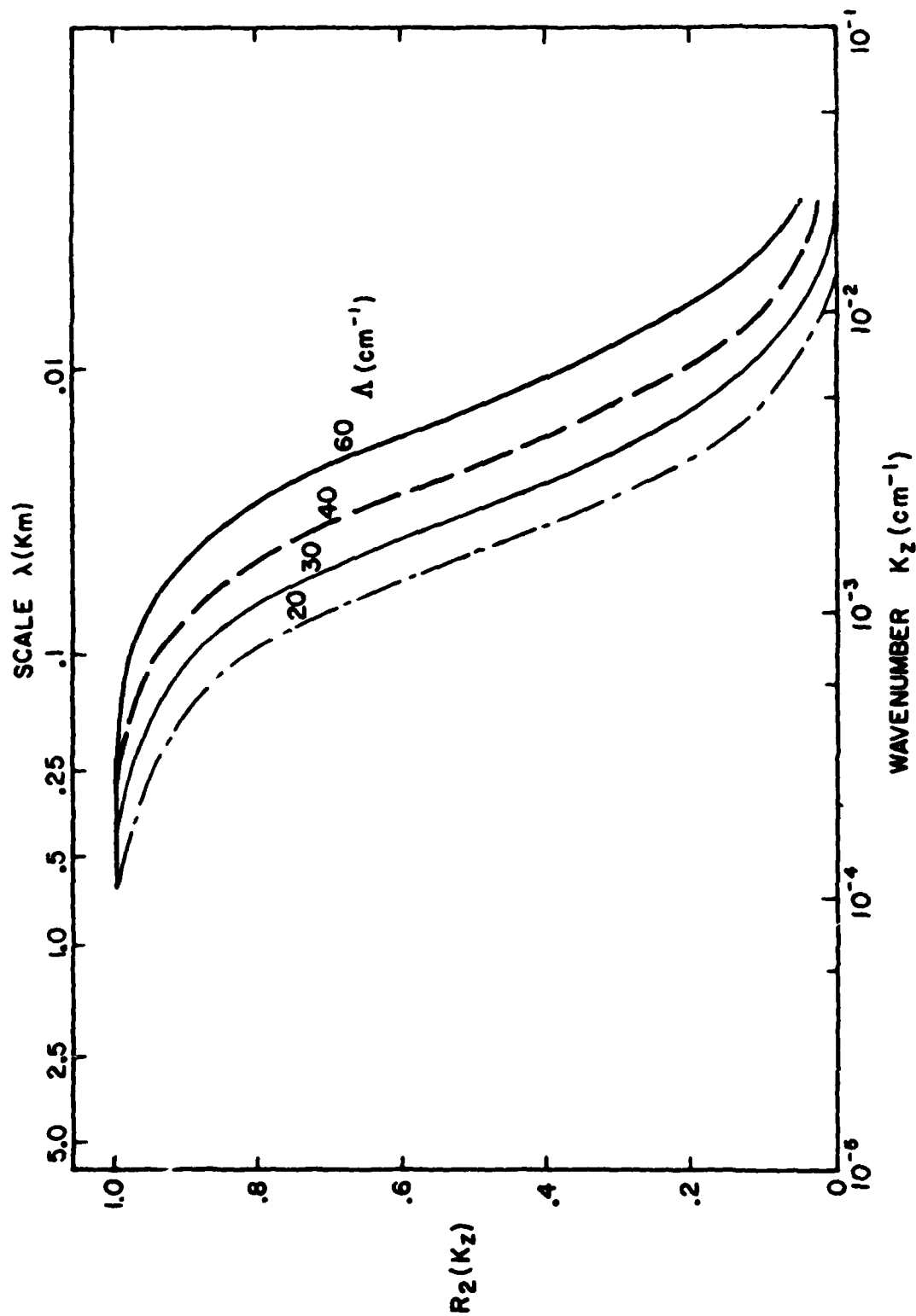


Figure E-3a. Precipitation turbulent motion response function versus  $Z$  wavevector component in precipitation environments  $\Lambda = 20 - 60$  cm<sup>-1</sup>. Equivalent space scale at top. Variance response function  $R_2(K_z)$ .

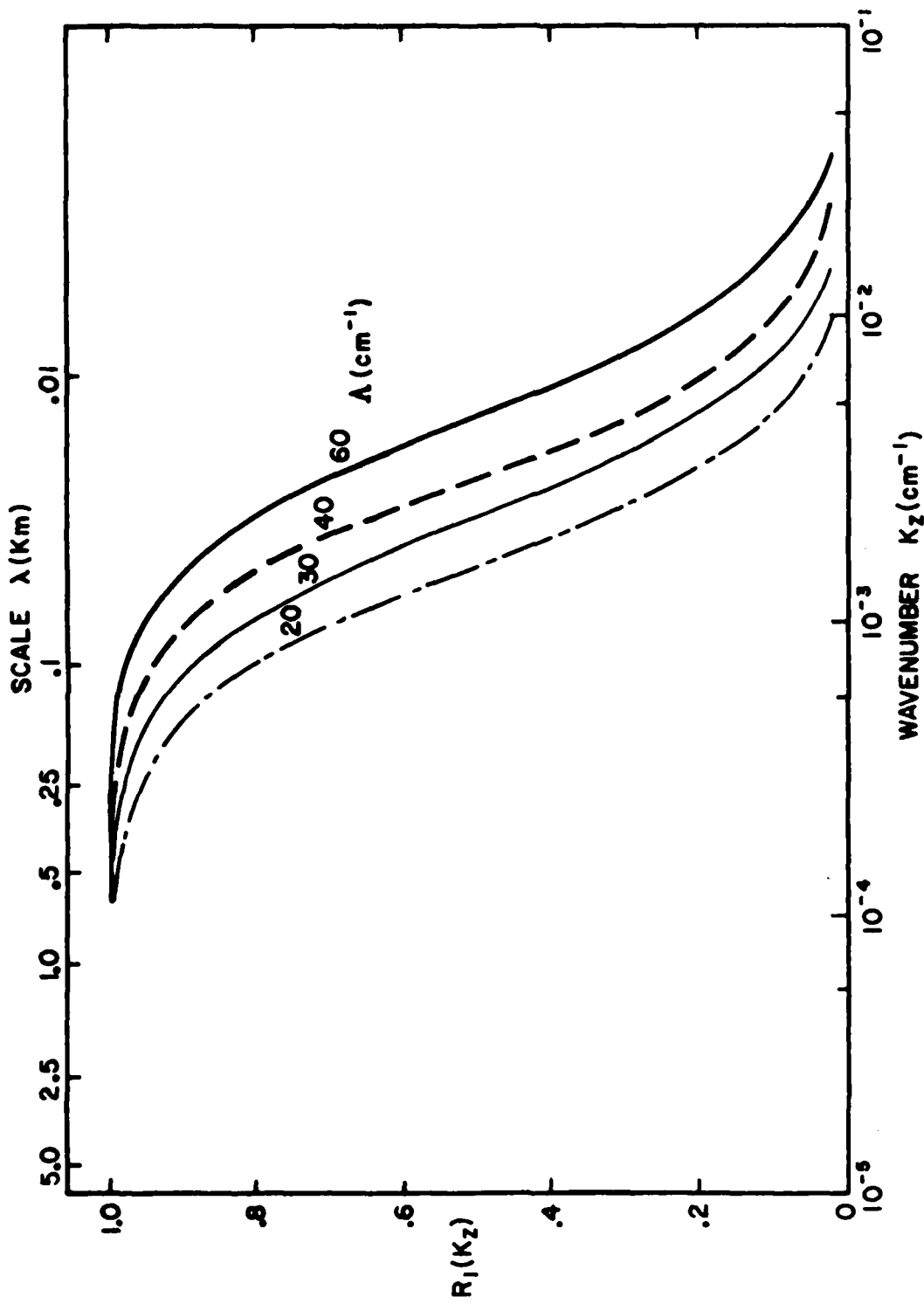


Figure E-3b. Precipitation turbulent motion response function versus  $z$  wavevector component in precipitation environments  $\Lambda = 20 - 60 \text{ cm}^{-1}$ . Equivalent space scale at top. Velocity response function  $R_1(K_z)$ .

Figures E-4a and E-4b show the two component terms of this one-dimensional representation for the two cases of outer scale  $\lambda_o = \infty$ , 1 km. The radar is assumed to have a full half-power beamwidth of one degree and the pulse volume depth is 200 m. The outer curve (point) is the true point turbulent air spectrum  $\phi_{zz}(K_z)$  (Equation 30). The lower solid curves (5, 20, 40, 60, 120) are the corresponding beam-filtered turbulent spectra  $\phi_{zzf}(K_z)$  (Equation 31) for the five ranges mentioned. The lines ( $\Lambda = 10, 60 \text{ cm}^{-1}$ ) represent the modifications to the appropriate curve  $R_2(K_z)$  for point curve;  $R_1(K_z)$  for range curves by introduction of imperfect tracers in rain environments corresponding to  $\Lambda = 10$  and  $60 \text{ cm}^{-1}$ . The precipitation response weighted curves for ranges greater than 20 km are nearly identical to the respective perfect tracer (air) curves and are not drawn.

The Doppler spectrum variance for the case of perfect tracers is given by the area between the perfect tracer point and appropriate range spectral curves. Similarly, for imperfect tracers, the area between the imperfect tracer point and appropriate range curves, for each given particle distribution slope, is the variance in real precipitation environments. Caution must be exercised in interpreting these spectra, since the curves represent the collapse of the three-dimensional turbulent spectrum onto the  $K_z$  axis. However, the figures clearly show: a) the loss of energy at small spectral scales (large  $K_z$ ) in precipitation environments, b) the region of abrupt change in slope, the knee of the curve, is a rough measure of the outer turbulent scale length, and c) imperfect particle response has only a small effect on power spectra determined from radar data where the radar range is greater than about 20 km. This last observation results from the strong pulse volume filtering action at these ranges reducing the amplitude of the power spectrum so much that further reduction from imperfect particle response is not significant.

Finally, calculations indicate that in light rain situations, the total radar measurable variance is partitioned equally between  $x = y \approx z$  components. In heavy rain environments, the horizontal variance components are noticeably smaller than the vertical component for outer scale lengths less than about .25 km ( $\langle u^2 \rangle / \langle w^2 \rangle = .95, .91, .88$  for  $\lambda_o = .5, .25, .167 \text{ km}$  respectively). This is a real effect and results from the response function being entirely dependent upon  $K_z$ . However, a more exact functional form, allowing for some slight direct dependence on  $K_x, K_y$  would presum-

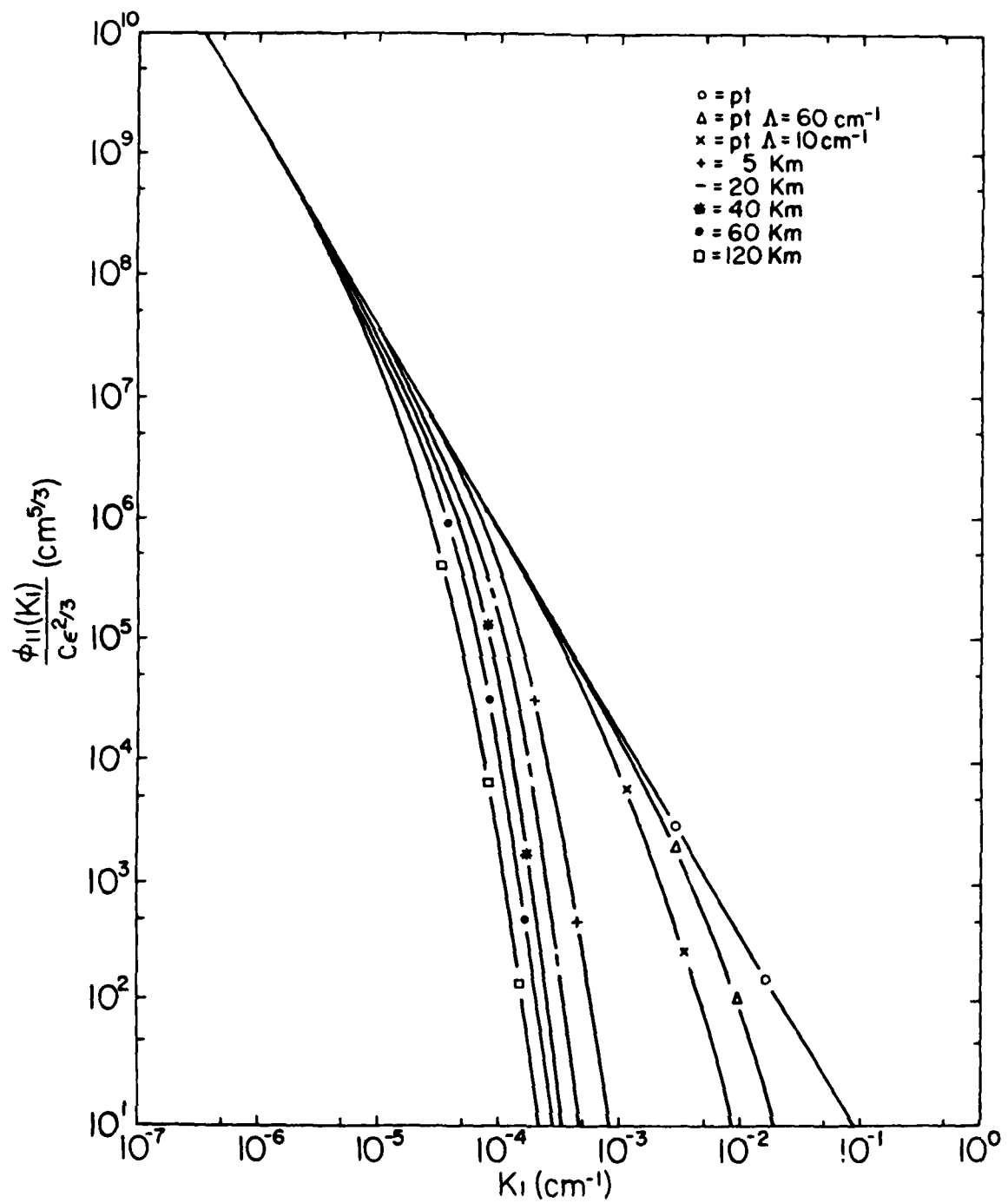


Figure E-4a. Turbulent power spectrum components of radar Doppler spectrum variance. Curves labeled pt. represent perfect tracer (pt.) and imperfect tracer ( $\Lambda = 10 - 60 \text{ cm}^{-1}$ ) precipitation environments. Curves labeled 5,20,40,60,120 km are radar beam filtered spectra for perfect tracers for ranges indicated. Full half-power beamwidth is 1 degree and pulse volume depth is 200 m. Outer scale  $\lambda_o \approx 10^{20} \text{ km}$ .

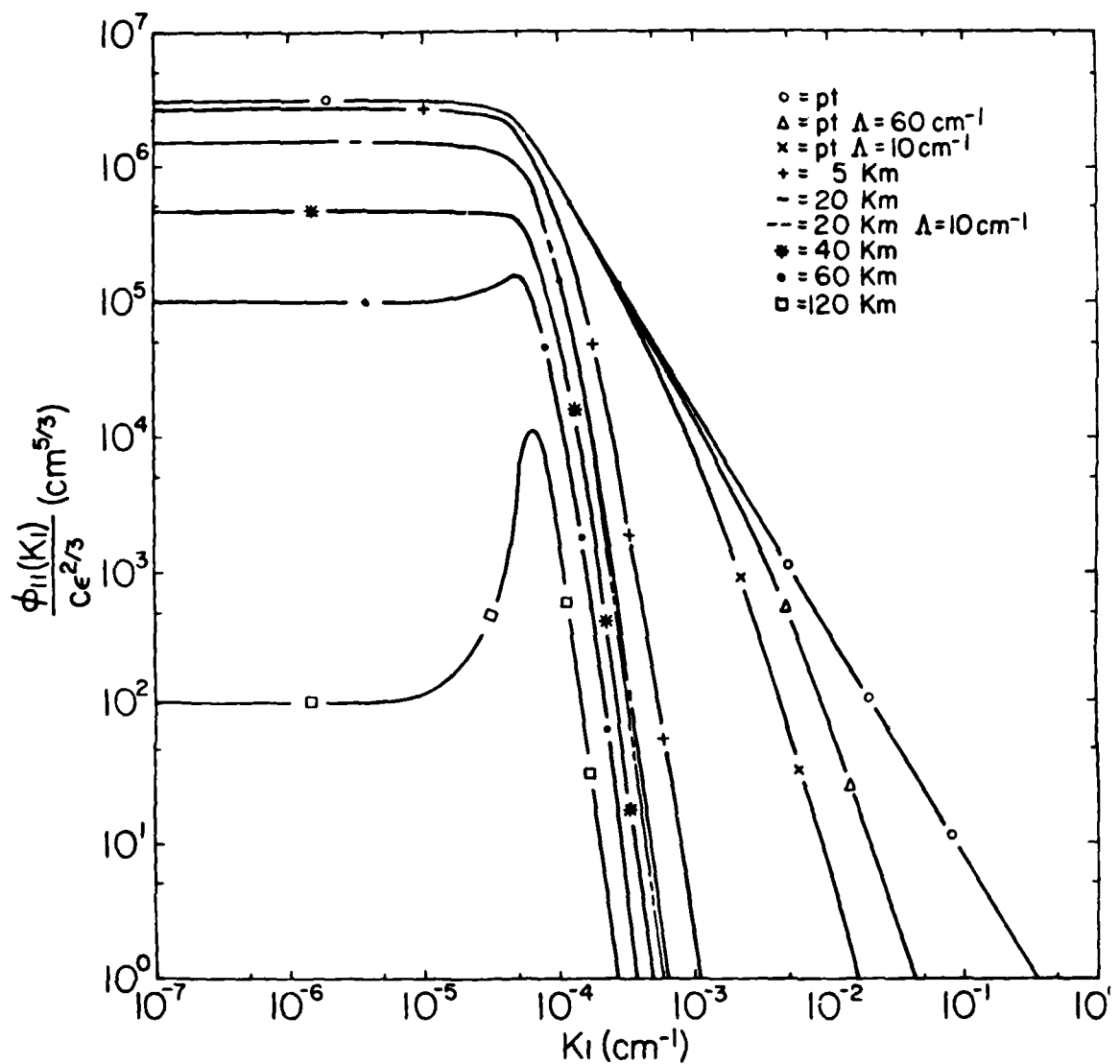


Figure E-4b. Turbulent power spectrum components of radar Doppler spectrum variance. Curves labeled pt. represent perfect tracers (pt.) and imperfect tracer ( $\Lambda = 10 - 60 \text{ cm}^{-1}$ ) precipitation environments. Curves labeled 5,20,40,60,120 km are radar beam filtered spectra for perfect tracers for ranges indicated. Full half-power beamwidth is 1 degree and pulse volume depth is 200 m. Outer scale  $\lambda_o = 1 \text{ km}$ .

ably retain equality among the three component variances to shorter scale values.

The above results show that solution of Equation 25 yields the Doppler spectrum variance that would be measured along any viewing direction in any precipitation environment and exhibiting turbulent outer scale values of .5 km or greater.

Figures E-5a, b show the variance (normalized to  $C\epsilon^{2/3}$ ) versus the range, and the ratio of pulse volume width/depth. The solid, long dash, and short dash curves represent the air (perfect tracer) and imperfect tracer ( $\Lambda = 60, 10 \text{ cm}^{-1}$ ) environments respectively. The curve marked  $\lambda_o = \infty$  is essentially Figure E-4a and is well represented by the analytical approximation of Frisch and Clifford (1974).<sup>9</sup> It is noted that the spectrum variance is essentially independent of outer scale length for ranges less than about 20 km. This simply reflects that at short ranges the various turbulent fields are nearly indistinguishable to the relatively small (compared to outer scale size) pulse volume and the variance contribution can be reasonably estimated from the approximation of Frisch and Clifford (1974). Significant deviation from this relation occurs when the maximum pulse volume dimension approaches the outer scale value.

The variation due to precipitation environment is significantly smaller, with increasing dependence on rain environment occurring with decreasing outer scale size and decreasing range. These features can more easily be seen by inverting the figure to form the estimate for eddy dissipation rate, the fundamental turbulent parameter.

Figures E-6a, b show  $\epsilon$  normalized to  $(\frac{\text{VAR}}{C})^{3/2}$  as a function of range, pulse volume width/depth ratio, outer scale  $\lambda_o$ , and particle distribution  $\Lambda$ . Observe that the precipitation effects become less important as the outer scale length increases. This reflects the more favorable response of the particles to increasing turbulent scale lengths, which also contain increasingly greater portions of the total air turbulent energy. Additionally, precipitation effects become significant at short ranges. For example, at a range of 10 km, the assumption of perfect tracers can lead to a 32 percent underestimate of  $\epsilon$  in heavy rain environments. This effect

<sup>9</sup> Frisch, A.S., and S.F. Clifford, 1974: A study of convection capped by a stable layer using Doppler radar and acoustic echo sounders, *J. Atmos. Sci.*, 31, 1622-1628.

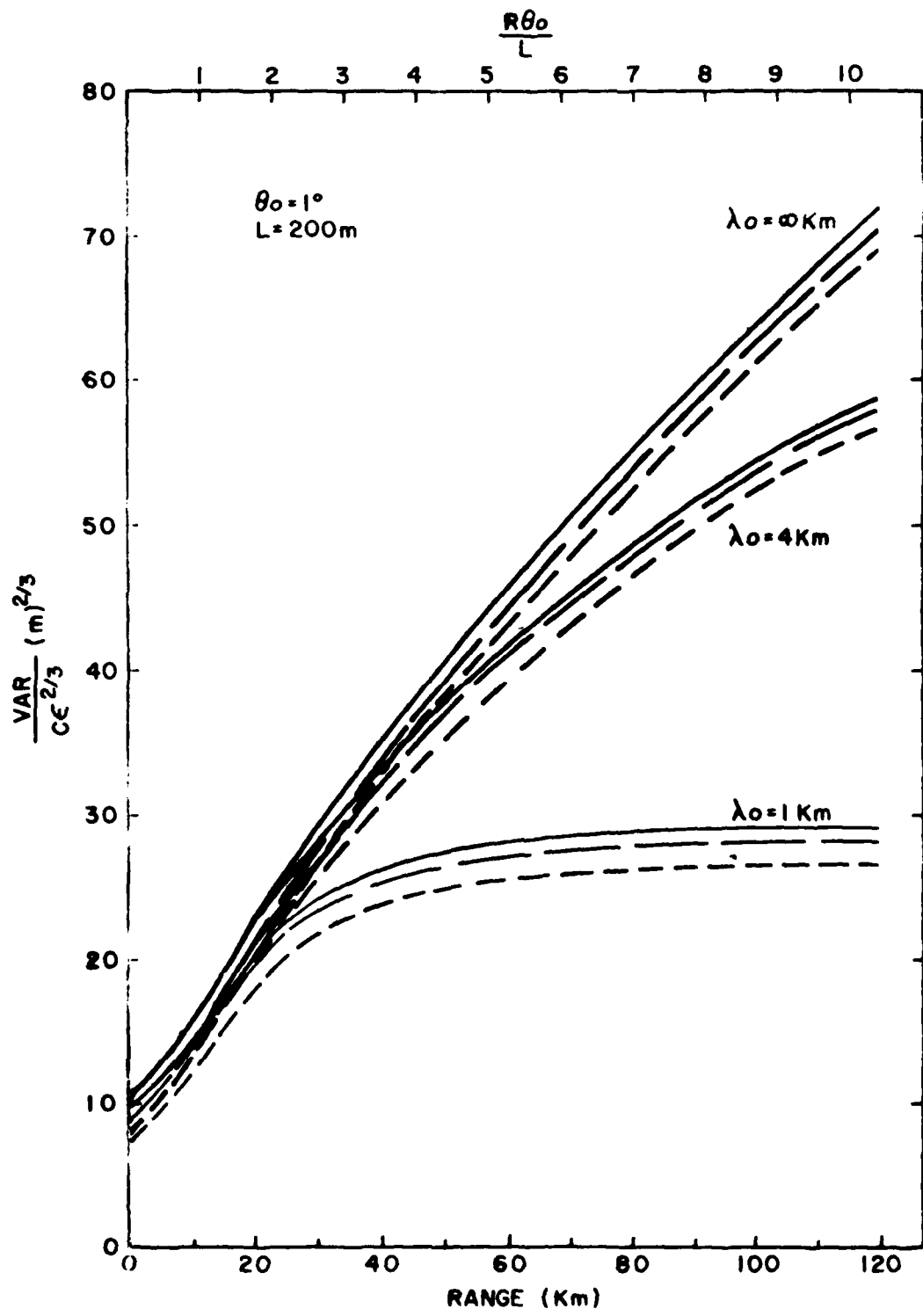


Figure 1-5a. Doppler spectrum variance (VAR) normalized to eddy dissipation rate ( $\epsilon$ ) and Kolmogorov constant ( $C$ ) versus radar range. Radar full half-power beamwidth is 1 degree and pulse volume depth is 200 m. Pulse volume width/length ratio at top. Outer scale  $\lambda_0 = 1, 4, \infty \text{ km}$ .

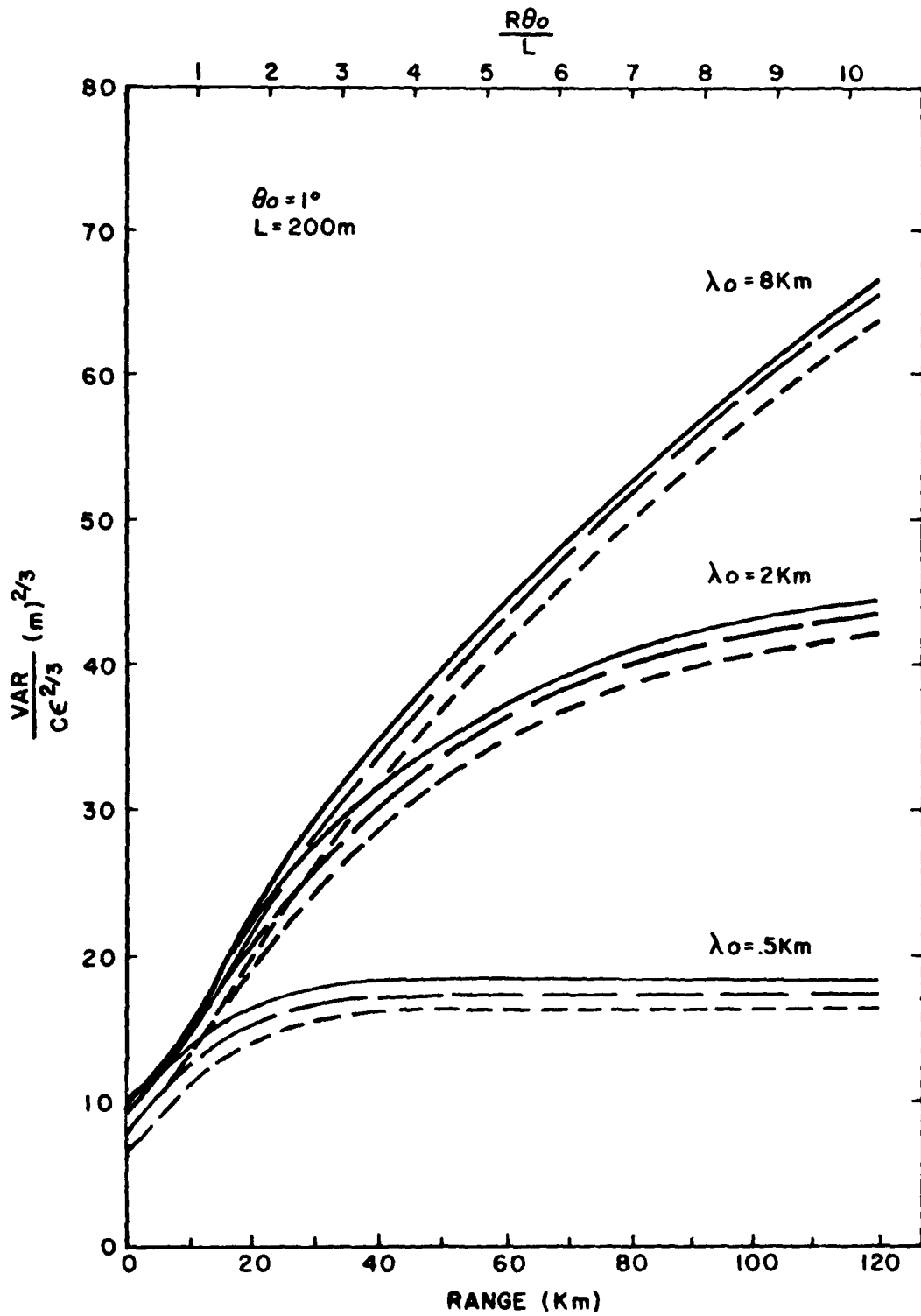


Figure E-5b. Doppler spectrum variance (VAR) normalized to eddy dissipation rate ( $\epsilon$ ) and Kolmogorov constant ( $C$ ) versus radar range. Radar full half-power beamwidth is 1 degree and pulse volume depth is 200 m. Pulse volume width/length ratio at top. Outer scale  $\lambda_o = .5, 2, 8\text{ km}$ .

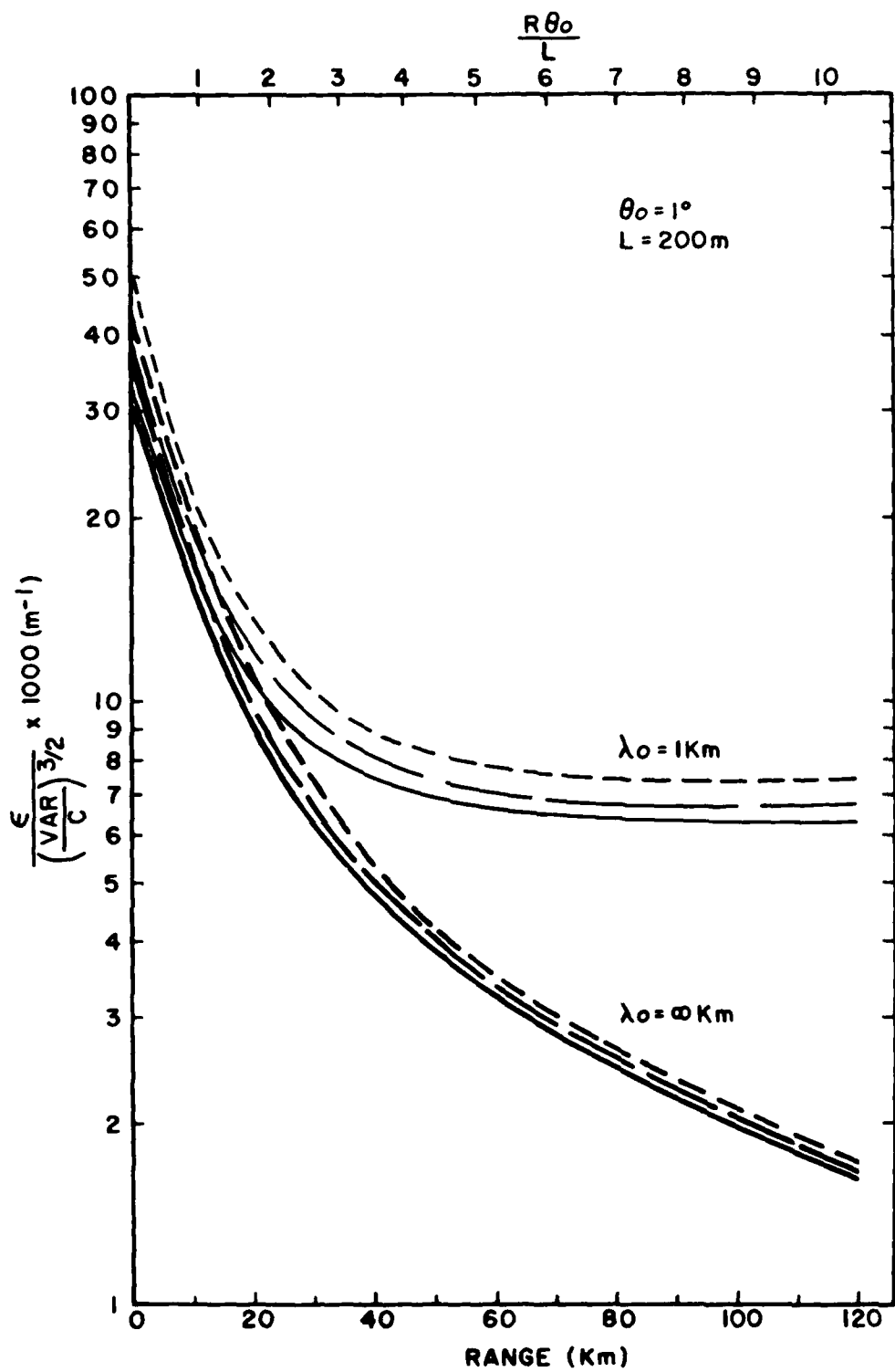


Figure E-6a. Eddy dissipation rate ( $\epsilon$ ) normalized to Doppler spectrum variance (VAR) and Kolmogorov constant (C) versus radar range. Radar beamwidth is 1 degree and pulse volume depth is 200 m. Ratio of pulse volume width/length at top. Outer scale  $\lambda_0 = 1, \infty \text{ km}$ .

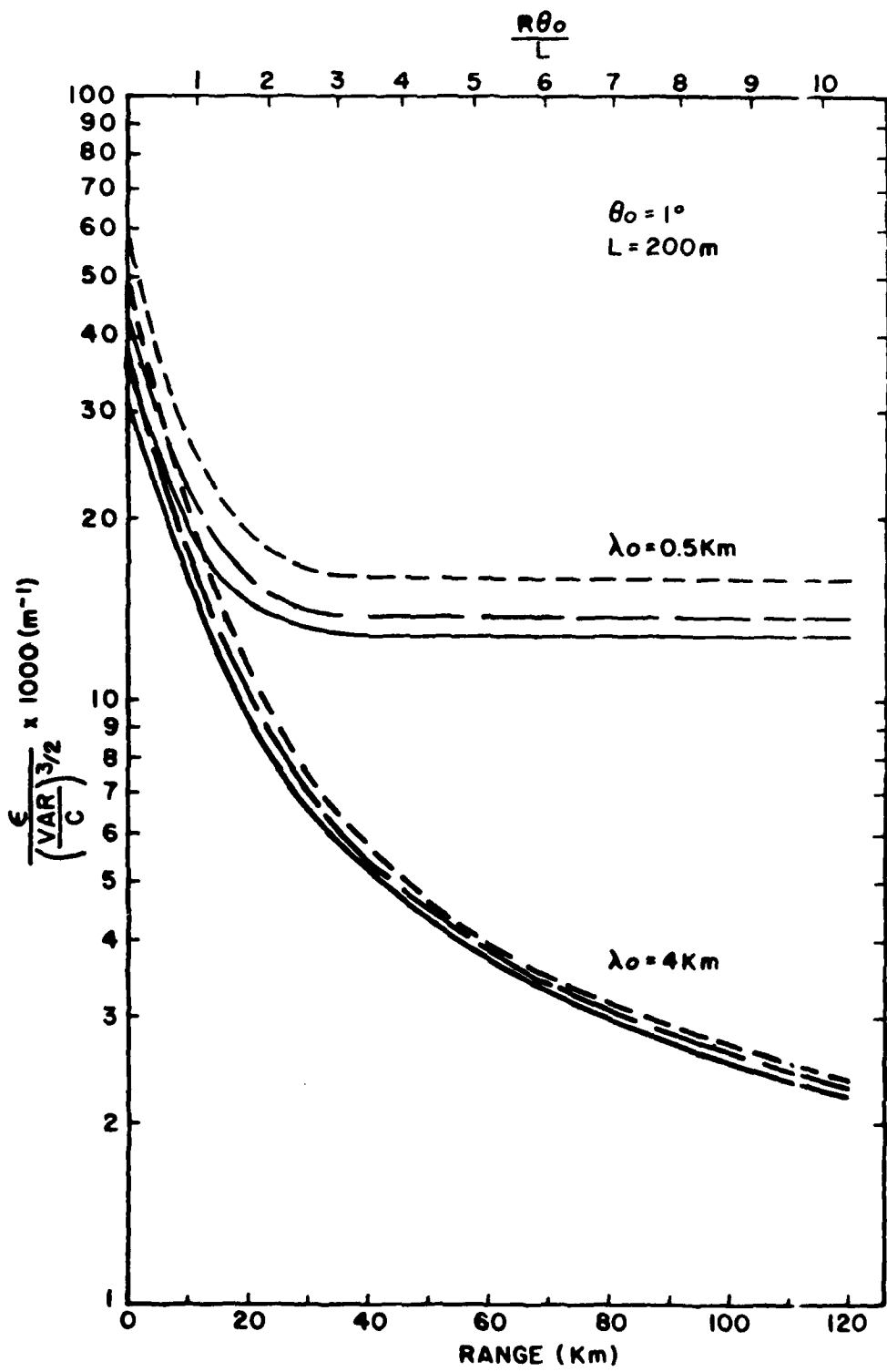


Figure E-6b. Eddy dissipation rate ( $\epsilon$ ) normalized to Doppler spectrum variance (VAR) and Kolmogorov constant (C) versus radar range. Radar beamwidth is 1 degree and pulse volume depth is 200 m. Ratio of pulse volume width/length at top. Outer scale  $\lambda_0 = .5, 4$  km.

results from the small size pulse volume being sensitive to only small turbulent scales to which precipitation responds poorly. Thus, in situations where the energy source for turbulence is obtained from small-scale structures (e.g., breaking Kelvin-Helmholtz waves) for which the outer scale may be small, or at ranges less than about 20 km, it is imperative that the precipitation environment be taken into account.

Of prime importance, however, is the thunderstorm environment. Aircraft observations have generally found turbulence to be patchy. This is to be expected since within storms there exist local regions of high shear which can provide the energy for turbulence production. There is yet no way of measuring by incoherent radar a turbulent outer scale value for these regions. The usefulness of estimating it from power spectrum analysis of Doppler radial velocity values is also questionable. Doviak et al (1978)<sup>10</sup> indicate that the variance of the Doppler spectrum does not increase dramatically with range for storm ranges of 50 to 120 km. This suggests, after comparison with Figures E-5a, b, that turbulence may frequently be the major contribution to Doppler spectrum variance and that, on the average, the turbulent outer scale may be 1 to 3 km. This result would be in agreement with general aircraft observations.

In this range the variability of  $\epsilon$  with both  $\lambda_o$  and precipitation environment is not too great. It may be possible to form a solution representing an average  $\lambda_o$  (or simple set of solutions dependent on various estimated  $\lambda_o$ ) with some simple correction determined from reflectivity factor to account for precipitation response, which may be representative of thunderstorm environments. Such a relation would always be superior to the commonly used relation of Frisch and Clifford, which as observed in Figure E-6, will always underestimate the eddy dissipation rate.

The material presented so far deals with the contribution to Doppler spectrum variance from precipitation in a given turbulent environment. This variance has been shown to be directly dependent upon the two basic turbulent parameters. The eddy dissipation rate is the quantity of interest since it describes the turbulent energy available per unit wavevector interval. However, Figures E-5 and E-6 demonstrate that some knowledge of the turbulent outer scale is required before we can successfully estimate this quantity. It was stated that turbulence in thunderstorms may be

<sup>10</sup> Doviak, R.J., D. Sirmans, D. Zrnic, and C.R. Walker, 1978: Considerations for Pulse Doppler radar observations of severe thunderstorms, J. Appl. Meteor., 17, 189-205.

localized, that there are a few patches wherein the turbulence is roughly homogeneous. The following material shows results of first analyses of aircraft thunderstorm gust velocity data which appear to support this concept and yield estimates of both  $\epsilon$  and  $\lambda_o$ .

The following data were acquired on May 26, 1976 by an Air Force F-4 instrumented aircraft. Two penetrations, separated by approximately 30 minutes, were made at a height of about 16 kft through a portion of a storm complex located 40 km south of Norman, Oklahoma. Aircraft measurements were taken every .1 second. The first run (Run 1) was from 210°. The second run (Run 2) passed through roughly the same storm region, but from 80° and 30 minutes later. Aircraft speed was at 198 m/sec during both runs. The discussion will center around the analysis of the vertical gust velocity data.

Figures E-7a - e and E-8a - e are plots of the vertical gust velocity, derived gust velocity, environmental temperature, aircraft normal acceleration, and barometric altitude during the two runs. The prominent feature in Run 1 is the apparent strong upward-moving current between 52510 and 52540. It is about 6 km wide and is characterized by a warmer temperature than the environment during entry and increased normal acceleration of the aircraft. Also note the large spikes in the vertical gust velocity of a somewhat periodic nature, suggesting the possible presence of waves. Similarly, Run 2 exhibits two apparent upward-moving air currents centered at 53775 and 53930 sec respectively. The period 53555 - 53645 exhibits strong periodic fluctuations. Increased aircraft normal acceleration and spikes in vertical gust velocity are also noticed here.

Casual observation of these two plots suggests that each gust velocity time sequence may be segmented into a number of discrete local turbulence zones. In Run 1, we focus on three zones labeled 3, 5, and 7 in Figure E-7a corresponding to the visually estimated turbulence classes moderate, heavy within updraft region, and moderate, respectively. Similarly, in Run 2, the time series is segmented into zones 1, 5, 6, 9, 7, 8, respectively.

Each gust velocity time series was subjected to power spectral analysis. The analyses were conducted on segments of the original data sets. Each segment consisted of one or more of the individual zones and is labeled 1 - 7 (Run 1) and 1 - 9 (Run 2) respectively. Each segment was linearly detrended before being subjected to spectrum analysis. Although

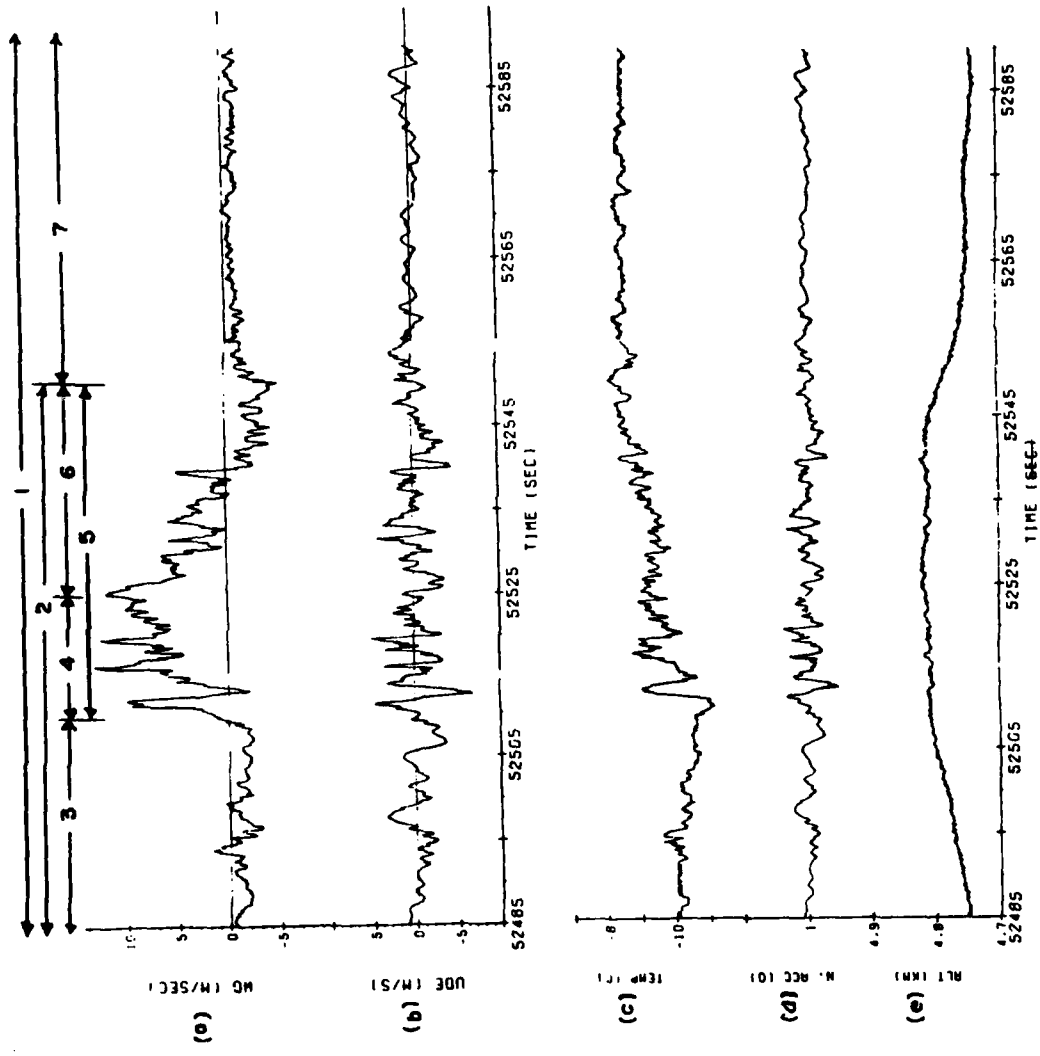


Figure E-7. Aircraft time series data for Run 1: a) vertical gust velocity, b) derived gust velocity, c) environmental temperature, d) normal acceleration, and e) barometric altitude. Analyzed segments are labeled 1 - 7.

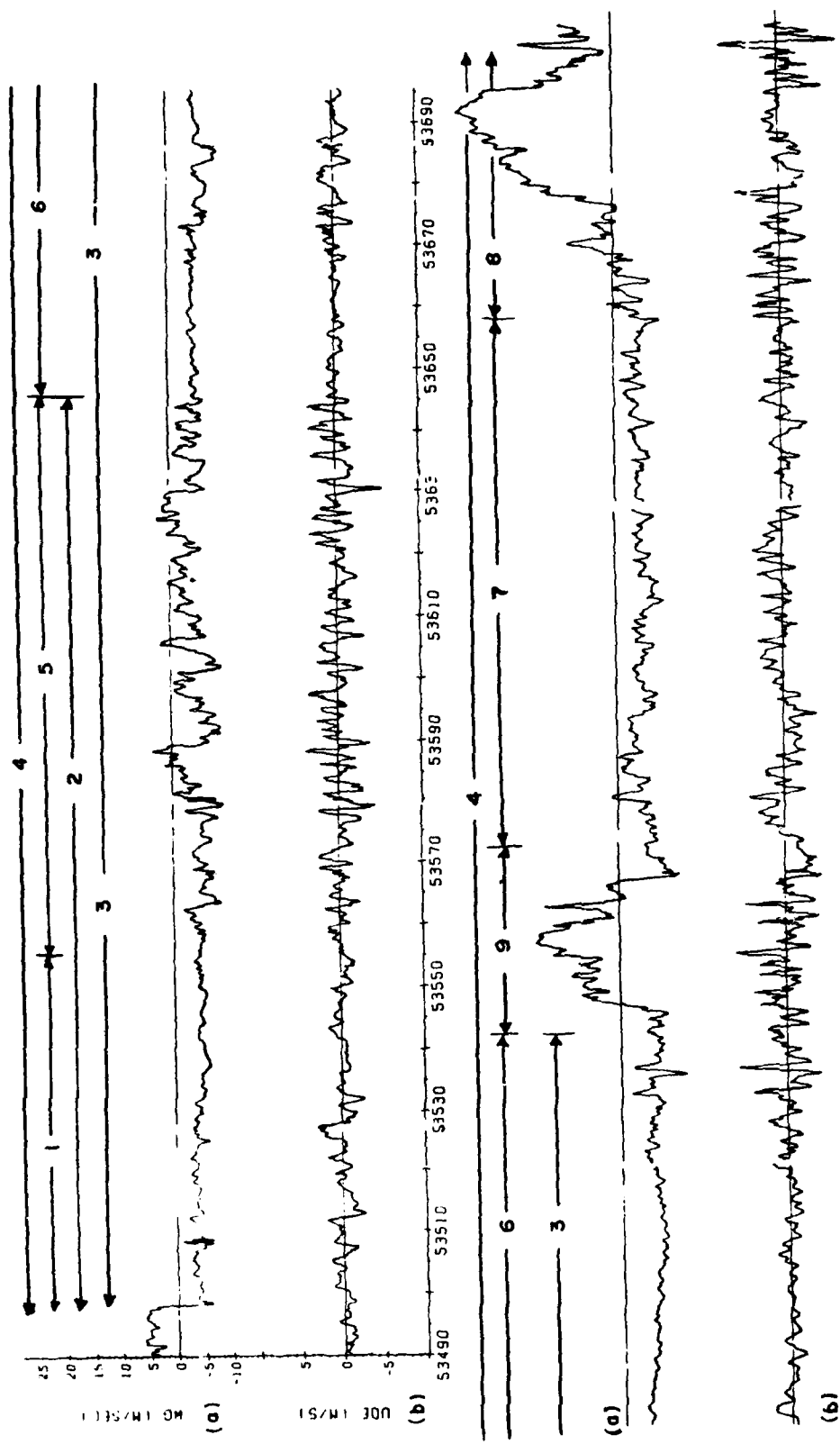


Figure E-8. Aircraft time series data for Run 2: a) vertical gust velocity, b) derived gust velocity. Analyzed segments are labeled 1 - 9.

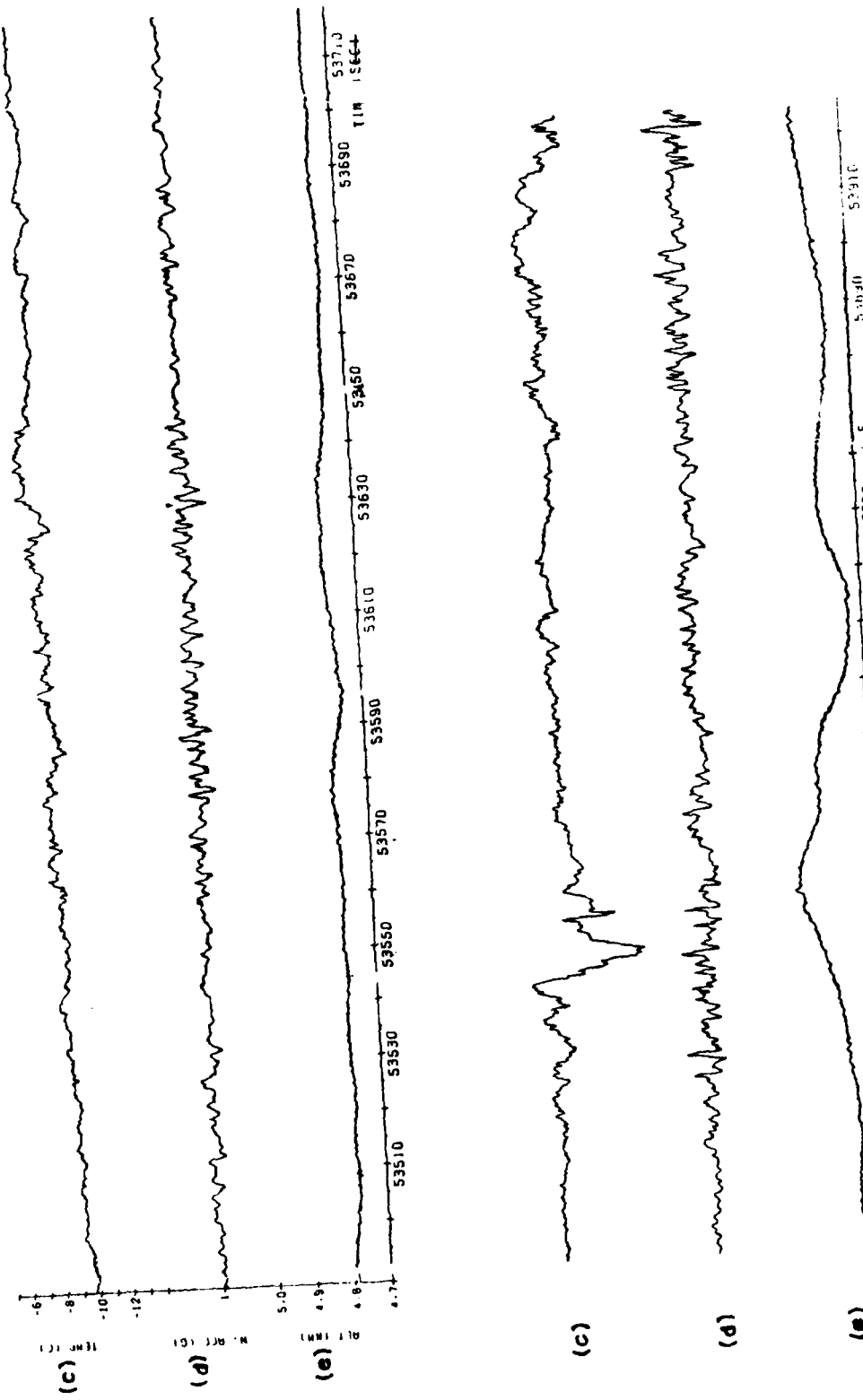


Figure E-8c, d, e. Aircraft time series data for Run 2: c) environmental temperature, d) normal acceleration, and e) barometric altitude.

detrending forces the power spectral density to go to zero at zero frequency, the spectral outer scales are generally well beyond the influence of this scale removal action, and should represent a true change of spectral slope. Figures E-9a - g and E-10a - h show the power spectral density (PSD) plotted as a function of radian frequency. An approximate space scale is also included. Observations from Run 1 will be presented first.

It is observed that the spectra may be classified according to where the sharp changes in slope (knee) of the curves occur. Spectra 3, 4, and 6 exhibit apparent slope changes at scales less than 1 km, whereas spectra 1, 2, 5, and 7 appear to have the knee located at scales greater than 2 km. It is believed that segment 7 (spectrum 7) would also have shown a small outer scale length if the time record 52550 - 52555 had not been included. Reference to Figure E-7a shows that spectra 1, 2, and 5 are strongly biased by inclusion of the upcurrent region as a turbulent fluctuation rather than as a true feature of the larger storm wind structure. The updraft region thus acts as a large, very energetic eddy which strongly biases the strength ( $V^2$ ) of the turbulent field and introduces extra energy into the long wavelength region of the PSA curves. In the sense that the upcurrent does not qualify as a truly turbulent feature, it is inappropriate to include it blithely in PSA. Spectra 4 and 6 show the power spectra derived from the fluctuations imbedded in the positive and negative slope portions of this upcurrent region. It is seen that these spectra are similar to spectrum 3. Referring back to Figure E-4b, it is observed that the knee of the spectral curve well represented the turbulent outer scale length under the ideal conditions of homogeneous isotropic turbulence. It is felt that here the knee may be a reasonable measure of this parameter.

Now consider Run 2. These spectra are not as easily categorized. It is clear that spectrum 4, which includes all data as turbulence, exhibits the largest apparent outer scale value and generates large spectral densities at long wavelengths. Again, this results from inclusion of the updraft features as turbulent gusts. The lower power but prominent peak near 80 km in spectrum 1 results from a .5 sec ripple riding on the gust velocity trace. These fluctuations are too fine to be seen in these highly reduced traces. In spectrum 6 a long (about 40 sec) modulation is likely the cause of the spectral peak near 4.6 km. It is instructive to compare spectra 1,

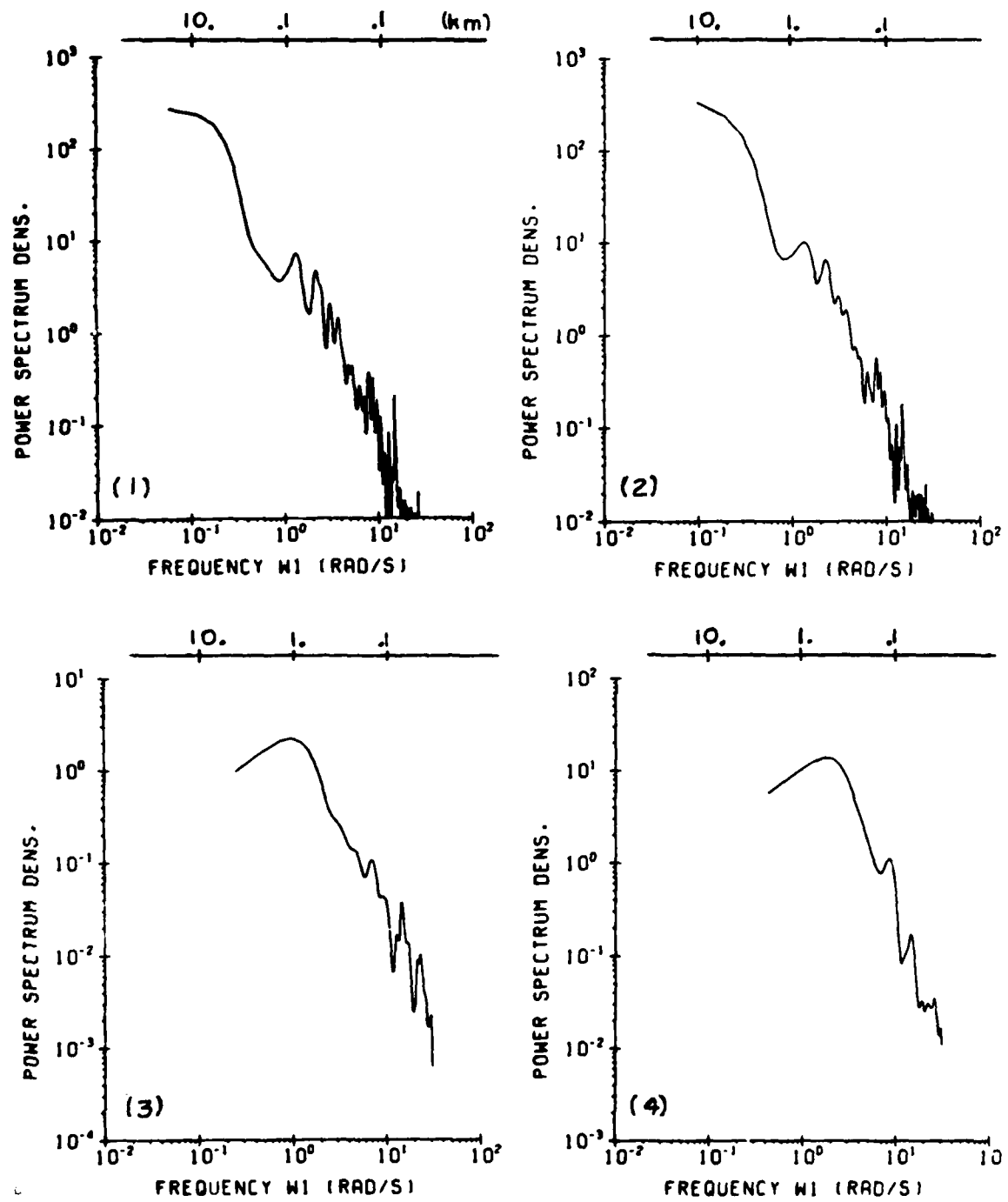


Figure E-9a-d. Turbulent power density ( $\text{m}^2/\text{s}^3$ ) versus frequency (rad/sec). Equivalent space scale at top. Labels (1) - (4) indicate appropriate segment from Run 1.

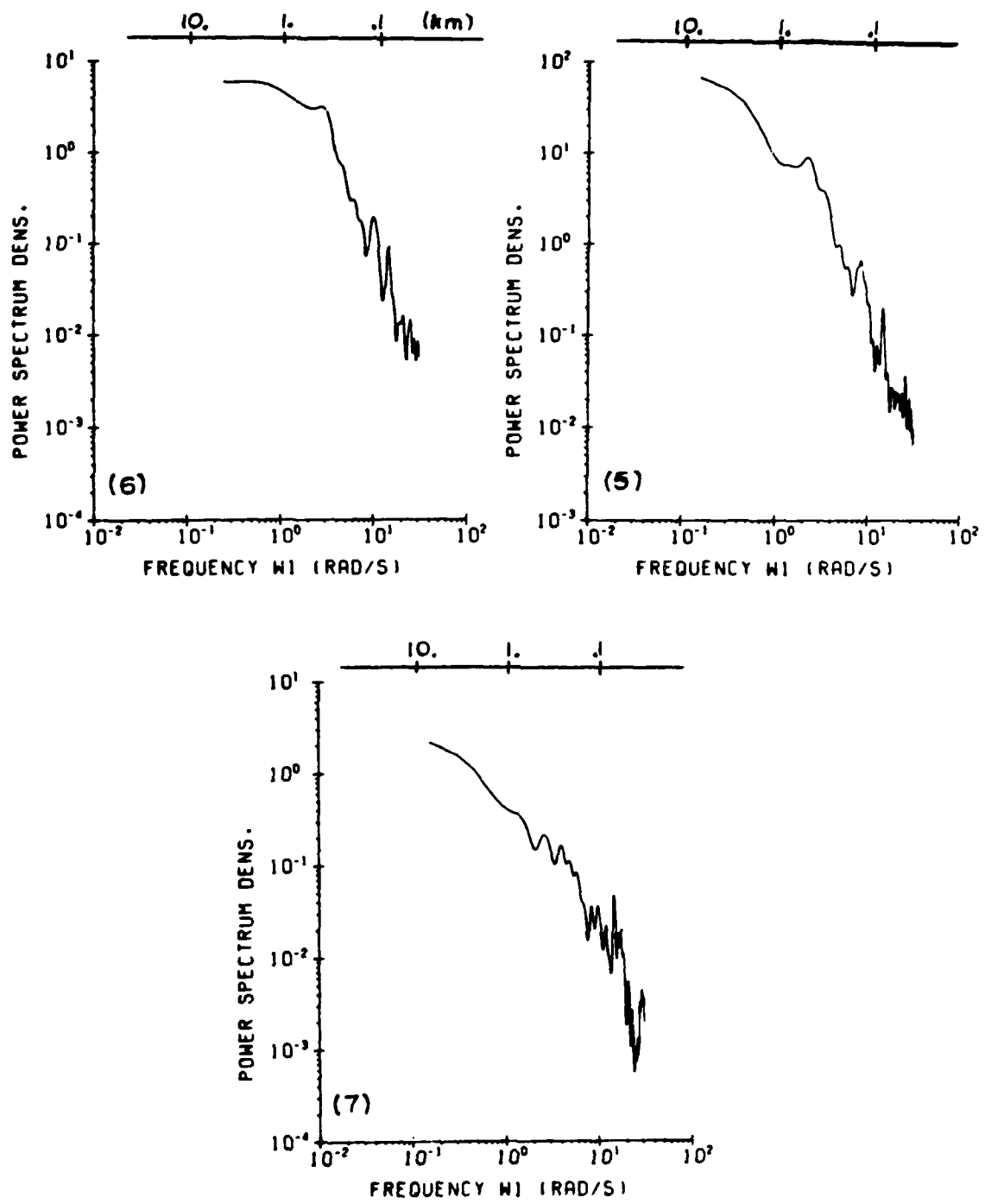


Figure E-9e-g. Turbulent power density ( $\text{m}^2/\text{s}^3$ ) versus frequency (rad/sec). Equivalent space scale at top. Labels (5) - (7) indicate appropriate segment from Run 1.

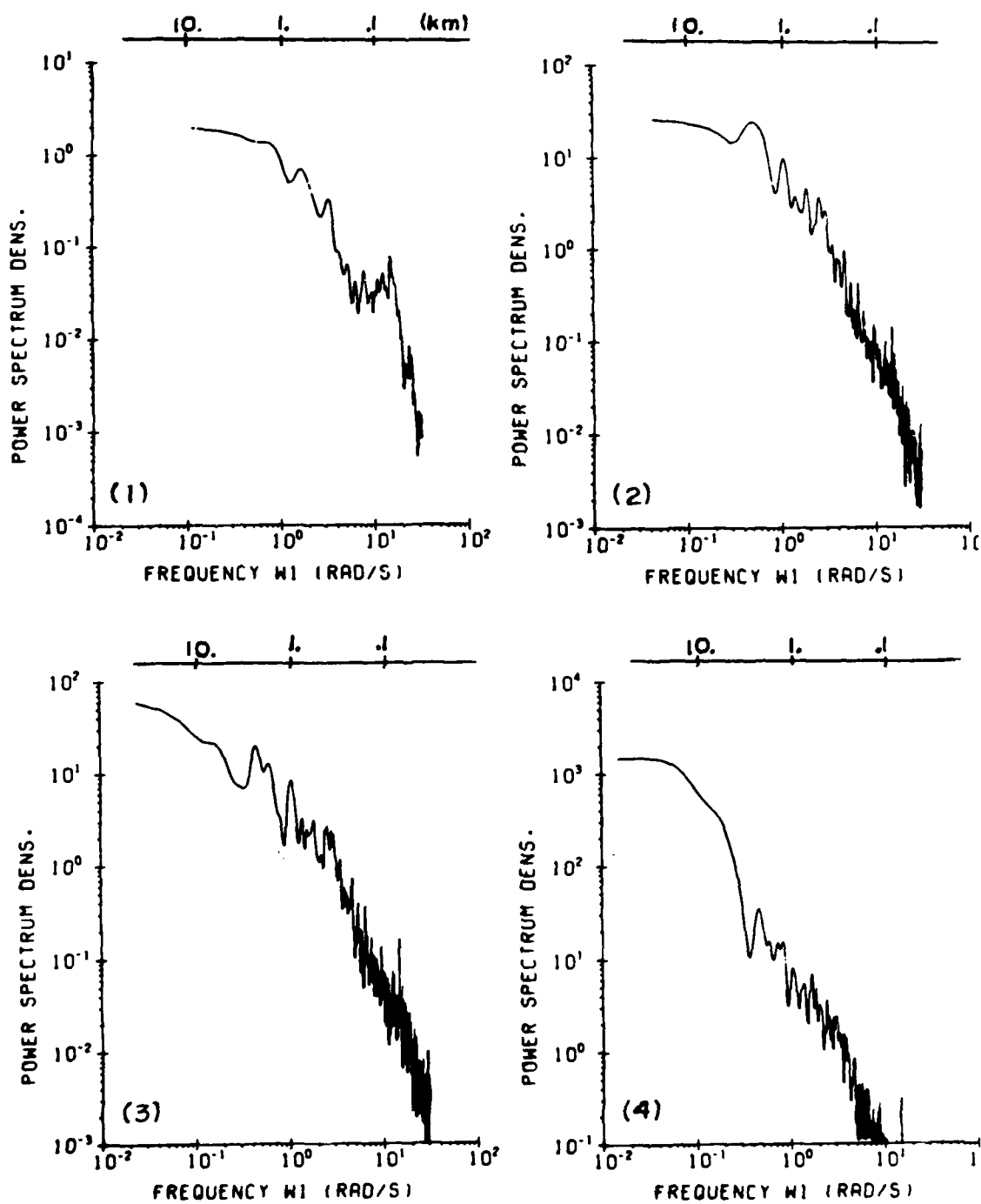


Figure E-10(a-d). Turbulent power density ( $\text{m}^2/\text{s}^3$ ) versus frequency (rad/sec). Equivalent space scale at top. Labels (1) ~ (4) indicate appropriate segments from Run 2.

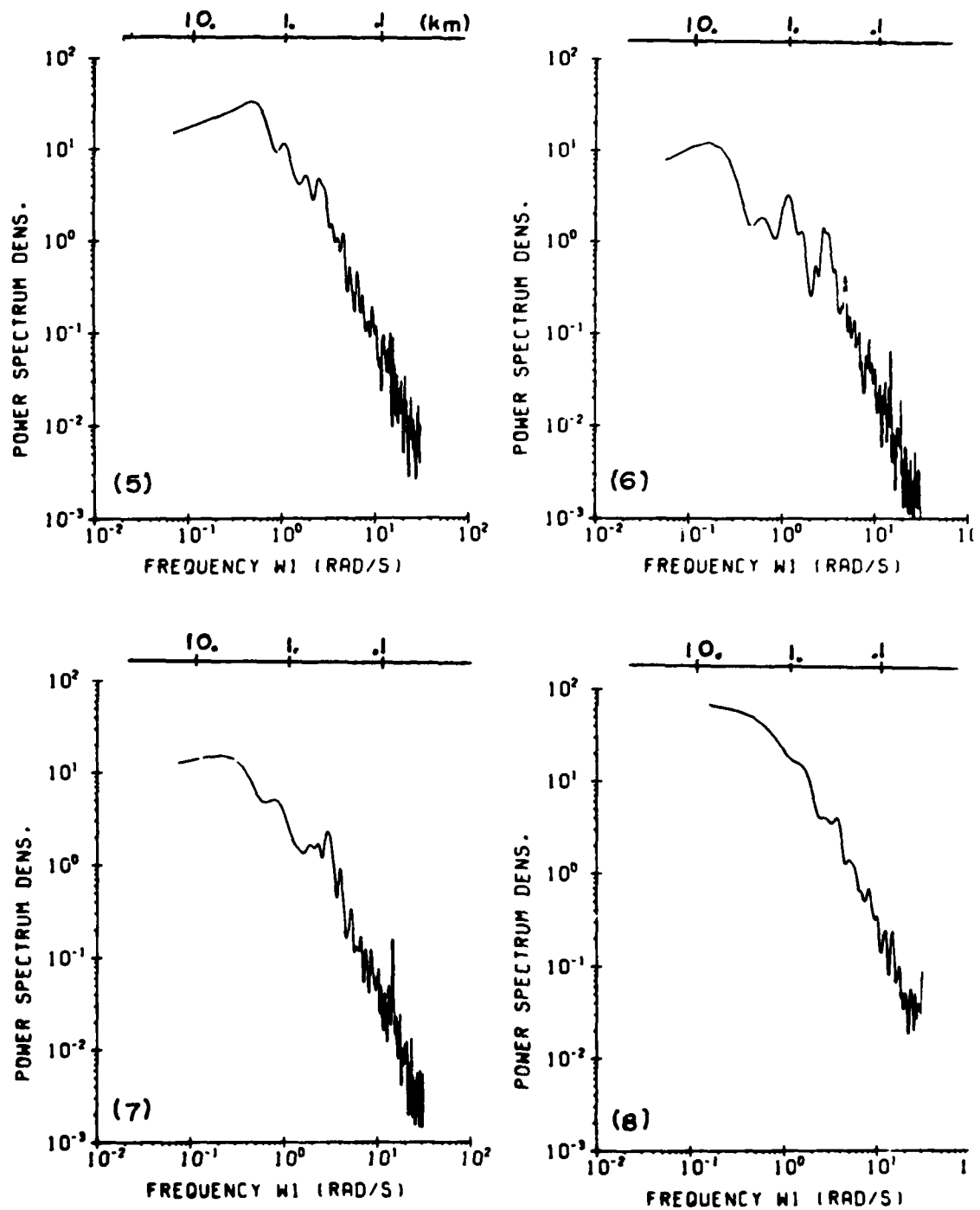


Figure E-10(e-h). Turbulent power density ( $\text{m}^2/\text{s}^3$ ) versus frequency (rad/sec). Equivalent space scale at top. Labels (5) - (8) indicate appropriate segments from Run 2.

3, 5, and 6. Note that spectra 1, 5, and 6 have a well-defined knee. However, when these three regions are combined into one (3), the resulting spectrum does not exhibit this clear slope change at short scales. In this instance, segment 5 appears to act similarly to an upcurrent region for the composite segment. The apparent turbulent outer scales for Run 2 for the individual segments are in the range 1 - 2.4 km. These data indicate that inclusion of storm structure, non-turbulent fluctuations, and composites of local turbulent patches can strongly influence the resulting apparent turbulent power spectra derived from the data.

Table E-1 provides the mean square velocity, estimated outer scale length, and estimated eddy dissipation rate for these various spectra. Note that the outer scale lengths are considerably larger for Run 2 than for Run 1. This difference is primarily a result of sampling non-identical storm regions, but may also indicate a temporal evolution. The almost synergistic effect of combining local turbulence zones into single larger units is dramatically demonstrated by the air motion variance  $V^2$ . Surprisingly, the eddy dissipation rates for the two spectral sets are very similar. Within non-updraft regions, both runs show  $\epsilon$  in the range 20 - 50  $\text{cm}^2/\text{sec}^3$ . The largest  $\epsilon$  are found within the updraft regions and range from 417 - 1680  $\text{cm}^2/\text{sec}^3$ . These values indicate that non-updraft regions would be characterized as moderate in strength, while the updraft regions are heavy to extreme (MacCready, 1964).<sup>11</sup>

Finally, it is instructive to consider the turbulent velocity and Doppler spectrum variance estimates which would have been made by a Doppler radar scanning these same regions. One method of estimating this is to apply to the data a filter which represents the equivalent 2-way beam filter function of the radar. Figures E-11 and E-12 show the equivalent radar mean turbulent velocity and spectrum variance that would have resulted in a uniform reflectivity field. Each gust velocity segment was detrended before application of the filter and the radar pulse volume was assumed to have a one degree beam width and 200 m depth.

Generally, the derived spectrum variances are quite small. Run 1 shows they are of the order of  $.05 - 1 \text{ m}^2/\text{sec}^2$  with a mean of roughly  $.1 \text{ m}^2/\text{sec}^2$  in regions 3 and 7, while in the updraft region, the range is

<sup>11</sup> MacCready, P., 1964: Standardization of gustiness values from aircraft, J. Appl. Meteor., 3, 439-449.

TABLE E-1. ESTIMATED TURBULENT PARAMETERS

| Spectrum Segment No.                         | 1     | 2     | 3    | 4     | 5    | 6    | 7    | 8                   |
|--|-------|-------|------|-------|------|------|------|---------------------|
| $v^2$ ( $\text{m}^2/\text{sec}^2$ )          | 12.19 | 17.73 | .77  | 7.56  | 9.25 | 2.81 | 3.68 | (Early Period)      |
| $\lambda_o$ (km)                             | .62   | .62   | .95  | .5    | 4    | .38  |      |                     |
| $\varepsilon$ ( $\text{cm}^2/\text{sec}^3$ ) |       |       | 30   | 1680  |      | 417  | 26.2 |                     |
| $v^2$ ( $\text{m}^2/\text{sec}^2$ )          | .534  | 4.15  | 3.34 | 32.36 | 5.84 | 1.33 | 2.39 | 12.38 (Late Period) |
| $\lambda_o$ (km)                             | 1.18  | 1.8   | 2.48 |       | 2    | 1.13 | .41  | 2.06                |
| $\varepsilon$ ( $\text{cm}^2/\text{sec}^3$ ) | 17.6  |       |      |       | 318  | 52.4 | 49   | 875                 |

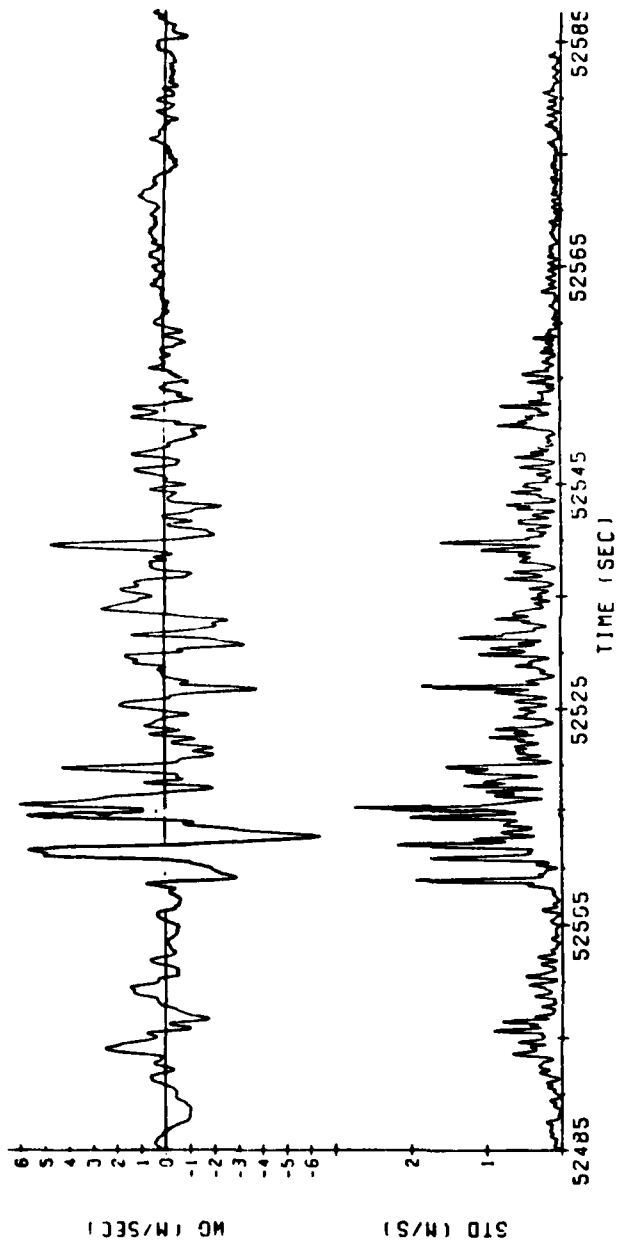


Figure E-11. Equivalent radar Doppler spectrum mean and standard deviation derived from aircraft gust velocity data. Radar beam filter has a 1 degree full half-power beamwidth and 200 m pulse volume length. Data for Run 1.

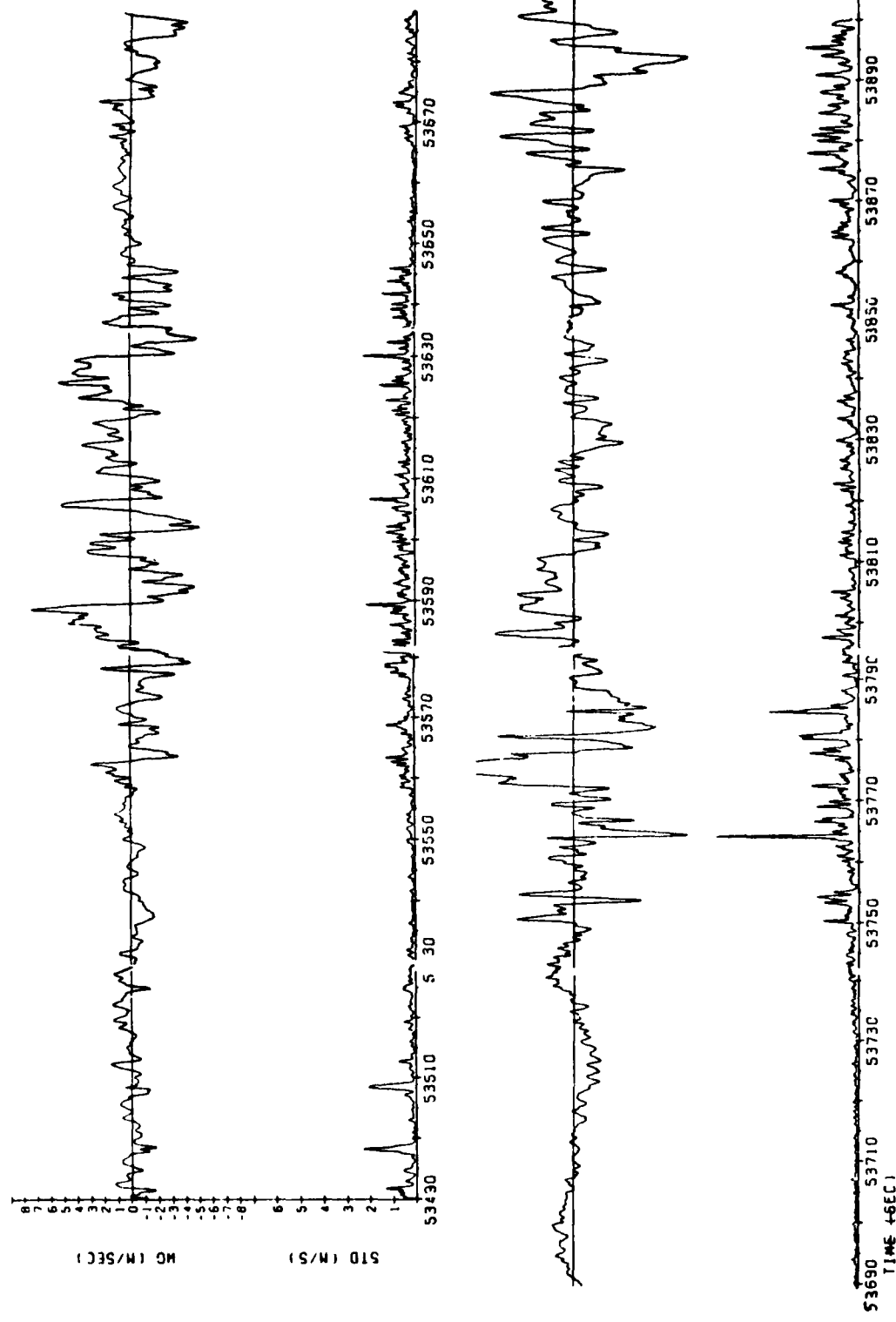


Figure E-12. Equivalent radar Doppler spectrum mean and standard deviation derived from aircraft gust velocity data. Radar beam filter has a 1 degree full half-power beam-width and 200 m pulse volume depth. Data for Run 2.

significantly larger at  $.1 - 8 \text{ m}^2/\text{sec}^2$  and has a mean value of  $.25 \text{ m}^2/\text{sec}^2$ . Again, the spikes are a result of the periodic fluctuation in the original data and may not really be representative of turbulent contribution.

The results for the late period are similar. Zones 1 and 6 have variances of the order  $.01 \text{ m}^2/\text{sec}^2$  with the updraft regions exhibiting  $.25 - 8 \text{ m}^2/\text{sec}^2$ .

These equivalent radar variance values are generally smaller than those typically observed by radar, which are generally  $1 - 36 \text{ m}^2/\text{sec}^2$  with a mean value range of  $4 - 16 \text{ m}^2/\text{sec}^2$ . The discrepancy here may result from the vertical gust velocity not being representative of the horizontal turbulent components, and exclusion of normal radar spectrum broadening agents such as system noise and wind shear. The preliminary analysis indicates that it is really necessary to compare coordinated aircraft and radar data to determine whether equivalent radar estimates can be reliably obtained in this manner.

The results discussed here will allow for increased accuracy in Doppler radar estimation of turbulence intensity, and will have practical application. As earlier stated, the two main contributions to Doppler spectrum variance are the transverse shear of the radial wind and turbulence. The Doppler radar can estimate the shear component by observing the variation in azimuth and elevation of the mean Doppler velocity between successive radials. Thus, the turbulent contribution can be estimated. With some knowledge of the turbulent outer scale, and storm reflectivity factor, a reasonable estimate of the eddy dissipation rate may be obtained. This information can then be combined with the known response characteristics of aircraft for identification of regions of hazard to aircraft. Use of these results with incoherent radar is significantly more difficult, however. The incoherent radar can not estimate the Doppler mean velocity, and therefore will not allow for the determination of the transverse shear. Thus, the turbulent variance contribution may not be well known.

Atlas and Srivastava (1971)<sup>12</sup> proposed a method for estimating an atmospheric structure function with incoherent radar by forming combinations of signal returns from successive pulse volumes along a given radial. They showed that the mean squared difference of Doppler velocity between the

<sup>12</sup>Atlas, D., and R.C. Srivastava, 1971: A method for radar turbulence detection, IEEE Trans. on Aerospace and Electronics, AES-7, No. 1, 179-187.

adjacent pulse volumes can be related to the Doppler spectral variances by

$$(V_2 - V_1)^2 = \frac{\lambda^2}{4} \frac{(P_1 + P_2)}{P_1 P_2} (\text{VAR}_{12} (P_1 + P_2) - \text{VAR}_1 P_1 - \text{VAR}_2 P_2) \quad (33)$$

where  $\lambda$  is the radar wavelength,  $\text{VAR}_1$  and  $\text{VAR}_2$  are the Doppler spectral variances ( $\text{sec}^{-2}$ ) from pulse volume numbers 1 and 2 having total spectrum powers  $P_1$  and  $P_2$ , and  $\text{VAR}_{12}$  is the variance of a composite Doppler spectrum obtained from adding the signals from the individual pulse volumes. Unfortunately, this relation is a highly smoothed estimate of the true atmospheric structure function (Sychra, 1974)<sup>13</sup> requiring very careful interpretation; it is also related to the environmental wind shear.

A measured Doppler radial estimate may be considered as a sum of a large-scale background wind ( $V_w$ ), turbulent component ( $V_t$ ), and an additional random error and noise bias ( $e$ ), as

$$V = V_w + V_t + e. \quad (34)$$

With this convention the left-hand side of Equation 33 becomes

$$(V_2 - V_1)^2 = (V_{2w} - V_{1w})^2 + (V_{2t} - V_{1t})^2 + (e_2 - e_1)^2 \quad (35)$$

where the second term is actually the true Doppler estimate of the pulse volume filtered turbulent structure function. If two azimuthal pairs of pulse volumes (( $V_2, V_1$ ) and ( $V_3, V_2$ )) are combined in this manner, then in a region where the mean turbulent air velocity over the region occupied by the pulse volumes varies little,

$$(V_3 - V_1)^2 - (V_2 - V_1)^2 \approx (V_{3w} - V_{1w})^2 - (V_{2w} - V_{1w})^2. \quad (36)$$

Using Equation 36, a linear variation in large-scale wind can be fitted to the data, thereby providing an estimate of the large-scale shear. If a quadratic variation in the wind field is desired, two such sets of Equation 36 may be used.

Obviously this technique is prone to error where the gradient of

<sup>13</sup>Sychra, J., 1974: Fluctuation spectra and velocity structure function, Tech. Rpt. 33, Lab. for Atmos. Prob., U of Chicago.

mean turbulent velocity is large. However, at the ranges of interest, perhaps 60 - 200 km, most of the turbulent energy is mapped into the Doppler spectrum variance. For this case, the radar estimate of the turbulent structure function is small, and its variation is not significant, allowing Equation 36 to be useful. The validity of this relation is independent of the actual magnitude of the air turbulent intensity. Therefore, the above relations may be applicable within local patches of turbulence and may return reasonable estimates of transverse radial wind shear, thus permitting an estimate of eddy dissipation rate to be obtained. Usefulness of this technique can only be established after comparison of radial shear estimates from Doppler and incoherent techniques using real data.

#### (C). Conclusions

The results of theoretical investigation demonstrate that useful and understandable relationships exist between Doppler radar spectrum variance and turbulence. For ranges less than 20 km, Doppler radar spectrum variance is independent of turbulent outer scale and dependent upon eddy dissipation rate and range. At ranges greater than 20 km, Doppler spectrum variance is strongly dependent upon all three quantities. However, once the largest pulse volume dimension becomes comparable to the turbulent outer scale length, the spectrum variance becomes range independent. Imperfect particle response is found to reduce significantly the measurable turbulent strength for outer scale lengths less than about 500 m. At larger lengths, precipitation response has only a minor effect. It is suggested that order of magnitude estimates of turbulent eddy dissipation rate may be obtained by using a generic outer scale length of 2 km. Accurate estimation of turbulent strength, however, awaits some method of remotely estimating turbulent outer scale values for the local turbulent patches within thunderstorms.

END